The Nanostructure of High-performance Fibres

Pauw, Brian Richard

Publication date:
2010

Document Version
Publisher's PDF, also known as Version of record

The Nanostructure of High-performance Fibres

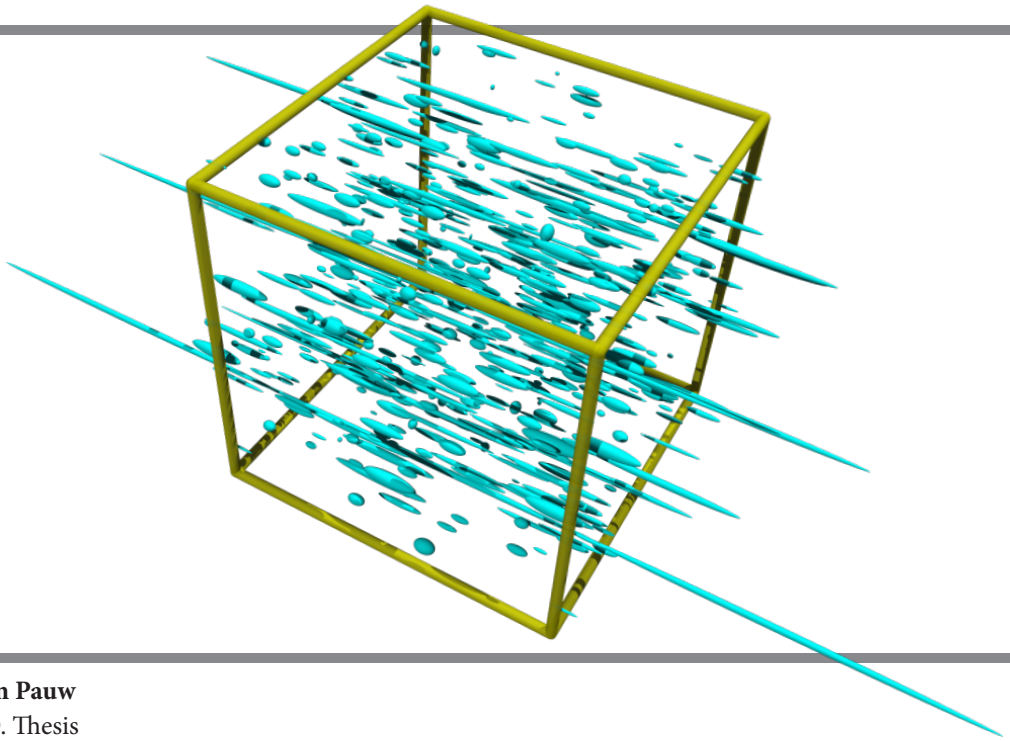

Brian Pauw
Ph.D. Thesis
2009

DTU Chemical Engineering
Department of Chemical and Biochemical Engineering

The nanostructure of high-performance fibres

Brian R. Pauw*

September 30, 2009

*Supervised by: M.E. Vigild, K. Mortensen, J. W. Andreasen, E. A. Klop

ISBN 978-87-92481-12-2

Printed in Denmark by
WWW.FRYDENBERG.DK
Baldersgade 12 - 16
DK-2200 Copenhagen N

Summary

High-performance fibres are produced by spinning a large number of polymer filaments into fibres (yarns)*. It is well known that during this process, nanostructures tend to form within the individual filaments. Investigations show a strong correlation between the properties of the nanostructure and the physical properties of the fibres. High-performance polymer fibres, such as poly-(*para*-phenylene terephtalamide) (aramid, PPTA) fibres, are examples of fibres exhibiting such a nanostructure. Investigation and quantification of the nanostructure of PPTA (and the porous structure in particular) is the main topic of this research.

Small-angle X-ray scattering (SAXS) has the power of characterising this structure without the need for destructive sample preparation. The challenging part of SAXS, however, is the analysis of the recorded scattering patterns. SAXS patterns obtained from PPTA fibres indicate the presence of an oriented nanostructure. Such a nanostructure is often characterized through analysis of sections of the SAXS patterns using methods derived from isotropic scattering, such as the Debye-Bueche method and the Porod method for determining size parameters. Other methods used are the Effler Invariant method and "Ruland Streak" method for determination of the degree of orientation of the scatterers. These methods are reviewed here and compared with measured and simulated data to provide insight into the applicability of the traditional methods.

An alternative analysis methodology is presented which fits the entire 2D scattering pattern to a model of perfectly aligned polydisperse ellipsoids, with the advantage that size distribution parameters are obtained. This analysis methodology is tested using the simulated data. Application of the methodology to the scattering patterns obtained from the PPTA fibres shows a reasonable fit. Improvements to the analysis methods are compared, consisting of the introduction of an orientation distribution to allow imperfect alignment of the scatterers, and the addition of large scatterers to take the effect of fibrillar scattering on the scat-

*For a graphical description of the terms "fibre", "filament" and "fibril", the reader is referred to Figure 1.4

tering pattern into account. The fit to the scattering pattern of as-spun aramid fibre is improved by the introduction of the large scatterers, while the fit to the scattering pattern obtained from the heat-treated fibre improves when imperfect alignment is taken into account. Due to the heat treatment, the average width and length of the scatterers increase.

The nanostructural behaviour of these polymer fibres under axially compressive and tensile strain has also been investigated. For this purpose, a single filament was put in a loop in order to effect regions of tensile and axially compressive strain (under elastic deformation) in parts of the filament. The top of the loop (where the radius of curvature is smallest, and thus the imposed strain the highest) was then probed using microbeam SAXS at the Swiss Light Source. SAXS data was extracted from the compressive as well as tensile region of the bent section, which shows oscillations in the highly anisotropic SAXS patterns, which indicates a regular internal structure likely originating from cracks or slip planes between packs of fibrils. The oscillations can be modelled as scattering from a packed array of the tape- or cylinder-shaped objects, the presence of which are supported by SEM images. In the inner side of the loop, where axially compressive strain is present, the fibril packs exhibit fibrillar separation upon decreasing the loop size, increasing the number of cracks between the scattering elements. With tensile strain the fibrils pack more tightly, resulting in the observation of packs of fibrils as one scattering element and an increase in repetition distance between slip planes.

Lastly, Initial results obtained from in-situ tensile and heating experiments show that the nanostructure is affected by high amounts of stress and moderate temperatures. The application of tensile strain shows the elongation of the void structure, and an increase in the degree of orientation. Heating affects (mostly) the length of the voids, which is reduced upon the application of heat. The results of combined heating and stretching experiments show a combination of these effects occurring.

Dansk resume

Højeffektive fibre produceres ved at spinde et stort antal polymerfilamenter (uld) til fibre (garn). Det er velkendt at der i løbet af denne process dannes nannostrukturer inde i de enkelte filamenter. Undersøgelser viser en høj grad af overensstemmelse mellem nanostrukturernes egenskaber og fibrenes fysiske egenskaber. Højeffektive polymerfibre, så som poly-(*para*-phenylene terephtalamide) (aramid, PPTA)fibre, er eksempler på fibre som indeholder sådanne nanostrukturer. Undersøgelse og kvantisering af nanostrukturer i PPTA (og især deres porøse struktur) er hovedemnet for denne afhandling.

Røntgensmåvinkelspredning (SAXS) har mulighed for at karakterisere disse strukturer uden nødvendigheden af destruktiv prøvepreparation. Den udfordrende del af SAXS er dog analysen af de registrerede diffraktionsmønstre. SAXS-mønstre som skyldes PPTA-fibre indikerer tilstedeværelsen af orienterede nanostrukturer. Sådanne nanostrukturer kan ofte karakteriseres ved analyse af dele af SAXS-mønsteret under brug af metoder udviklet til isotrop spredning, som f.eks. Debye-Bueche-metoden og Porodmetoden til bestemmelse af størrelsesparametre. Andre anvendte metoder er den Effler Invariant og "Ruland Streak" metoden til bestemmelse af orienteringsgraden af de spredende partikler. Disse metoder bliver gennemgået og sammenlignet med målte og simulerede data for at give indsigt i avendeligheden af de traditionelle metoder.

En alternativ analysemetode præsenteres som fitter hele det todimensionelle spredningsmønster til en model bestående af fuldstændigt ensrettede polydisperse elipsoider, med den fordel at bestemmelse af størrelsesfordelingsparametre kan opnås. Denne analysemetode testes ved brug af simulerede data. Anvendelse af metoden på spredningsmønstre målt på PPTA-fibre giver et fornuftigt fit. Forbedringer af metoden sammenlignes, bestående af introduktionen af en orienteringsfordeling for at tillade mindre end perfekt ensretning af sprederne, og medtagelse af store spredningspartikler for at tage højde for effekten af fibrillar spredning i spredningsmønsteret. Fittet til spredningsmønsteret fra as-spun aramidfibre forbedres af introduktionen af større spredere, mens fittet til spredningsmønsteret fra de

varmebehndlede fibre forbedres når der tages højde for uperfekt ensretning. Som følge af varmebehandlingen øges den gennemsnitlige bredde og længde af spredderne.

Polymerfibrenes nanostrukturelle opførsel under aksial kompression og stræk er også undersøgt. Til dette formål blev der lavet en løkke for at opnå områder med henholdsvis kompression og stræk (under elastisk deformation) i dele af filamentet. Løkkens top (hvor krumningsradius er mindst, hvorved det påtrykte stræk bliver størst) blev dernæst belyst med mikrobeam-SAXS ved Swiss Light Source. SAXS data blev uddraget både fra komprimerede og udstrukne områder af det bøjede filament, hvilket viser oscilationer i de højest anisotropiske SAXS-mønstre. Dette indikerer regulære interne strukturer som sandsynligvis stammer fra revner eller glideplaner mellem tætpakkede grupper af fibriler. Oscillationerne kan modeleres som spredning fra en tætpakket matrix af bånd- eller cylinderformede objekter, hvis tilstedeværelse også understøttes af SEM-billeder. På indersiden af løkken hvor aksial kompression forekommer, udviser fibrilgrupperne fibrillar seperation i takt med aftagende løkkestørrelse, hvilket øger antallet af revner mellem de spredende elementer. Udsat for stræk pakker fibrillerne tættere, resulterende i at grupper af fibriller kan sprede som et samlet element samt at repetitionsafstanden mellem glideplanerne øges.

Endelig viser resultater fra indledende in-situ stræk- og opvarmningseksperimenter at nanostrukturen påvirkes af højt træk og moderate temperaturer. Trækpåvirkningen viser længdeforøgelse af hulrumsstrukturer, samt højere grad af orientering. Opvarmning påvirker (først og fremmest) længden af hulrummene som reduceres som følge af tilførsel af varme. Resultaterne af kombinerede opvarmnings- og strækforsøg viser at der opstår en kombination af disse effekter.

Foreword

Dear Reader,

Thank you for taking the time to read through (part) of this thesis. I hope that you may find it interesting and I hope you can use some parts of it for your own research. There is a Dutch custom to pour some thought into "Stellingen", a small sheet of statements, often containing insightful or witty thoughts related to the research and life in general, which the opponents may use as a starting point for asking questions during the defense. While this is not done in Denmark, I have decided to hijack the foreword for this purpose.

With only a few days left before handing in this thesis, the whole project can be summarised as a rollercoaster ride through many slightly stressful periods alternating with periods in between. The stressful periods are marked by periods wherein I had to hand in reports, applications or proposals, give presentations or perform measurements at the synchrotrons. The periods in between are filled with discussions, staring out the window, designing, programming Matlab and visualising data. Given the sheer contrast of the latter type of period with the former type, during the "relaxing" periods I often felt that nothing was achieved. This was partly solved towards the end as I started keeping a log of everything I did. Logbook-keeping is now an occupation which I can highly recommend to all those suffering from Ph.D. study depression somewhere halfway through their project. It is also reassuring here to quote the words from Mahatma Gandhi: "Whatever you do will be insignificant, but it is very important that you do it. You must be the change you want to see in the world".

Which nicely brings me to my next topic: The World and its relation to Ph.D. studies. I found that you will not gain any wisdom from a Ph.D. project. Instead you get knowledge and insight from it, and you have to translate that to wisdom through discussions and listening to others. Some excellent sources for wisdom are the talks from the TED (Technology, Entertainment, Design) conferences (http://www.ted.com/), and the stories from (foreign) BBC correspondents told in the "From Our Own Correspondent" radio programs (also conveniently

available on podcast). I sincerely think that the TED talks should be highly recommended (if not required) weekly viewing for all students, to broaden their minds and expand their world views. In addition to that, they will see what good presentation skills are, and with all this, gain the ability to bring themselves out of the natural isolation we place ourselves in.

Some things I have seen in the TED talks are amazing (naturally, not all talks are good, but an astoundingly large number are). I have seen theoretical particle physics explained in a most elegant manner from a surfer who researched while living in a van, driving around the island of Maui (Garett Lisi). The brain can be equally explained as long as it's done with enthusiasm (Vilayanur Ramachandran), genius can be explained in a humane way (Elizabeth Gilbert) and so can failure (Alain de Botton). Many talks also focus on aid work and the statistics involved (e.g. Hans Rosling, Al Gore) and showcase new technologies. Excellent music, art and photography also appears regularly, but most striking are the stories of personal development, such as recovery from severe depression (Sherwin Nuland), and stories of hopes and wishes (Dave Eggers, Karen Armstrong). There are now a near infinite number of excellent talks on there worth watching. In the (not so delicate) words of Ryan Sohmer (from his online comic blog): "Watch TED. You just might learn something of value".

Presentation skills in the academic world are also severely lacking. I think I understand why the public does not understand academics and academic research; we have lost the way of explaining to a layman audience. The presentations given by academics are too often filled to the brim with information, making it too easy for the audience to get lost between the stories the slides are telling and the stories of the presenter. Improving presentation skills will, therefore, benefit us, our audience and the public in general as we (re-)gain the ability to give talks. TED presentations are an excellent example, but much information can also be gleaned from following weblogs such as Presentation Zen (or, of course, by reading the book).

Presenting is all about visualising a story, through storytelling and supporting graphics. Making the graphics can be time-consuming in the beginning, but has helped me a lot to get insight into the problems encountered in the Ph.D. project. This made me realise that visualisation of data, even if only for sticking it in the logbook, can be incredibly valuable. Another way of looking at this is that half of your brain is geared towards interpreting visual information. If you are not visualising your data, therefore, you are only working with half a brain. No offense...

That said, it is very important to maintain a level of humour in science, and sci-

entists should not take themselves too seriously. This can be done by following the Annals of Improbable Research (previously known as the Journal of Irreproducible Results), which is full of scientists applying the right scientific methods to the wrong kinds of questions. The Ig-Nobel prizes are a part of this, and should help scientists keep their feet on the ground.

Finally, projects like this are never finished. And if I don't do this research someone else will. But that doesn't mean I should not do it, because I have learned a lot in the past three years, from supervisors, books, papers, videos, audiobooks, people in the field and people outside the field, and maybe one day I can tell you some of what I have learned. I have also learned that I am a rude, pretentious, overconfident young brat who knows nothing, and that I'll be that for a very long time to come. And I think that is a good thing.

Contents

Chapter 1

High-performance polymer fibres and their nanostructure

1.1 High-performance polymer fibres

Demanding applications require high-performance materials. Some demanding applications are bullet-proof or stab resistant vests, competition sails, mooring cables, fireproof clothing, high-performance tires, airplane wings, windturbines, and so on and so forth. These applications all benefit from the implementation of high performance materials. Some sought for properties may include high tensile strength, high modulus, heat resistance and low density. Many applications of high performance materials require the material to be in the form of a fibre, which can be braided or twisted into cables, woven into sheets, or embedded in other materials to form composites. Fibres, therefore, are the focus of this thesis.

Some available materials (both high-performance as well as more standard materials) are listed in Table 1.1. Two parameters, the tensile strength and modulus, have been plotted in Figure 1.1. These show that the region of high-performance materials are delimited by carbon fibres in the high-modulus region (high stiffness), and glass fibres in the low-modulus (low stiffness), high tensile strength region. Polymer fibres are situated roughly in the intermediate-modulus, high tensile-strength region. From this perspective, high-performance polymer fibres appear relatively unremarkable. This changes, however, when the density is taken into account. Most organic polymer fibres have a low density (as can be determined from Table 1.1), which makes the aramid type fibre, for example, several times stronger than steel on a per-weight unit basis, as shown in Table 1.2.

Choosing an appropriate fibre for a particular application also implies a careful selection of the fibre characteristics. Some examples of the selection criteria may be modulus, tensile and compressive strength, temperature and/or chemical resistance, resistance to radiation (UV or otherwise) and effects of moisture on the properties. Other examples are fibrillation properties, electric properties and processing properties. In high-performance applications, cost often plays a less important role.

1.2 The aramid polymer fibre, PPTA

One class of such high-performance polymer fibre that was "discovered" in 1965 and commercialized in the 1970s is the aramid (aromatic polyamide) polymer [Beyen, 2007; Tanner et al., 1989]*. This polymer consists of aromatic monomers linked using amide bonds, with properties approaching like rigid-rod polymers [Northolt and Aartsen, 1973; Weyland, 1980]. Hydrogen bonding interactions lead to sheet-like crystal structures, which contributes to the compression strength [Afshari et al., 2008]. The particular form of aramid polymer that this thesis revolves around is the para-aramid structure, described by its chemical name: poly(para-phenylene terephthalamide) (PPTA, shown in Figure 1.2).

PPTA fibres are characterised by their lack of melting point, high Young's modulus and tenacity (tensile strength), low creep and a low elongation at failure [Tanner et al., 1989] as well as good impact resistance [Afshari et al., 2008]. This makes them suitable for use in a wide range of applications. Additionally, by chopping the fibre into small parts followed by roughening steps, the fibre breaks up (fibrillates) and turns into a material with a woolly texture which can be used in applications such as asbestos replacements.

While the material has many beneficial properties, there are a few aspects which may affect its performance. These are its reduced resistance to some chemicals such as strong acids and gasoline [Chae and Kumar, 2006; Jiang et al., 1993], and its reduced resistance to radiation. The latter aspect was investigated in detail by Zhang et al. [2006], who found that the skin of the material is affected by prolonged (144 hours) exposure to simulated sunlight. The most significant physical response after this irradiation was a reduction of about 50% of the tensile strength of Twaron 2000 fibre, while the modulus remained mostly unaffected [Zhang et al., 2006].

*For a detailed treatment of the history of the commercialisation, the reader is referred to a paper by Tanner et al. [1989] and a book by Beyen [2007]

Table 1.1: *Comparison of some parameters of several well-known high-performance fibres.*

Material	Tensile modulus (GPa)	Tensile strength (GPa)	Compressive strength (GPa)	Density (g/cm^3)	Elongation at break (%)	Reference
Steel	200	2.8	-	7.8	1.4	[Chae and Kumar, 2006; Jiang et al., 1993]
Alumina	≈365	1.7	6.9	3.7	-	[Jiang et al., 1993]
S-Glass (fibreglass)	90	4.5	>1.1	2.46	-	[Jiang et al., 1993]
Carbon (pitch)	725	2.2	0.48	2.15	-	[Jiang et al., 1993]
Carbon (PAN)	585	3.8	1.67	1.94	-	[Jiang et al., 1993]
Carbon (HS)	230	2.1	2.1	1.8	1.5	[Afshari et al., 2008]
PPTA (Twaron, Kevlar)	91-130	3.1-4.1	0.32-0.68	1.44-1.47	2-3.4	[Afshari et al., 2008; Chae and Kumar, 2006; Jiang et al., 1993; Northolt and Sikkema, 1991]
PBO	80-280	2.31-5.5	0.4-0.68	1.5 -2.5	1.56-2.1	[Afshari et al., 2008; Northolt and Sikkema, 1991]
Zylon	180-270	5.8	-	1.54-1.56	2.5-3.5	[Chae and Kumar, 2006]
PBI	5.6	0.4	-	1.4	30	[Chae and Kumar, 2006]
PBT	325-331	4.1	0.68	1.58	-	[Jiang et al., 1993; Northolt and Sikkema, 1991]
PIPD (M5)	330	3.5-5	1.6	1.7	1.5-2.5	[Afshari et al., 2008; Chae and Kumar, 2006]
UHMW-PE	70-105	2.4-3.1	-	0.97	2.5-4	[Chae and Kumar, 2006; Jiang et al., 1993]
Vectran	65	2.9	-	1.4	3.3	[Chae and Kumar, 2006; Jiang et al., 1993]
Nylon	6	1.0	0.1	1.14	-	[Jiang et al., 1993]
PET	12	1.2	0.09	1.39	-	[Jiang et al., 1993]
Polyester	15	1	-	1.38	20	[Chae and Kumar, 2006]
Nomex 450	17	0.65	-	1.38	22	[Chae and Kumar, 2006]

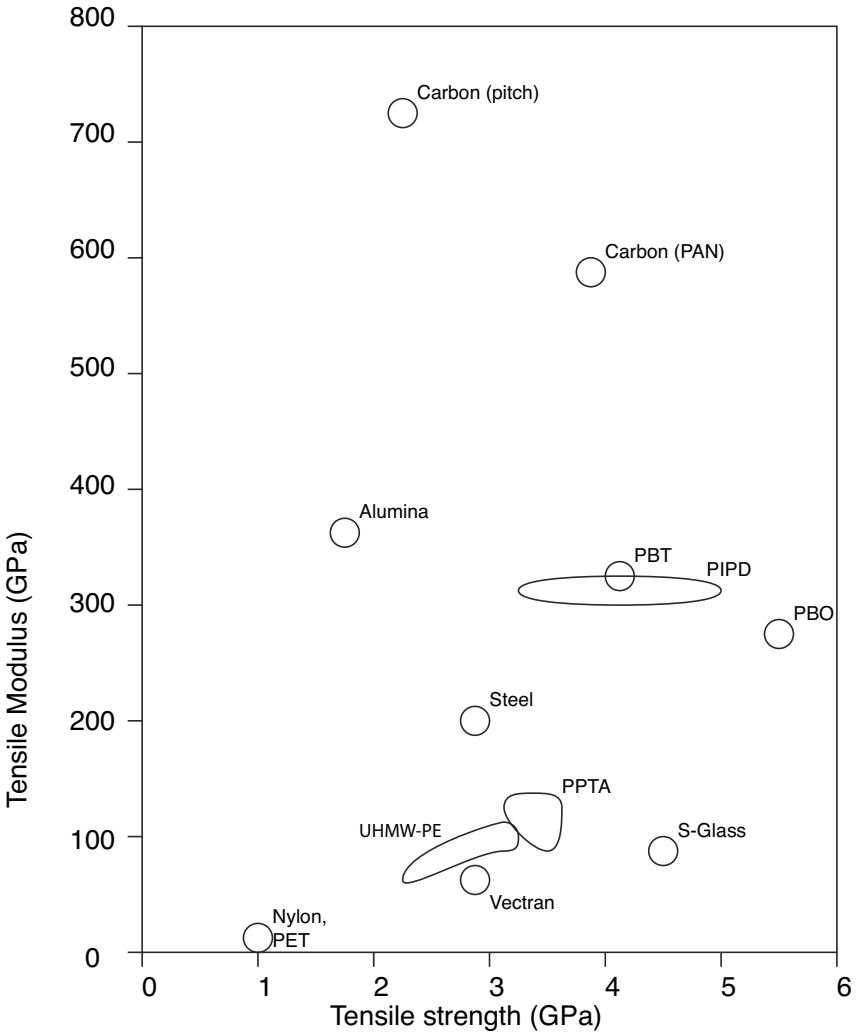

Figure 1.1: *Graphical comparison between the fibre strength and moduli for various materials, based on Table 1.1.*

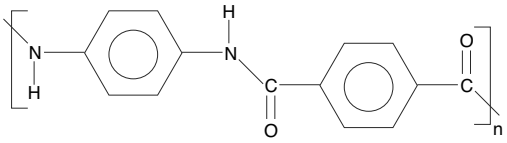

Figure 1.2: *The structure of PPTA.*

Table 1.2: *Specific tensile strengths of materials (tensile strength/density).*

Material	Specific tensile strength (GPa cm^3/g)
Zylon	3.74
UHMWPE	3.2
PIPD	2.94
PPTA	2.15-2.79
PBT	2.59
PBO	2.2
Vectran	2.07
Carbon (PAN)	1.96
S-glass	1.83
Alumina	1.22
Carbon (HS)	1.16
Carbon (pitch)	1.02
Nylon	0.88
Steel	0.34

The remarkable performance and properties of the fibre have sparked a wide range of investigations into the structure and spinning behaviour of the PPTA fibre [Chae and Kumar, 2006; Jiang et al., 1993; Northolt and Sikkema, 1991]. The goal of these investigations is to investigate links between the production parameters, internal structure and the final physical properties of the material. In order to attain a better view of the parameters and structure involved, the following sections will highlight some aspects of the production process and its impact on the structure and properties of the material. For a detailed treatment, the reader is referred to an excellent review article by Northolt and Sikkema [1991].

1.3 Manufacturing process of PPTA

1.3.1 Production

After polymerisation of para-phenylenediamine and terephthalic acid to form poly-(*p*-phenylene terephthalamide) (PPTA), the formed PPTA is dissolved in ≈100% sulfuric acid [Tanner et al., 1989]. Good spinning characteristics are obtained above 10 wt.%, usually close to 20%, since in this concentration range the solution is liquid crystalline at the spinning temperatures (≈ 80 degrees Centigrade) [Picken et al., 1992; Tanner et al., 1989; Weyland, 1980]. Below this spinning tem-

perature the polymer forms a crystallosolvate with sulphuric acid [Tanner et al., 1989; Weyland, 1980]. Local molecular order exists in the liquid crystalline domains due to inter-chain interactions as well as concentration effects in these rigid-rod-like polymer solutions [†]. On a macro-scale, a sufficiently relaxed (no shear) solution contains randomly oriented domains [Northolt and Sikkema, 1991; Picken, 1990].

In commercialized PPTA production methods, the liquid crystalline solution is forced through a spinning head, which contains small spinning holes, each producing its own jet of liquid crystalline solution which is later to become the filament (with an approximate diameter of 12 μm, c.f. Figure 1.4) [Weyland, 1980]. After traversing a small air gap, the polymer enters a coagulation bath in which the polymer undergoes a phase transition due to solvent exchange and changes in temperature. Here, each jet solidifies as a filament, and thus the fibre (a collection of many filaments, also known as a yarn) is formed. Structure formation mainly occurs in the air gap and coagulation bath.

It was found that if draw ratios larger than two were to be achieved, either the coagulation bath composition had to be changed, or the spinning head had to be placed above the coagulation bath in order to delay solidification of the polymer [Weyland, 1980]. Since the tenacity (tensile strength) as well as the modulus strongly relate to the draw ratio, either of the two had to be implemented [Northolt and Sikkema, 1991; Weyland, 1980]. Draw ratios of around 6 are published as common draw ratios for PPTA fibres [Picken et al., 1992].

After washing, stretching and drying steps, the so-called "as-spun" material has been produced (cf. Figure 1.3). We will discuss some aspects of this process individually as they are closely related to the formation of the internal structure.

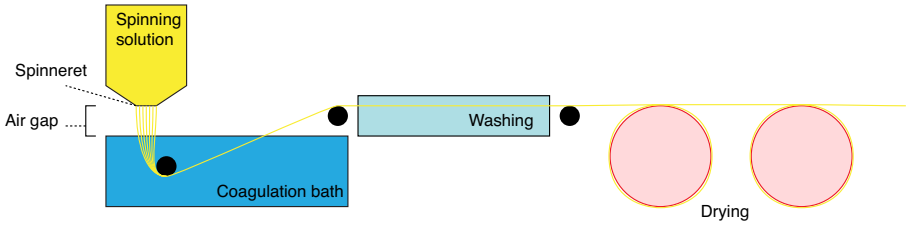

Figure 1.3: *Spinning process of PPTA fibres from a liquid crystalline solution.*

[†]For similar polymeric systems, namely PBA, a concentration-dependent orientation factor ranging from 0.76 to 0.83 was found. This orientation factor ranges from 0 for unoriented systems to 1 for perfectly aligned systems [Sartirana et al., 1986]

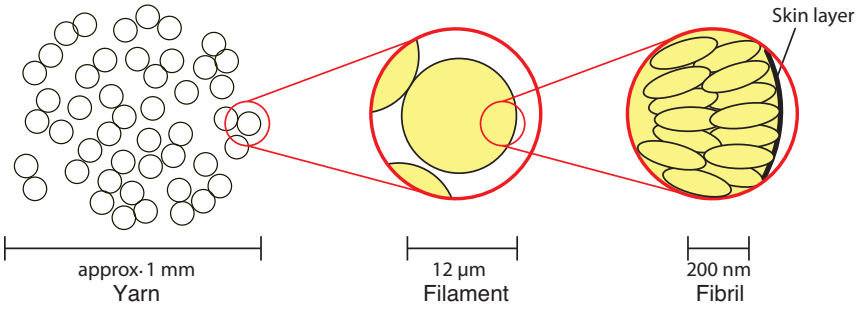

Figure 1.4: *Description of the terms "fibre", "filament" and "fibril" as used throughout this document.*

1.3.2 Structure formation during spinning

Structure formation takes place in the coagulation bath, and there is a significant (but complex) relationship between the manufacturing properties and the final product properties and structure [Picken et al., 1992]. Post-spinning treatment of the fibres may slightly influence the final internal structure and properties.

The crystallites orient due to several effects in the production process. In the sulfuric acid the polymer molecules align at high concentration, forming a liquid crystalline solution with domains of oriented polymer molecules. This orientation is dependent on the concentration and temperature of the spinning solution [Picken, 1990]. The elongational flow during spinning aligns the directors of the liquid crystalline domains, due to the spinneret effecting elongational as well as shear flow, and an additional elongational flow in the air gap and coagulation bath[‡] [Northolt and Sikkema, 1991]. Although there is some evidence that the strain rate does not affect the actual crystallite orientation as measured by *in-situ* wide-angle diffraction [Picken et al., 1990], optical measurements do indicate an improved orientation of the disclinations in the fibre [Kenig, 1987]. This apparent contradiction is addressed in [Picken et al., 1990] and later in [Picken et al., 1991] and [Picken et al., 1992].

[‡]It is interesting to note that a similar orientation effect of the elongational flow can be achieved by application of a strong magnetic field [Panar and Beste, 1977]

1.4 The internal filament structure

The internal structure of the filaments has been investigated in depth using a variety of techniques. Herewith a discussion of the aspects of the internal structure that have already been established. We will discuss the several levels and morphological expressions of the hierarchy below, starting from the crystalline structure and working our way up to the filament-scale effects.

1.4.1 Crystalline structure

The PPTA polymer can crystallise into several different structures. PPTA crystallises into a monoclinic lattice, with unit cell angles of approximately 90 degrees [Jain and Vijayan, 2004; Northolt and Stuut, 1978], which can also be described with the term "pseudo-orthorhombic" [Northolt, 1974].

There are two main modifications of the PPTA crystal structure, i.e. modification I and modification II. These are graphically shown in [Haraguchi et al., 1979a]. Modification II is thermodynamically least stable, and reverts to modification I upon annealing [Haraguchi et al., 1979a]. Therefore, Modification I is the modification most commonly found in commercial fibres spun from a high-concentration liquid-crystalline solution [Northolt and Sikkema, 1991]. From a low-concentration solution, modification II can sometimes be produced in films coagulated using specific coagulation bath compositions [Haraguchi et al., 1979b], although it remains challenging [Jackson and Chanzy, 1993].

The crystallites are monoclinic with unit cell angles of 90 degrees. The crystallite size is approximately $50\times50\times200$ Å [Northolt and Aartsen, 1973; Northolt and Sikkema, 1991], and the calculated crystal density is 1.50 g cm^{-3} [Northolt and Stuut, 1978; Yabuki et al., 1975]. The material in the fibres is highly crystalline (>99%), as no amorphous diffraction was observed in the diffraction pattern [Northolt and Sikkema, 1991; Panar et al., 1983].

While the angles and dimensions are universally accepted [Jain and Vijayan, 2004], there is some ambiguity regarding the exact space group of the crystal structure present in PPTA fibres [Jain and Vijayan, 2004; Liu et al., 1996]. The space group reported by Northolt [1974] is either P_n or $P2_{1/n}$ (shown in Figure 1.5, the full name of the latter group is $P1121/n$). Some forbidden reflections are visible (e.g. the 210,120, 320, and 410 reflections [Liu et al., 1996]), however, which have led to the suggested alternative space group P1a1 (brief name Pa) [Liu et al., 1996]. Neutron vibrational spectroscopy has provided new evidence supporting this alternative spacegroup [Plazanet et al., 2005]. Other explanations for the appearance

of forbidden reflections are the presence of stacking faults by [Jain and Vijayan, 2004].

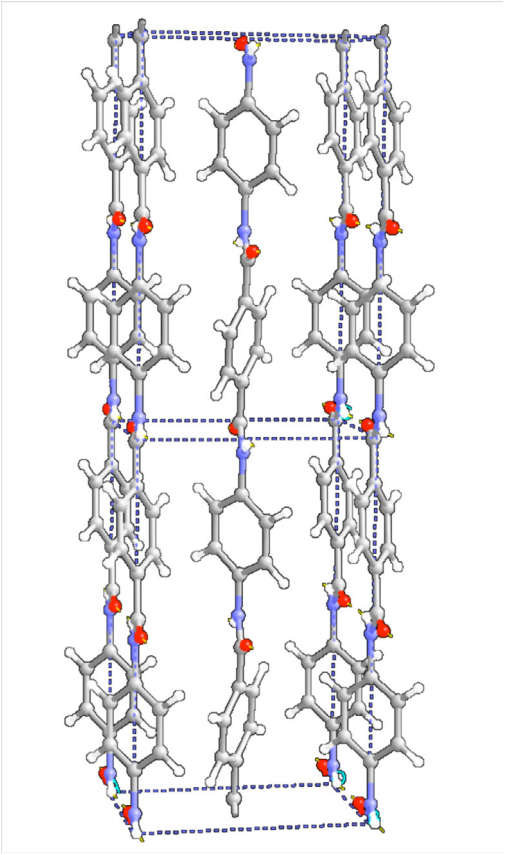

Figure 1.5: *Crystal structure of modification I as reported by Northolt [1974]. Image courtesy of dr. E. A. Klop.*

It is further noted that heat treatment affects the crystallite size, which subsequently increases in both the longitudinal and lateral dimensions [Northolt and Sikkema, 1991; Yabuki et al., 1975]. This has been visualised nicely for several Kevlar types by Jackson et al. [1994]. Heat treatment at temperatures up to 600 degrees Centigrade increases the longitudinal size to about 800 Å and the lateral size to about 100 Å [Jackson et al., 1994; Northolt and Sikkema, 1991; Yabuki et al., 1975]. A reduction in the lattice distortion parameter is concurrently observed [Yabuki et al., 1975].

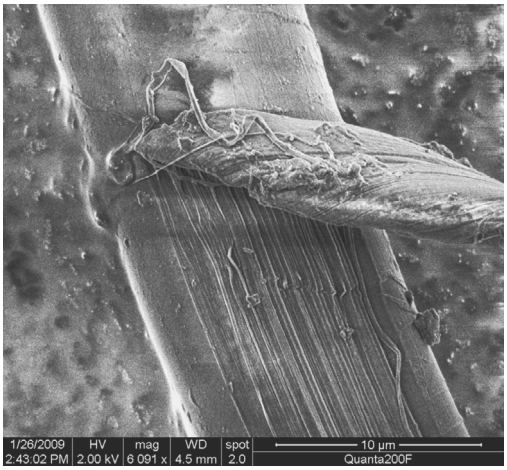

Figure 1.6: *Electron micrograph showing the fibrillar structure underneath the delaminated surface of a single as-spun PPTA filament.*

1.4.2 Fibrillar structure

The crystallites connect end-to-end, forming fibrils [Northolt and Sikkema, 1991]. Lateral connections (tie points) and weak interactions also bind crystallites with similar orientation of their hydrogen-bonded planes [Jungnickel, 1977]. Fibrils thus are large structures consisting of interconnected crystallites. These interconnected fibrils may be observed in Scanning Electron Microscopy images [Wang et al., 1993]. Two illustrative examples (which will return in another chapter of the thesis) are measurements performed at the DTU Centre for Microscopy, showing the fibrils beneath a layer of delaminated skin in the first image (Figure 1.6), and the fibrils extending to the core of the material in Figure 1.7. Additionally, the interconnectedness of fibrils are clearly visible from SEM micrographs taken on a high resolution SEM as shown in Figure 1.8.

The dimensions of the fibrils vary throughout the reports, from about 60 nm [Morgan et al., 1983] to 600 nm [Panar et al., 1983]. Sawyer et al. [1993] indicated that fibrils can be split up into smaller sub-fibrils (sometimes referred to as "microfibrils"), such that a hierarchy can be established. According to Sawyer et al. [1993] (in agreement with our findings), "microfibrils" are tape-like structures several tens of nanometers wide and several nanometers high (and approximated to have near infinite length). Fibrils consist of a packing of microfibrils and are tape-like structures about 500 nanometers wide, and ranging from 100 to 500 nanometers in height [Sawyer et al., 1993]. They furthermore classify "macrofibrils" as cylindrical structures of several micrometers in diameter. Since these dimensions

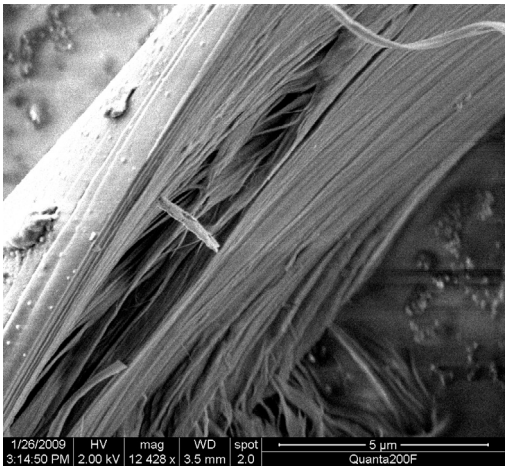

Figure 1.7: *Electron micrograph showing the fibrillar structure underneath the surface of a cut single filament of as-spun PPTA.*

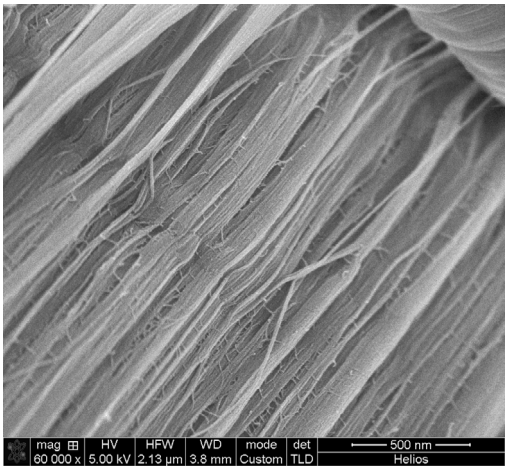

Figure 1.8: *Electron micrograph revealing an interconnected fibrillar structure underneath the delaminated surface of a single as-spun PPTA filament..*

Table 1.3: *Approximate size of objects in a PPTA fibre*

Structural level	shape	approx. size
Crystal unit cell	monoclinic	7.8×5.2×12.9 Å [Liu et al., 1996]
Crystallite	hexagonal prism [Jackson et al., 1994]	50×50×200 Å [Klop, 2009]
Microfibril	tape-like	2.5×20 nm [Sawyer et al., 1993]
Fibril	tape-like	0.5×0.5 μm [Sawyer et al., 1993]
Macrofibril	cylindrical	1-2 μm
Filament	cylindrical	12 μm
Fibre (Yarn)	pack of filaments	$\approx$ 0.5×0.5 mm

are found using microscopic methods (scanning probe microscopy, SPM), the observed size of the fibrils may very well be dependent on the fibrillation method, i.e. a rigourous fibrillation procedure may yield much smaller fibrillar dimensions than a careful fibrillation procedure. The approximate sizes of all the structures described above have been listed in Table 1.3.

1.4.3 Radial structure

A complex structure manifests itself inside the filaments during the spinning process. Firstly, a smooth skin is present around the filament. Inside this, a core-shell structure may be found, depending on the production process (c.f. Figure 1.9). It should be mentioned at this point, that most literature solely speaks of two distinctions in their observations (and thus usually refers to the structures as skin-core or core-shell where shell and skin are interchangeable). After consideration of the observations available in literature, however, it becomes likely that there are three distinct regions in the filament, which will be elaborated below (a similar division was suggested by Davies et al. [2008] as "skin, intermediate and core" regions). Additionally, the crystallites in the filament may orient radially, as can be observed by microbeam crystallography or lateral birefringence measurements. These aspects will be discussed here.

The skin around the (12 μm diameter) filament is a thin section of material (about 100 nm thick), where the polymer chains exhibit a random chain-end distribution in the axial direction (i.e. they are still aligned in the axial direction) [Morgan et al., 1983]. This skin is visible in the electron micrographs in Figure 1.6,

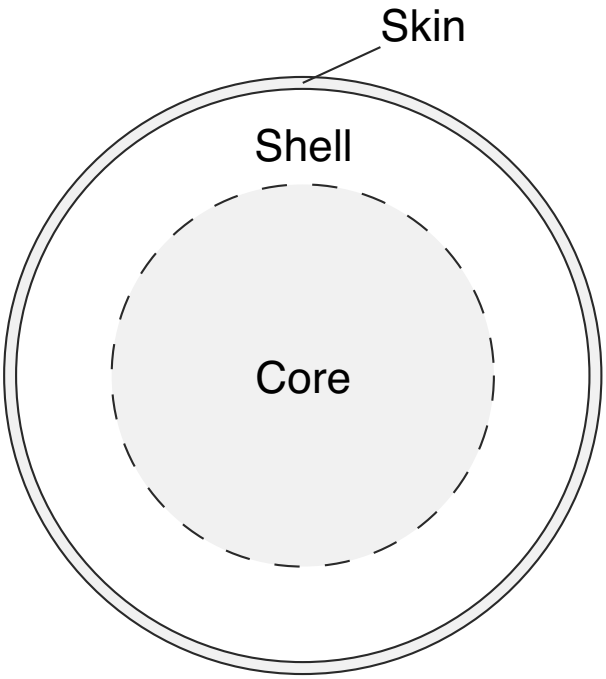

Figure 1.9: *The structural levels inside a filament.*

also observed by others [Horio et al., 1984], and shows up in microbeam diffraction patterns as regions with increased scattering at small angles (and an anisotropic scattering pattern) [Davies et al., 2008].

The core and shell regions both show an organisation of the crystallites resembling a smectic phase found in liquid crystals, indicating that the chain ends now are more or less aligned [Morgan et al., 1983]. These measurements may be supported by light diffraction measurements as shown by Roche et al. [1985]. The structure has been represented by Morgan et al. [1983], and is shown (redrawn) in Figure 1.10. The size parameters have been reproduced from the original article, but it should be noted that there is a lot of variation in the literature regarding the exact dimensions. This is not surprising, as it is most probably heavily influenced by the production method, and its determination is challenging. Over time, production methods of commercial fibres are optimized by changing production parameters (e.g. temperature, coagulation bath acidity, draw ratio, air gap length), leading to varying sizes of the internal structure over time.

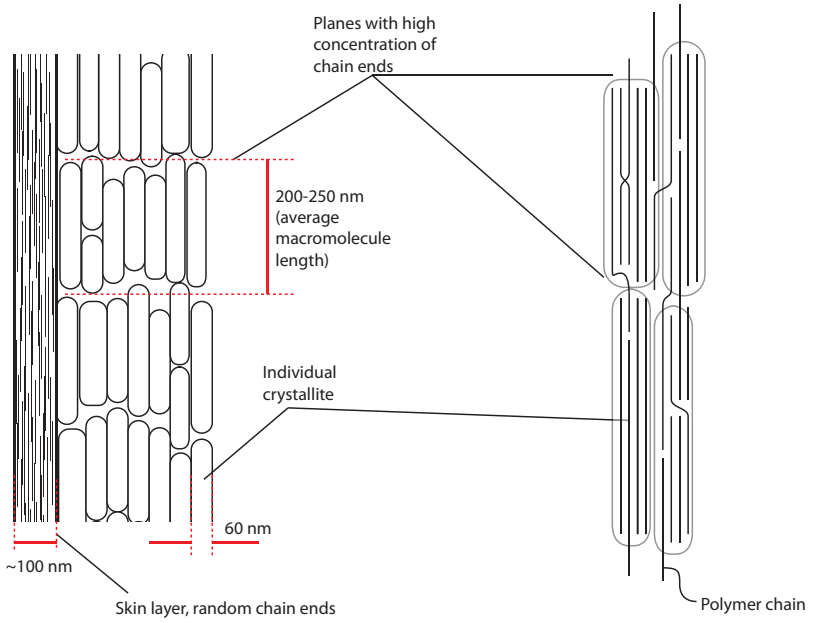

Figure 1.10: *The structure as proposed by Morgan et al. [1983], indicating the distribution of chain ends in the skin and inner (core and shell) regions of the filament. The right-hand image depicts the organisation of the polymer chains in the crystallites. Adapted from Morgan et al. [1983].*

Inside the skin layer, there may be a distinct difference between the core and the

shell of the material. Measurements by Riekel et al. [1999] indicate a reduced crystalline orientation in the core of the material, in agreement with the results from [Davis et al., 2000; Singletary et al., 2000; Yabuki et al., 1976][§]. Optical measurements using crossed polars to measure the periodicity of the pleated sheet structure (discussed below) also show differences between the core and the shell of the material [Northolt and Sikkema, 1991]. This difference between the core and the shell of the material has also been observed in more recent measurements by Davies et al. [2008].

One reason for the generation of the higher orientation in the shell of the material may be explained using a fibre formation model suggested by Davies et al. [2007] for PBO. It was similarly found that the degree of orientation for some PPTA fibres increases with distance to the fibre centre, whereas for other PPTA fibres this was not found to be radially dependent [Davis et al., 2000]. An alternative determination using X-ray microspectroscopy was performed by Smith and Ade [1996].

Upon the application of tensile strain on the filament, the degree of orientation in the filament increases, as observed by Riekel et al. [1999] and Davies et al. [2006]. This was most clear for Kevlar 29, where the regions with relatively low orientation (core) in the filament increased in orientation [Riekel et al., 1999]. This was supported later on by simultaneous Raman measurements [Davies et al., 2006].

1.4.4 Pleated sheet structure - structure parallel to the axis

An interesting observation with regard to the internal structure is that polarized light microscopy measurements reveal a periodic misalignment of the crystallographic axes with respect to the filament axis, so-called pleated sheets. The periodicity of this effect was determined to range from 200-1000 nanometers [Horio et al., 1984; Jiang et al., 1993; Morgan et al., 1983; Northolt and Sikkema, 1991; Panar et al., 1983].

The misalignment of the crystallites with respect to the fibre axis is determined to be about 5 degrees. Interestingly, the structure is more susceptible to degradation at the kink point [Panar et al., 1983]. Riekel et al. [1999] also showed that the degree of misalignment is reduced through the application of strain, and Kenig

[§]It should be mentioned here, that the paper discussing this determination is in Japanese, with the figures, tables and captions in English. When the works [Yabuki et al., 1976, 1975] are cited, therefore, conclusions have been drawn by interpretations on the figures and their captions.

[1987] showed that the degree of misalignment is dependent on the production process of the fibre as well.

The structure shown before from Figure 1.10 can be adapted to show the pleated sheet structure. This is visualised in Figure 1.11, where a 5 degree offset to the crystallites has been applied.

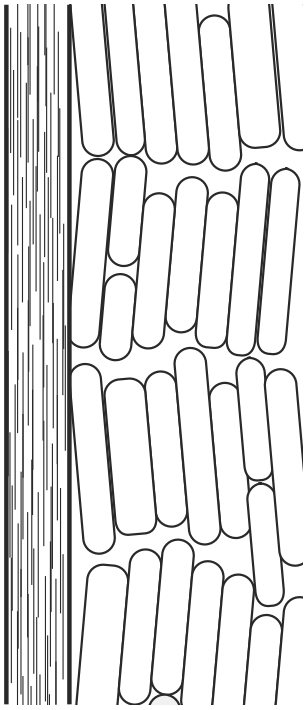

Figure 1.11: *The structure from Figure 1.10, adapted to correspond to the pleated sheet structure.*

1.4.5 Density considerations

The density of the fibre is approximately 1.43-1.45 g cm^{-3} (cf. Table 1.1). With regards to the high degree of crystallinity of the material, and the crystalline density being 1.50 g cm^{-3}, there is a fraction of voids in the material. Calculation shows that the filaments consist of about 95% crystalline polymer, which leaves about 5 % of void space.

From Table 1.1, we can see that the high-modulus forms of aramid fibre have a

slightly higher density than their low-modulus variants, indicating that the void fraction is also dependent on the production process and/or subsequent heat treatment procedures.

1.5 Void structure - Scope of this thesis

There is considerable evidence for the presence of a nanoporous structure in the filaments [Aerts, 1991; Jiang et al., 1993; Mooney and MacElroy, 2004; Northolt and Sikkema, 1991; Saijo et al., 1994]. Firstly, there is the difference between the crystalline density of PPTA (1.48 g cm^{-3}) and the macroscopic density of the material (which ranges from 1.45 to 1.47, depending on the production process [Chae and Kumar, 2006; Jiang et al., 1993; Northolt and Sikkema, 1991]). The absence of an amorphous diffraction signal indicates that little or no amorphous PPTA is present, so that the reduced density is likely to be due to about 5 volume% of voids. Furthermore, direct observations of a porous structure have been obtained through transmission electron microscopy by (amongst others) Dobb et al. [1979]. In other investigations the moisture uptake in the filaments is analyzed. The moisture is partially transported through and stored in a void structure [Mooney and MacElroy, 2004; Saijo et al., 1994]. Finally, the presence of a strong Small-angle X-ray Scattering (SAXS) signal strongly supports the presence of voids, especially since it is dependent on the moisture content [Dobb et al., 1979; Saijo et al., 1994]. The void structure appears analogous to that found in carbon fibres [Dobb et al., 1977], although it exhibits a lower aspect ratio [Northolt and Sikkema, 1991]. An alternative explanation for the existence of the SAXS signal is that this signal could also originate from an amorphous phase instead of a void structure [Grubb et al., 1991; Ran et al., 2001]. Ran et al. [2001] reached this conclusion partially since they did not observe a change in the SAXS pattern when subjecting PPTA fibres to moisture. In view of the investigations referred to above, it is at present commonly accepted that a void system is present in the fibres.

There is some discussion on the exact location of this void structure in the filament. Panar et al. [1983] places the bulk volume of the voids in the centre of the filament, and discusses this choice with respect to a paper by Dobb et al. [1979]. The observation by Dobb is based on transmission electron microscopy results on stained filaments, whereas Panar interprets his findings based on etching and dyeing behaviour of filaments. These voids are elongated to several hundred Å in the direction of the fibre axis, and several tens of Å in diameter [Northolt and Sikkema, 1991]. Their cross-section either have circular symmetry, or are randomly oriented around the fibre axis, as intermediate-angle microbeam

scattering experiments show a circularly symmetric scattering pattern. This may not be true for the skin layer, however, where anisotropic scattering patterns were observed [Davies et al., 2008].

This thesis concerns itself with the investigation of this void structure in particular and its relation to the surrounding filament nanostructure. While the thesis revolves around the manifestation of this structure in PPTA fibres, the techniques are more broadly applicable.

This thesis will firstly introduce and expand on the main applied technique of Small-Angle X-ray Scattering (SAXS), explaining firstly why it was chosen, secondly how it works, and lastly how its results are interpreted using the classical techniques. The subsequent chapter will investigate the analysis of the scattering patterns as a whole, using a novel analysis methods, and discuss its application to PPTA fibres. Next, peculiar findings for bent filaments are presented and interpreted. Lastly, a conclusion is drawn on the applicability of SAXS to characterise the nanostructure.

Chapter 2

Small-angle X-Ray scattering

2.1 Introducing SAXS

Small-angle X-Ray Scattering as used in this thesis, can be considered as an elastic X-ray technique*. These techniques rely on the wave nature of radiation to produce interference patterns upon interaction with matter. Due to the nature of the X-ray radiation applied, and due to some machine characteristics, the typical length scale of nanostructure probed by SAXS ranges from about 1 to 1000 nanometers (the larger sizes, beyond several hundred nanometer, are commonly reached by highly optimized systems). This size range places the technique solidly in between Wide-Angle X-ray Scattering/Diffraction (WAXS/WAXD) and (optical) microscopy techniques. It can complement details seen by electron microscopy techniques, and can be directly compared to those.

Advantages of SAXS, as compared to microscopic methods, are that the technique determines the average nanostructure of the entire irradiated section (which is usually on the order of 1 mm^3). This is done with virtually no sample preparation, as the only requirement of the sample is that it is thin enough for radiation to pass through. For most polymeric materials, this is usually on the order of a millimeter, metallic samples must be much thinner due to their high absorption of X-rays. As an alternative to thinner samples, the energy of the X-rays can be increased,

*Other examples of techniques using the elastic properties are Wide-angle X-ray diffraction and Laue diffraction. Besides the elastic techniques, there is the group of non-elastic scattering techniques, such as Extended X-ray Absorption Fine Structure (EXAFS) and X-ray Absorption Near-Edge Spectroscopy (XANES). The latter group relies on the particle nature of radiation and probes the electronic structure of matter. Some techniques use both the elastic and non-elastic scattering properties, such as resonant scattering and Anomalous Diffraction.

reducing interaction of the radiation with the sample material, thus increasing the allowed sample thickness. SAXS, furthermore, does not require a thorough preparation or destruction of the sample to the level required by microscopic methods. This non-destructive feature allows for in-situ studies, probing the evolution of reactions, or the behaviour of samples in a non-equilibrium state[†].

The main disadvantage of SAXS is that it does not provide a real-space image of the nanostructure. Instead, it is the Fourier transform of the electron density contrast distribution in the sample (which will be elaborated upon shortly). This makes even the qualitative analysis of such scattering patterns not straightforward, and requires some experience or knowledge of Fourier transforms of structures. Often, the scattering pattern cannot be uniquely translated to a structure, and therefore requires some assumptions supported by information extracted from direct-space techniques such as various forms of microscopy. With this additional information, the structural parameters may then be resolved from SAXS.

When time and effort is invested, however, SAXS can provide quite some information about the sample which is normally quite difficult to obtain otherwise. Information such as the volume fraction of nanostructure, shapes, sizes, and orientation can be extracted in a variety of situations (e.g. heated samples, wetted samples, etc.).

2.2 A short introduction to scattering theory

2.2.1 The basics of scattering

The basis of most scattering techniques based on EM radiation, such as crystallographic techniques, lies in the interaction of incoming radiation with the sample. Imagine two electrons being irradiated by an incoming electromagnetic wave, consisting of an electric and a magnetic field. The electrons respond to the electric field (due to their charge) and will oscillate with the same frequency as the field supplied by the incoming wave [‡]. When the two electrons oscillate, they emit radiation at the same frequency as their oscillation. If these two electrons are situated in close proximity, this radiation can interfere (c.f. Figure 2.1). When the emitted

[†]Since radiation is used, however, the duration of such tests may be limited to the lifetime of the sample when exposed to radiation

[‡]the electrons usually oscillate with the same, or virtually the same frequency (also known as "elastic" interaction with the incoming radiation). There are, of course, exceptions to this ("inelastic" interactions, mentioned in a previous footnote) which can be exploited, but they are not relevant to this thesis and have therefore been omitted.

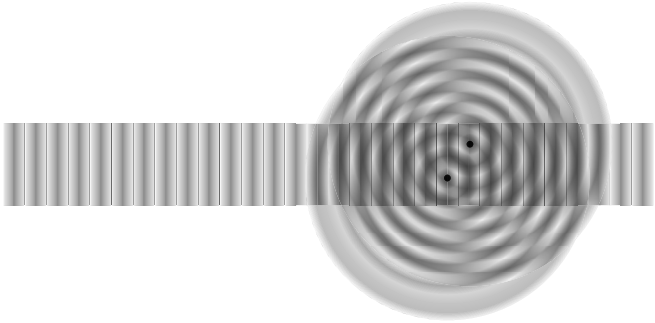

Figure 2.1: *Two electrons oscillating with an incoming EM wave and emitting interfering waves themselves.*

radiation is observed from a distance, the interference causes the appearance of maxima and minima in the detected intensity of the radiation.

Practical scattering experiments differ from this idealised situation in several aspects, but the essence remains valid. The differences are that in practice:

- The incoming wave is replaced by a superposition of waves that are roughly in phase within a certain volume of space
- The experimental sample consists of many electrons instead of just two
- The detector cannot observe the scattering amplitude (and thus cannot resolve the phase of the scattered radiation), but instead detects the scattering intensity (photon flux) striking the detector surface. Further instrumental limitations also affect the observed intensity pattern.

These three aspects will be discussed in detail in the following paragraphs, with special emphasis on the second and the third aspect, as they are of specific relevance to this thesis.

Some useful equations related to the behaviour of waves

Since photons can be considered to have a particle as well as a wave nature, they can be described using either. The de Broglie relationships link the kinetic energy E, momentum p, wavelength λ and frequency ν. Since radiation can be described by any of these, it is useful to keep the following equations at hand:

$$\lambda = \frac{h}{p} \tag{2.1}$$

Here, h is the Planck constant. Similar equations can be established for an electromagnetic wave linking the angular wavenumber k, angular frequency ω, frequency ν and energy E:

$$k = \frac{2\pi}{\lambda} = \frac{2\pi\nu}{v_p} = \frac{\omega}{v_p} = \frac{E}{\bar{h}c} \tag{2.2}$$

where v_p is the propagation speed of the wave and equal to c for waves travelling in vacuum, and $\bar{h} = \frac{h}{2\pi}$ is the reduced Planck constant. The value for the Planck constant is 6.626×10^{-34}Js $= 4.136 \times 10^{-15}$eVs.

The electric field amplitude of an electric field propagating along the x-axis, can be expressed as a sine wave in its real form $E_0 \sin(kx)$ or in its complex form $E_0 \exp i(kx)$, where $k = \frac{2\pi}{\lambda}$ is the wavenumber. The electric field of EM radiation can be parameterized in vector notation using a single equation [Als-Nielsen and McMorrow, 2004]:

$$\mathbf{E}(\mathbf{r}, t) = \hat{\epsilon} E_0 \exp i(\mathbf{k} \cdot \mathbf{r} - \omega t) \tag{2.3}$$

where $\hat{\epsilon}$ is the polarisation vector (the direction of the oscillatory field), t is the temporal component, $\mathbf{k}$ the wavevector along the direction of propagation.

The intensity of radiation emitted by an electron oscillating in an electric field is related to the intensity of the incoming radiation by the Thompson equation:

$$I_e(\theta) = I_p \frac{T}{R^2} = I_p \frac{\frac{e^4}{m^2c^4} P}{R^2} \tag{2.4}$$

Where I_p is the intensity of the incoming radiation, T the product of the square of the so-called classical electron radius ($r_e^2 = \frac{e^4}{m^2c^4} \approx 7.90e-26$, e is electron charge, m electron mass and c the speed of light) with the angle-dependent polarisation factor P. R denotes the distance between the electron and the "detector".

The polarisation factor is dependent on the source of the X-rays, and direction of observation. For synchrotron radiation, the incoming radiation is polarised in the horizontal plane, making the polarisation factor for observations in the vertical plane equal to 1, and for observations in the horizontal plane equal to $P = \cos^2(2\theta)$, where 2θ the scattering angle. For unpolarised sources, $P = \frac{1+cos^2(2\theta)}{2}$. When small angles are considered, the polarisation factor in all cases can be approximated to 1.

To calculate the position of constructive and destructive interference for two point scatterers, it can be shown that this is dependent on the relative locations in 3D space of the two scattering centers, using two special, easy to calculate cases (c.f. Appendix A). We can then consider the more complex case of two arbitrarily

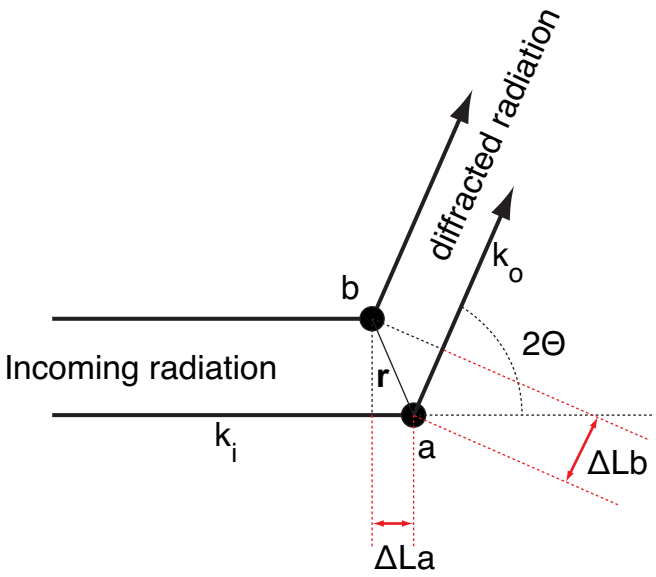

Figure 2.2: *Two electrons positioned arbitrarily with respect to the incoming radiation, oscillating with an incoming EM wave and emitting interfering waves themselves.*

positioned point scatterers, as shown in Figure 2.2. We see here that the difference in pathlength is the sum of ΔLa and ΔLb. These can be written as the projection of $\mathbf{r}$ onto $\mathbf{k}_i$ and $\mathbf{k}_o$ respectively, where $\mid \mathbf{k} \mid = \frac{2\pi}{\lambda}$:

$$\begin{aligned} \Delta La &= \mathbf{r} \cdot \mathbf{k}_i \\ \Delta Lb &= \mathbf{r} \cdot \mathbf{k}_o \\ \Delta L &= \Delta La + \Delta Lb \\ &= \mathbf{r} \cdot (\mathbf{k}_o - \mathbf{k}_i) \\ &= \mathbf{r} \cdot \mathbf{q} \end{aligned} \tag{2.5}$$

The last part of this equation is our definition of $\mathbf{q}$, defined as:

$$\mathbf{q} = \mathbf{k}_o - \mathbf{k}_i \tag{2.6}$$

with magnitude

$$q = \mid \mathbf{q} \mid = \mid \mathbf{k}_o - \mathbf{k}_i \mid = \frac{2\pi}{\lambda} 2\sin(\Theta) \tag{2.7}$$

as shown graphically in (Figure 2.3). The phase difference caused by this pathlength is:

$$\Delta\Phi = \mathbf{q} \cdot \mathbf{r} = 2\sin(\Theta) \mid \mathbf{q} \mid \cdot \mid \mathbf{r} \mid \tag{2.8}$$

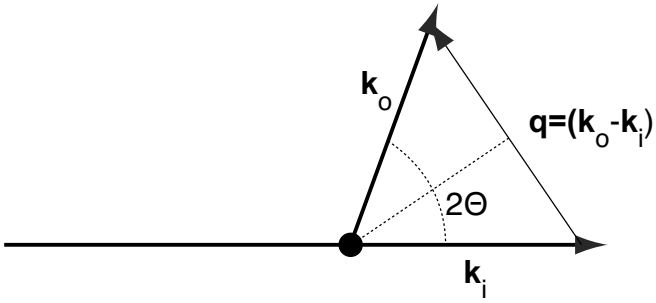

Figure 2.3: *Definition of* $\mathbf{q}$ *as* $\mathbf{k}_o - \mathbf{k}_i$.

2.2.2 Incoming waves - coherence volumes

Only a small fraction of the incoming waves actually interact with the electrons in the sample. This means that performing scattering experiments requires high-flux sources producing high intensity waves. In the visible region of the EM spectrum, lasers are commonly used for two reasons: lasers are a high-flux source, and secondly produce monochromatic radiation (the monochromaticity is important for reasons discussed shortly hereafter). For the X-ray section of the EM spectrum, a variety of sources are available. Most X-ray sources, however, do not produce monochromatic radiation.

The monochromatic radiation is of importance in scattering experiments, as a local volume at the sample position has to be established, where the waves are in phase. The size of this volume depends partially on the monochromaticity of the beam. This volume is often referred to as the "Coherence volume", as it is the place where the waves produce coherent EM fields. If the waves are not in phase, scattering effects do not take place, or take place to a lesser extent (depending on the degree of coherence).

The size of the coherence volume dictates the upper limit of the size of the scattering objects participating in the scattering effect. This means that attempts of detecting a structure of 1000 nanometers will not work with a coherence volume that is only 100 nanometers in the transversal directions, i.e. perpendicular to the direction of travel of the waves [Veen and Pfeiffer, 2004]. The size of the coherence volume is dependent in the transversal direction on the size of the beam-defining aperture and the distance from the aperture to the sample position (see for example the effect of a slit on the coherence volume in Figure 2.4, the larger the slit, the smaller the coherence volume, but the higher the intensity of the radiation). Distance from the optical element such as the slit, increases the transversal coherence

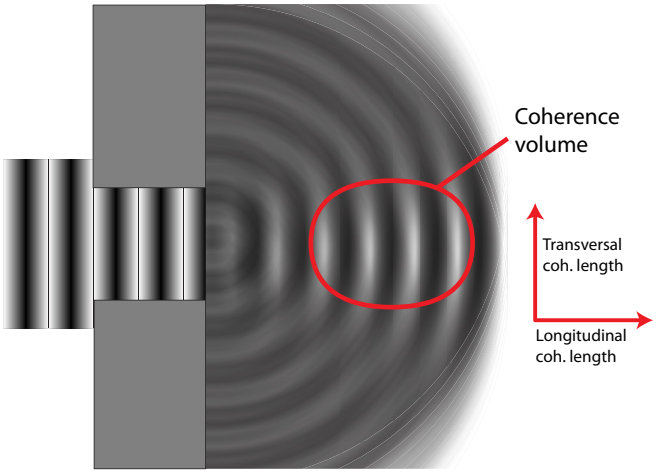

Figure 2.4: *Coherence volume after a slit. The larger the slit, the smaller the transversal coherence length.*

length. In the longitudinal direction, the coherence length is dependent on the monochromaticity of the radiation. Polychromatic beams have small longitudinal coherence lengths [Livet, 2007].

In many X-ray experiments, the irradiated sample volume is many times the size of such a coherence volume. In these samples, many coherence volumes exist, and thus scattering occurs from each of these coherence volumes. Some experiments, however, do exploit special characteristics of scattering from a single coherent volume. These will not be discussed here, but comprehensive descriptions of these have been established by Livet [2007] and Veen and Pfeiffer [2004].

The EM radiation used in this thesis is mainly low-energy X-rays, with a wavelength ranging from about 0.1 to several Ångström. This has only minor implications on some derivations as this restriction allows for some assumptions about the interaction between radiation and matter to be made. Most of the techniques used with X-rays, however, can be transposed onto techniques using other radiation, such as neutron sources and other techniques using EM radiation such as light scattering and vice versa.

2.2.3 Many-electron systems interaction with radiation

Samples contain many electrons. The computation of the scattered amplitude from a system with many electrons can be considered as the interference (sum) of

all waves emanating from each electron in the coherence volume[§].

The equation for the amplitude from a multitude of point sources can be written as:

$$A(\mathbf{q}) = -r_0 \sum_j \exp(i\mathbf{q}\mathbf{r_j}) \tag{2.9}$$

where r_0 is the Thompson scattering length if dealing with single electrons, j the index of the scattering source (electron), and $\mathbf{r_j}$ the position of the scattering centre.

For samples with continuously varying electron densities, the sum can be replaced by an integral. This makes the resulting equation into a Fourier transform function, which has great benefits for computational purposes. The scattering amplitude is the Fourier transform of the electron density difference (contrast) in the sample. The amplitude scales proportionally to the electron density contrast in the sample, the volume fractions of the phases and to the irradiated volume (c.f. Equation 2.13).

The Fourier transform of the electron density distribution over the correlation volume v therefore becomes:

$$A(\mathbf{q}) = -r_0 \iiint_v \rho(\mathbf{r}) \exp(i\mathbf{q}\mathbf{r}) \mathrm{d}v \tag{2.10}$$

2.2.4 Intensity - not amplitude - is detected

In most X-ray scattering experiments, the intensity of the scattered radiation is detected, and not the amplitude. The intensity of the scattered radiation can be computed from the electron density (in each correlation volume) by calculation of the absolute square of the amplitude (as obtained from Equation 2.10):

$$I(\mathbf{q}) = \mid A(\mathbf{q}) \mid^2 \tag{2.11}$$

The scattered intensity from many correlation volumes within the sample is detected by the detector. This means that the radiation that is scattered to a certain

[§]For the scattering experiments in this thesis, it is not strictly necessary to discuss coherence volumes, as we will not talk about coherent scattering experiments at all. However, as coherent scattering experiments become more common, it may prove useful to have touched upon the concept of coherence volumes. Additionally, it is important that the maximum size of the scatterers that can be detected by a SAXS instrument is not only limited by its geometry, but also on the coherence of the source [Livet, 2007; Veen and Pfeiffer, 2004].

angle is the incoherent sum of the scattering from a number N of correlation volumes in the sample [Livet, 2007], and therefore:

$$I(\mathbf{q}) = \sum_{i=1}^{N} I_i(\mathbf{q}) \tag{2.12}$$

The total scattered intensity for a two-phase system is proportional to Stribeck [2007]:

$$\iiint I(\mathbf{q}) d\mathbf{q} \propto V_{irr} \nu_1 \nu_2 (\rho_1 - \rho_2)^2 \tag{2.13}$$

where V_{irr} is the total irradiated volume, ν_i is the volume fraction of phase i and ρ_i is the electron density of phase i. This has been derived for multi-phase systems as well Ciccariello and Riello [2007].

2.2.5 Small-angle X-ray scattering instruments

Overview

Three major types of small-angle scattering instruments are available today. These are the Kratky camera, which is a camera employing an X-ray beam with a line-shaped cross-section, The Bonse-Hart instrument, which uses crystals (one monochromator and one analyser crystal) to select a very small portion of the scattered beam, and finally a pinhole- or slit-collimated instrument which uses an X-ray beam with a small circular or (nearly) square cross-section. This last type is the instrument which is the focus of this thesis, and will be expanded on in detail in this chapter.

The SAXS instrument consists of several sections, each of which will be discussed in detail. A schematic picture of a three-pinhole collimated SAXS machine is shown in Figure 2.5. It consists of an X-ray generator, a monochromator (which doubles as a focusing device), a collimation section, a sample chamber, a flight tube and a detector. In the following paragraph we will discuss each part individually.

Source

Various sources are available today for the generation of X-rays. Some of these are available as laboratory instruments, others are dedicated large-scale research facilities. We will discuss here some of the available sources.

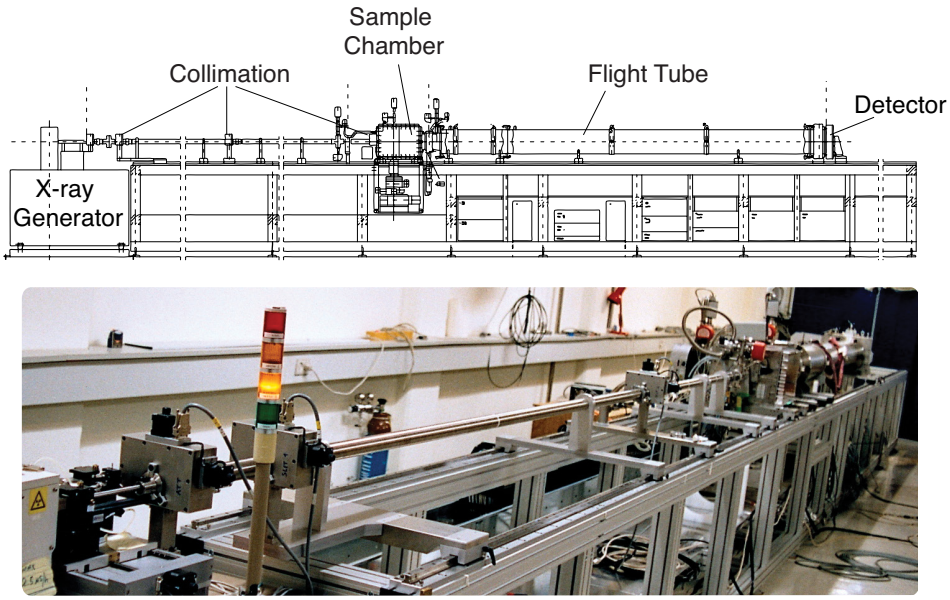

Figure 2.5: *Schematic depiction and photograph of the SAXS machine at DTU Risø*

Lab based sources started with the advent of the x-ray tube [Als-Nielsen and McMorrow, 2004]. The x-ray tube uses an electron-emitting (hot) filament cathode. The released electrons accelerate in an electric field towards the (water-cooled) anode. As the electrons hit the anode, x-rays are generated. Depending on the anode material, the characteristic wavelength of the radiation can be selected. The power of the anode is limited by the cooling method, and therefore a rotating anode has been developed. This anode consists of a rotating drum, which is water-cooled from the inside. Connecting a water-cooled drum that rotates at high speed in a vacuum chamber was one of the reasons why this type of generator only came about after the 1960's. The heat load using this drum is thus spread out over a much larger area than compared to a (static anode-based) x-ray tube, allowing for much more efficient cooling and a higher operating power (and more radiation).

Even higher intensities are obtained in particle accelerators (electron or proton) used for high-energy physics experiments. The bending magnets in those accelerators cause a deviation of the particle path, which subsequently emits radiation. The first accelerator-based x-ray experiments consisted of parasitic experiments besides the high-energy physics experiments. When it became evident that much good science could be done through the use of this radiation for (for example) materials science purposes, dedicated X-ray synchrotrons became available (sometimes as hand-me-downs from the particle physics experiments, such as the PETRA III

and DORIS synchrotrons at the DESY institute in Hamburg).

Because the search for higher intensities continued, "insertion devices" such as wigglers were placed in the straight sections of the synchrotron (between the bending magnets). These bend the particle path several times in s-curves by subjecting the particle to opposing magnetic fields (thus "wiggling" the electrons). The intensity from each wiggle in a straight section can then be added. A further (and most recent) improvement was achieved by wiggling the particles just so, that the emitted wave from each wiggle would constructively interfere with the next wiggle. The intensity from two oscillations is then not two (as with the wiggler) but four times as high. These insertion devices are called undulators and are found in most modern beamlines.

Monochromatisation

The source of X-rays for use in a SAXS machine has to be reasonably monochromatic, so that the required correlation length can be reached. In addition to the correlation length requirement, the accuracy of the measured scattering is also dependent on the wavelength spread, since the scattering vector $\mathbf{q}$ is dependent on the wavelength. A polychromatic beam, therefore, will smear out any scattering effects on the detector.

Several monochromatization methods exist, depending on the accuracy required. The first commonly used monochromator consists of a thin foil of metal. The absorption edges of the metal can then be used as a one-sided filter. For copper Kα radiation, for example, which commonly originates from x-ray tubes and rotating anodes which use copper as anode material, a nickel filter can be used. The monochromatization using such filters is very limited. Similarly, x-ray mirrors, which depend on the energy-dependent specular reflecting capabilities of some surfaces, can be used as a high-energy cut-off filter (as the higher the energy, the lower the required angle of incidence) [Freund, 1993].

Single-crystal monochromators are highly monochromatizing optical elements, which depend on a bragg-reflection from a crystalline material. The bragg condition of a perfect crystal is dependent on the wavelength, and thus only radiation within a certain energy window is diffracted. Using multiple bounces, the energy and divergence can be further fine-tuned Freund [1993]. Curved crystals can also be used for focusing the beam. Similar monochromatization and focusing effects can be achieved through fabrication of a "multilayer" mirror, which consists of many layers of deposited material, and works on the principle of bragg diffraction from stacked layers.

Collimation

Collimation of the beam is the shaping of the beam achieved through placement of various devices in the beam path. These devices usually consist of either circular pinholes in absorbing material or sets of parallel slits. Circular pinholes have the advantage that the final beam shape is circular, but the size of the pinhole is constant, and thus only a limited set of beam sizes can be selected (depending on the number of different pinholes in the collimation system). Slit collimation creates a square beam, which is less ideal, and requires two more motor drives. It has the advantage, however, of having a near infinite number of sizes and shapes (rectangular, naturally).

For 2D SAXS purposes, a two-pinhole or two-slit collimation has often been used[¶]. The second slit, however, still introduces a considerable amount of scattering, as a large amount of radiation passes the edge of the pinhole. This led to the introduction of a third pinhole or slit in the system, that does not touch the primary beam, but removes the scattering from the second pinhole or slit (cf. Figure 2.6) [Glatter and Kratky, 1982; Pedersen, 2004].

The diameter of the direct and parasitic beam scattering on the detector is related to the pinhole sizes and distances between the pinholes through [Pedersen, 2004]:

$$\Delta = R_3 + \frac{L_3(R_2 + R_3)}{L_2} \tag{2.14}$$

with parameters defined in 2.6.

Sample positioning

Sample positioning is usually performed using orthogonally placed linear motor drives, i.e. one drive for motion in the horizontal direction perpendicular to the beam, and one in the vertical direction. In specific cases, however, additional alignment is required. Samples for grazing incidence and crystallography may also need rotational alignment around the three orthogonal axes (and sometimes additional translation stages are required). One new, elegant sample stage incorporating many of these motions is the hexapod or Stewart platform, consisting of a plate held aloft by six canted linear actuators [Stewart, 2009]. This plate has six degrees of freedom (3 orthogonal translations and three orthogonal rotations, with

[¶]1D SAXS systems sometimes work with a line-shaped beam, in a Kratky-type camera. These are very useful for measuring liquid or unoriented samples, and may also be used for measuring oriented samples, but will not be discussed here.

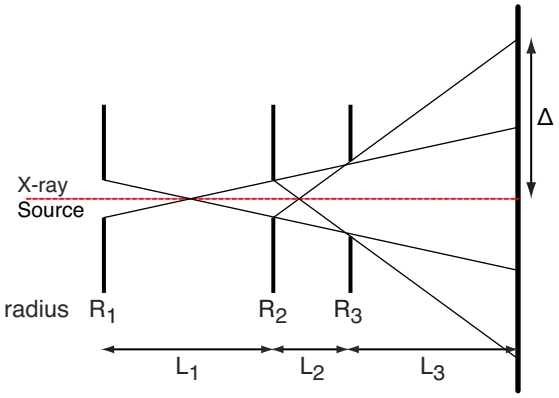

Figure 2.6: *Three-pinhole collimation parameters. Redrawn from [Pedersen, 2004].*

no fixed axes relative to its base plate (i.e. the centre of rotation can be defined by the user).

Flight tubes

Given the length of the SAXS machine and the scattering and absorption of X-rays by air, the collimation system and the space between the sample and detector are almost always filled with vacuum tubing, although the latter tube is sometimes filled with helium instead of evacuated (this is for example done at the SLS cSAXS beamline to allow the use of a thin, large exit window). Other systems are completely evacuated, consisting of a continuous in-vacuum space [Pedersen, 2004], and thereby reducing absorption and scattering effects of x-ray transparent windows. The latter of course is the most ideal from a data collection perspective, but limits are then imposed on the type of sample holders that fit within the vacuum enclosures.

Detection

X-ray detection systems depend on the transfer of energy from the x-ray photon to the detection system [Morse, 1993]. The X-ray is then either fully absorbed or fully transmitted, and therefore X-ray flight paths cannot be detected. The absorbed energy is subsequently transferred to an electrical system and then assigned to a value. The absorbed energy can be detected in four different ways (depending on the energy): by ionisation of a gas, liquid or solid, through excitation of optical states, by excitation of lattice vibrations (phonons) and through breakup of cooper

pairs in superconductors. Most common for SAXS are scintillation-based and ionisation-based detection systems [Graafsma, 2009].

Detectable parameters are the photon flux, photon energy, position, arrival time and polarisation [Graafsma, 2009]. For SAXS, only the flux and position are required, and the goal of the SAXS detector is to detect these parameters with a signal-to-noise ratio which is as high as possible. The detectors can detect these parameters in four different operating modes: current (flux-) mode, integration mode, photon counting mode and energy dispersive modes. SAXS detectors commonly consist of photon counting detectors or integration-based counting detectors [Graafsma, 2009].

These two most commonly consist of a gas-ionisation detector, where an incoming photon ionises a gas inside the detector. The ionised particles are subsequently accelerated due to an imposed electric field, ionising more gas along the way. Eventually the cloud of ions reaches a detector wire, causing an electrical pulse on the wire which is then detected. The intensity of the pulse is roughly related to the intensity of the incoming photon, and a coarse energy discrimination can be used to filter out (cosmic) background radiation as well as "double" photon events. An alternative (improved) ionisation based detector is the semiconductor detector, which has a plate of semiconducting material directly accessible to X-rays. One such detector is the PILATUS detector, developed by the SLS detector group [Eikenberry et al., 2003]. This detector detects photons through the change in conductivity in a semiconductor when a photon strikes. It is a low-noise photon counting system, with near-absolute position detection (only limited by the size of the pixel, as it has no point spread function like the gas-based detectors have [Né et al., 1997]).

Another common type of detector is the CCD-type integrating detector. This detector commonly consists of a scintillation screen to convert the X-rays to visible light and detects this light using a commercial CCD element used in (f.ex.) digital cameras. The advantage is that it is able to withstand much higher flux than the ionisation-based detectors, but it has significant drawbacks. It is generally not a single-photon counting device, and the obtained intensities are therefore in arbitrary units (although calibration can be done). These types are not energy discriminating, and cosmic radiation may therefore be observed. It also tends to have a drift in the gain, a high background level and relatively long readout times (which is a drawback for time-resolved experiments).

Chapter 3

Simulated scattering

3.1 Single 1D profiles

In order to explore some aspects of the relationship between scattering and the scatterer, it is illustrative to start by considering 1D structures before moving to 2D structures. These 1D structure models will furthermore be used in chapter 5 to explain scattering observed in looped filaments.

A 1D structure can be considered as the projection of a cross-section of material. One scatterer shape that will be discussed further on in this thesis is an infinitely long cylinder, oriented with its main axis perpendicular to the X-ray beam. This cylinder only scatters in one plane, namely that perpendicular to its axis. We can therefore simulate the scattering from this cylinder as the scattering from the electron density in the cross-section through the cylinder in that direction. This is shown in Figure 3.1. The cross-section of the cylinder is a circle. If this density is projected along the direction of the X-rays onto a 1D line, we obtain the electron density shown to the right of the structure in Figure 3.1. It is these projections that we will concern ourselves with for the remainder of this chapter.

3.1.1 Calculating the scattering from projected electron densities

In short, Fourier transformation of the projected 1D electron density profile of this structure will result in the scattered amplitude of our virtual radiation, according to Equation 2.9.The scattered intensity can then be computed from $I(\mathbf{q}) = \mid A(\mathbf{q}) \mid^2$ [Stribeck, 2007]. However, the numerical Fourier transform only defines the density

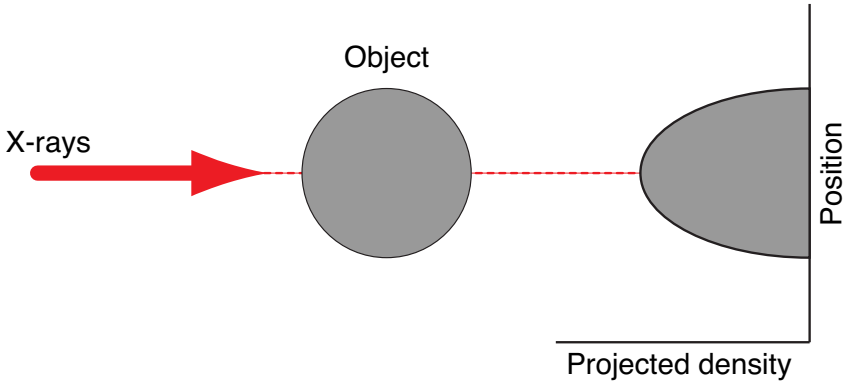

Figure 3.1: *Projection of the 2D shape onto a 1D line.*

at the sampling points —as discrete peaks— whereas the density is more accurately described as a continuous function. This has an effect on the simulated intensity at higher angles, which will be too high. In order to correct for this discrepancy, the discrete peaks in the electron density have to be convoluted with an inter-peak space-filling box function, i.e. with a box function which has the real-space width of the distance between the sampling points . This convolution in real-space can be replaced by a elementwise multiplication in Fourier-space of the Fourier transform of the density with the Fourier transform of the box function. This will improve the intensities at higher angles, and is described in more detail by Schmidt-Rohr [2007].

In order to simulate the scattering from infinitely long objects with a range of cross-sections, a superellipsoidal cross-section was chosen as a basis for the following simulations*. Superellipsoids can assume a variety of shapes, including diamond-like, circular and lamellar shapes. In detail, the following steps are taken in order to calculate the scattering pattern from *oriented*† superellipsoidal profiles numerically: For the shape projection, the electron density profile of a superellipsoidal cross-section projected onto a line is used as a basis (c.f. Figure 3.1). We start from the equation for a superellipse [Weisstein, 2008]:

$$\left|\frac{x}{a}\right|^n + \left|\frac{y}{b}\right|^n = 1 \tag{3.1}$$

*The simulation software, complete with a graphical user interface (GUI, under the name of EDsel_gui_v2.m), are described in the appendix, chapter B.

†These simulations assume not only that the main axis of the infinitely long scatterer is perpendicular to the X-ray beam, but furthermore assume that the cross-section is also oriented in a specific way with respect to the beam. Any isotropicity, therefore, is not considered in this simulation.

with a the radius of the superellipse in the direction of x, and b the radius of the superellipse in the direction of y. The parameter n defines the resulting shape, which is square for $n \to \infty$, ellipsoidal (or spherical, if the aspect ratio $a/b = 1$), diamond for $n = 1$, and astroid for $n = \frac{2}{3}$ [‡] (c.f. Figure 3.2). All intermediate and extrapolative shapes can be obtained.

The area of the profile (important for scaling of the intensity) is given by:

$$A = \frac{4^{1-\frac{1}{r}} ab\sqrt{\pi}\Gamma\left(1+\frac{1}{r}\right)}{\Gamma\left(\frac{1}{2}+\frac{1}{r}\right)} \tag{3.2}$$

Rewriting equation 3.1 to project the shape onto a line (see Figure 3.1, and substituting $y = \rho(x)$, we obtain for the electron density $\rho(x)$,

$$\rho(x) = 2b\left(-\left|\frac{x}{a}\right|^n + 1\right)^{\frac{1}{n}} \tag{3.3}$$

The factor 2 originates from the projection on the line. It is clear that the radius (b) of the object in the direction parallel to the beam (y) has no effect on the shape of the resulting scattering plot, but only on its scattered intensity, and can therefore be left out. Relative corrections of the intensity contributions for the scattering "volume" will be performed separately when necessary (for example in polydisperse systems). Several projected electron density profiles are shown in Figure 3.2.

The scattered intensity from this profile can be determined by calculating the absolute square of the Fourier transform of the electron density, or by calculating the Fourier transform of the autocorrelated electron density ($\rho(x)^{*2}$) [Stribeck, 2007]:

$$\begin{aligned} I(q) &= \mid \mathrm{FT}(\rho(x)) \mid^2 \\ &= \mathrm{FT}(\rho(x)^{*2}) \end{aligned} \tag{3.4}$$

We can improve the intensity decay of the numerical discrete Fourier transform (implemented in Matlab as the "fft" function) at higher angles by convoluting the intensity with the Fourier transform of a box function with the width of the distance between the sampling points as mentioned on page 48. This is performed using the following computation for m dimensions

$$I(\mathbf{q})_{\text{corrected}} = I(\mathbf{q})\left[\prod_{m=1}^{3} \frac{\sin(q_m a/2)}{q_m a/2}\right]^2 \tag{3.5}$$

[‡]Piet Hein's "superellipse" can be obtained by setting $n = \frac{5}{2}$, resulting in Sergels Torg (Stockholm, Sweden) with $\frac{a}{b} = \frac{6}{5}$ or his table with $\frac{a}{b} = \frac{3}{2}$.

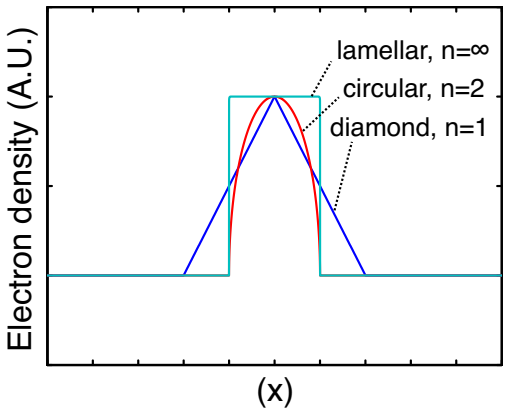

Figure 3.2: *Several simulated (electron) density profiles, simulated using the superellipsoidal profile scattering.*

where a is the distance between the sampling points. The function after the product can be recognised as the analytical fourier transform of a box (lamellar) function: the squared "sinc" function ($\frac{\sin(q_m a/2)}{q_m a/2}$), with a radius of the box of $a/2$. Matlab has several peculiarities to take into account. The first is that the Fourier transform implementation puts the zero frequency component in the corners of the resulting transform, requiring the execution of a "fftshift" operation to the resulting data in order to shift this to the center. Furthermore, for even matrix sizes (as opposed to odd-sized matrices), the zero frequency component cannot be placed exactly in the center and the result then requires the elimination of the first datapoint (row and column or three slices for 2D and 3D images, respectively), to make the resulting matrix centrosymmetric again. These have all been correctly applied in the ("EDsel") Matlab code used for the simulation.

3.1.2 Results for various cross-section shapes

Cylinder

If this numerical computation is performed for the previously shown infinite cylinder, and we define its radius R as 100 Ångström, a scattered intensity is obtained as shown on the right-hand side of Figure 3.3 [§]. What can be observed is a periodic

[§]The reader is aware that the height of the simulated profile is "1" While this initially appears to be erroneous, changing the height of the profile only affects the vertical scaling of the resulting scattering pattern. The aspect ratio of a single lamellae oriented in the direction of the beam can therefore not be determined without working in absolute units.

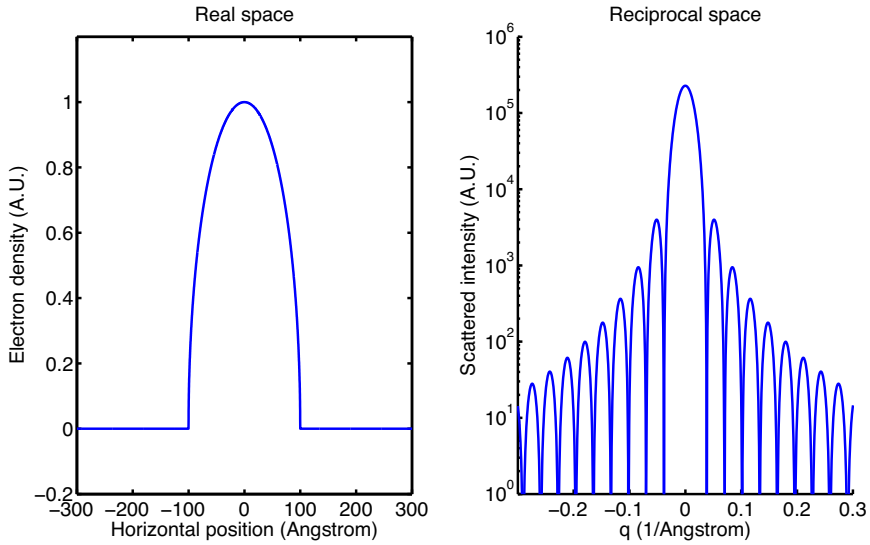

Figure 3.3: *Projected electron density and equatorial scattering intensity of an infinite, oriented cylinder*

oscillation, dipping to low values every $\delta q = \frac{\pi}{R}$ Å^{-1}. The position of the first dip in the scattering pattern is at $q/R = 3.83(1) \times 10^{-4}$. When the scattering plot is plotted on a double logarithmic scale (Figure 3.4), we see that most of the scattering curve, apart from the onset and final part, follows an $I \propto q^{-3}$ relationship.

We can now verify the validity of this numeric simulation by comparing this with the analytical scattering function for a single, *oriented* cylinder, as reported by [Oster and Riley, 1952]:

$$A(q) = 2. * \frac{J_1(qR)}{qR}; \tag{3.6}$$

Where R is the radius of the cylinder. Figure 3.5 shows this comparison between numerical and analytical curves, which agrees perfectly.

Lamellar profile

A lamellar profile can be construed by setting the value n in equation 3.3 to a high value (in this case 100). A profile and scattering pattern as shown in Figure 3.6 is then obtained. The position of the first dip in the scattering pattern is here $q/R = 3.142(6) \times 10^{-4}$, and the periodicity of the dips is (again) $\delta q = \frac{\pi}{R}$ Å^{-1}. In a double logarithmic plot, the slope of this curve is $I \propto q^{-2}$ (not shown

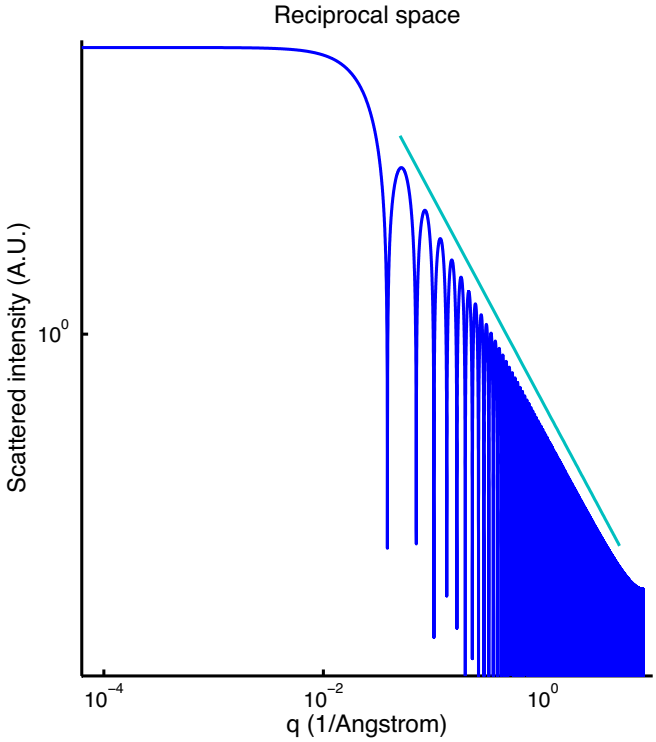

Figure 3.4: *Projected electron density and equatorial scattering intensity of an infinite, oriented cylinder on a double logarithmic scale. The additional line follows an* $I \propto q^{-3}$ *relationship.*

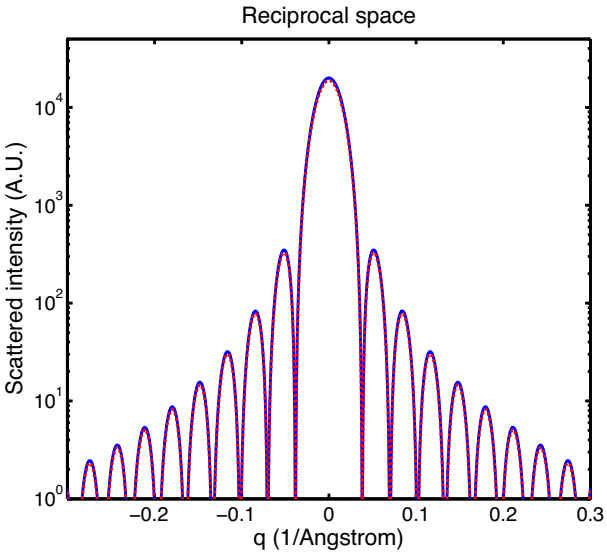

Figure 3.5: *Comparison between the intensity of the numerical (dashed red line) and analytical scattering function of a cylinder (continuous blue line).*

graphically). For this shape an analytical function exists as well (the previously described "sinc"-function), as given by Pedersen [1997] (adapted for a perfectly oriented lamella):

$$A(q) = \frac{\sin(qR)}{qR} \tag{3.7}$$

This comparison is not shown graphically, but when performed, forms a precise match to the numerically obtained result.

Diamond shape

The diamond shape is an interesting shape, as it is identical to a lamellar shape with a square cross-section, but rotated 45 degrees. Furthermore, it is indistinguishable from a triangular profile. It is also identical to a lamellar shape when the electron density gradient at the interface is considered to be finite and linear, as opposed to the previously assumed infinite shape. This means that the scattering amplitude can be computed using a convolution of the lamellar shape and a linearly decaying electron density gradient. The smoothing function used in this case is again a lamellar shape, as indicated by Vonk [1973]. Thus, our analytical scattering amplitude now is the Fourier transform of the convolution of the lamellar

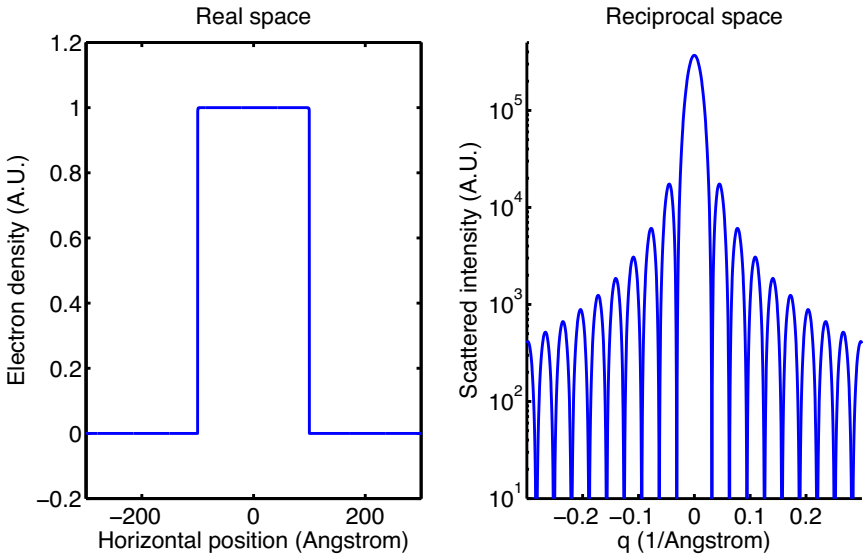

Figure 3.6: *Projected electron density and scattering intensity of an infinite, oriented lamella*

electron density function with the lamellar-shaped smoothing function:

$$A(q) = \frac{\sin(qR)}{qR} \frac{\sin(q\frac{E}{2})}{(q\frac{E}{2})} \tag{3.8}$$

Where E is the total width of the smoothing function (and thus of the interface region of the structure). We can obtain the scattering amplitude of the diamond shape by setting $\frac{E}{2} = R$.

The result of the numerical computation is shown in Figure 3.7. Most notably, the width of the profile is twice as large, whist the periodicity in the scattering pattern remains equal to that for the previously discussed structures. This means that for diamond-like shapes, the periodicity of the dips in the scattering pattern is no longer $\delta q = \frac{\pi}{R}$, but instead $\delta q = \frac{2\pi}{R}$. If, however, we see the diamond profile as a lamellar profile with smoothed electron density boundaries, it becomes apparent that the radius of the lamellar structure is only half that of the diamond-like structure (this lamellar structure is drawn as a dotted line in Figure 3.7). The intensity of the scattering pattern is proportional to $I \propto q^{-4}$, which also can be inferred from equation 3.8. The position of the first dip for this structure (of double width to the previous two structures), lies at $q = 0.03142(6)$.

Here we see clear evidence of the effect that isotropicity would have on the scattering pattern of scatterers with a non-circular cross-section. As mentioned before,

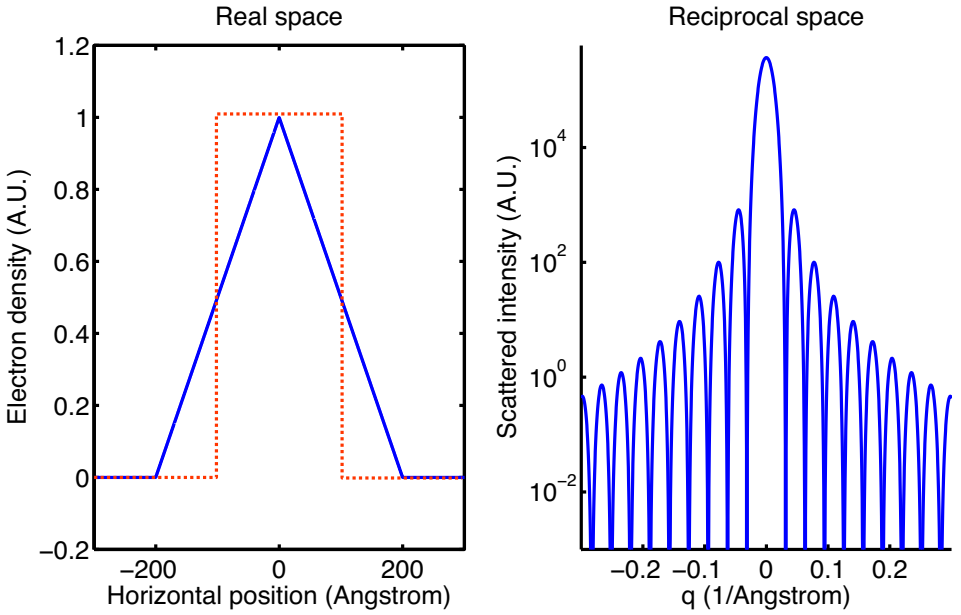

Figure 3.7: *Projected electron density and scattering intensity of a diamond profile. Dotted line indicates the lamellar structure.*

this shape can be related to the lamellar shape, albeit rotated by 45 degrees around the main axis. The intensity decay power, however, is very different, indicating that rotationally isotropic systems of a lamellar structure would have an intensity decay power in between that of the anisotropic lamellae ($I \propto q^{-2}$) and anisotropic diamond profile ($I \propto q^{-4}$).

Superellipsoids - intermediate shapes

By varying only the n value, thereby changing the curvature of the anisotropic superellipsoidal profile, an impression could be obtained of the range for the first dip position, periodicity of the dips and intensity decay power. This can prove to be valuable information when fitting periodic scattering patterns of unknown (but perfectly oriented) structures. When such a series of computations is done (and automatically analysed) for superellipsoidal profiles with a fixed width (100 Ångström), the following results are obtained:

For superellipsoidal profiles below $n = 0.3$, no oscillations are observed, and no straight section in a log-log plot is observed. Therefore, analyses of slope can only be done beyond $n = 0.3$. Periodic oscillations start appearing at $n = 0.7$.

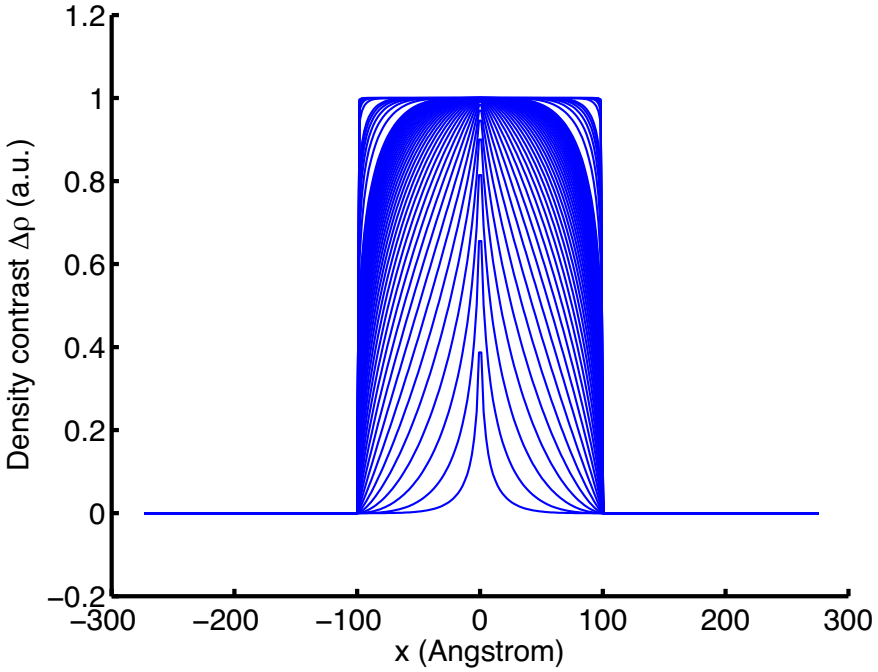

Figure 3.8: *Projected electron density profiles of superellipsoidal scatterers ranging from* $n = 0.3$ *to* $n = 80$.

The superellipsoids are simulated for $n = 0.3 \ldots 4$ in steps of 0.1, after which $n = 5 \ldots 10$ in steps of 1, and finally for $n = 10 \ldots 80$ the stepsize is 10. The electron density profiles are shown in Figure 3.8. Beyond 80, the code is unable to cope with the high powers. The total width of the simulated real space is 1×10^6 Ångström, quantised using 2^19 points (powers of two are recommended for speedy computation of the Fourier transform).

The determintation of the q-power law that the intensity is proportional to, is determined in the q-range from $q = 0.04 - 0.3$. It is fit using an iterative procedure, which for oscillatory data only uses the intensities at the peak positions. The position of the first dip is determined by following the intensity from the maximum downwards. The first q-value at which the intensity is smaller than the next point is considered the q-position of the first dip. The analysis routine subsequently searches for the next peak and dip and so on to determine the position of each dip. The periodicities and standard deviation of the periodicity is computed from this set of dip positions. In the case of $n = 0.7$, which is a special case as the dips

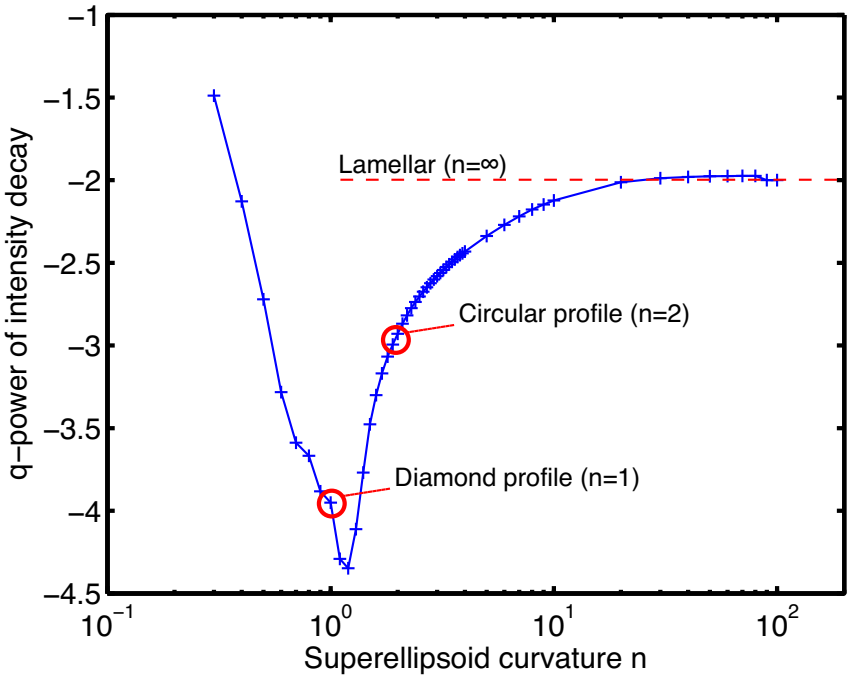

Figure 3.9: *q-Powers of the intensity decay of oriented (i.e. not rotated around the main axis) superellipsoidal scatterers ranging from $n = 0.3$ to $n = 80$.*

are only slightly visible, the slope was determined in the range $0.04 - 0.7$, and the position of the first dip was manually determined.

The results of these analyses are shown in Figures 3.9, 3.10 and 3.11. We can observe the following:

With respect to the determined slopes (determined in the range of $q = 0.04 - 1$), there are some slopes which have been determined to be below $I \propto q^{-4}$. Given that the slope was determined on the latter section of the scattering patten, this could be considered an effect similar to the effect of graded interfaces. At $n \approx 1$, the effect of the superellipsoidal function is a change in corner shape of the superellipsoid, similar to the effect graded interfaces would have on the electron density. This also exhibits itself as the appearance of a second periodic structure at higher q. The slopes for the sharp diamond profiles range from -1.5 for very sharp profiles to -4 for profiles close to triangular shapes (straight edges). It must be said, however, that the first scattering pattern, the one exhibiting a slope of -1.5, does not show much of a straight section in the double logarithmic plot and therefore the determined

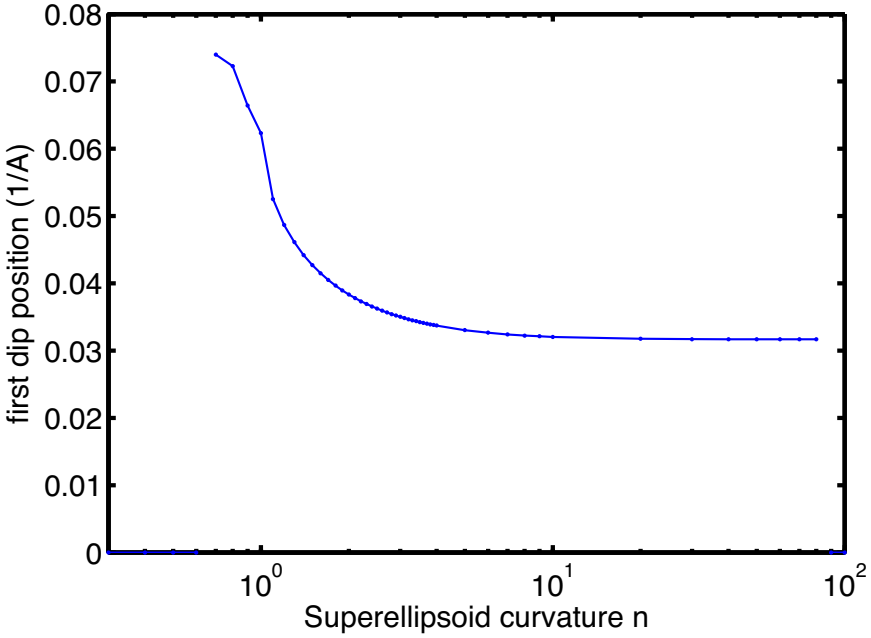

Figure 3.10: *position of the first dip in intensity in the scattering pattern of superellipsoidal scatterers ranging from $n = 0.3$ to $n = 80$.*

slope is less accurate than the other determined values. When increasing the curvature to create a circular cross-section results in a smooth transition between a slope of -4 for the triangular shape to -3 for the circular shape. Going to a lamellar shape reduces the slope further to -2. Therefore, if only a slope (other than -4) is known of a measured scattering pattern of aligned structures, the shape causing the scattering may be either of (at least) two possible shapes: a concave or a convex shape.

Regarding the position of the first dip for these simulated profiles, clear information about which shape causes the scattering can now be found, as the first dip has a unique, characteristic position in the scattering pattern. This can be seen in Figure 3.10, where the position of the first dip in the scattering pattern ranges between 0.074 $Å^{-1}$ to 0.03 $Å^{-1}$. This position of the first dip, however, is dependent on the size of the scatterer as well. This size information is usually obtained from the periodicity in the scattering pattern. We will now determine whether this is also possible for scattering patterns of superellipsoidal profiles.

The determined periodicity over the q-range of $0.01 - 1$ $Å^{-1}$ is shown in Figure

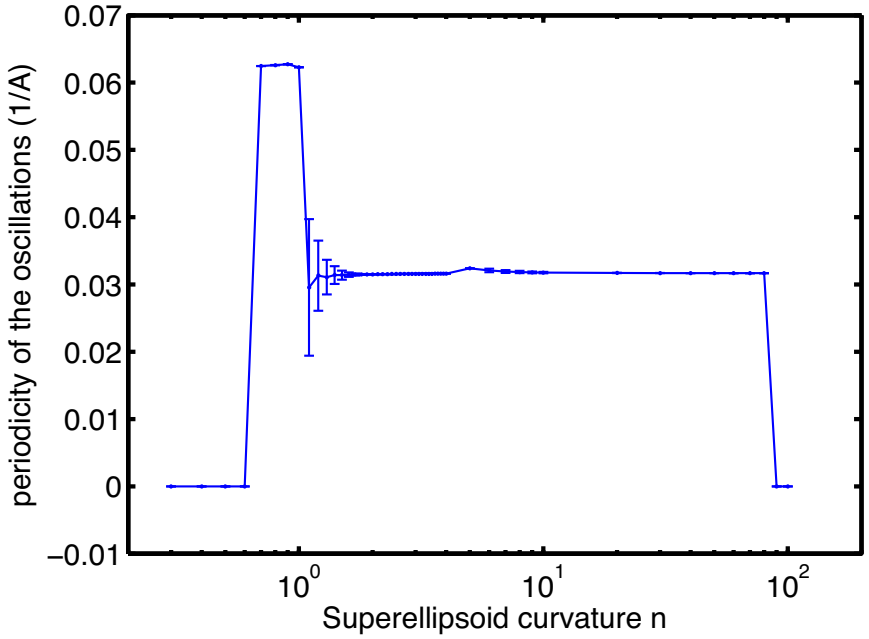

Figure 3.11: *Periodicity of the oscillations in intensity of superellipsoidal scatterers ranging from* $n = 0.3$ *to* $n = 80$.

3.11. The error bars indicate the standard deviation of the periodicities found throughout the scattering pattern. The curve indicates that for (concave) objects below $n \leq 1$, the periodicity is related to its size by $R\Delta q_{dip} \approx 2\pi$. In the scattering patterns (not shown) for the scattering patterns of superellipsoids with curvatures between $n = 1$ and $n = 2$, two patterns with different periodicities emerged. As is apparent from the error bars indicating the standard deviation on the determined periodicity, this was most severe for superellipsoids close to $n = 1$. The curve also clearly shows that beyond $n = 1$, the size of the convex structure is related to the periodicity of its scattering pattern by $R\Delta q_{dip} \approx \pi$.

This then indicates that for monodisperse, perfectly aligned (i.e. anisotropic in any direction) superellipsoidal profiles, the size and shape of the scattering object can be determined from the periodicity, the slope and the position of the first dip in the oscillatory scattering pattern. A closer look can now be taken into how several aspects affect the scattering patterns. Aspects that will be discussed first are the effects of polydispersity, the effects of graded interfaces and the effects of packing on the scattering pattern. Since the simulation method as provided here does not allow rotation of the profile, the effect of axial random orientation on the scattering pattern will be discussed in Section 3.5, where 2D scattering pattern of infinite and objects with cylindrical symmetry are simulated.

3.2 The effect of polydispersity on the scattering pattern

The effect of polydispersity on a scattering pattern can be simulated by integrating over a size distribution as opposed to simulating a fixed radius. What becomes important in this case is the scaling of the intensities. Since the numerical Fourier transform takes care of this, all that is needed here, is to make sure that the density of the projected profile is proportional to R. Then, the numerical integration over a probability density function $P(R)$ (defined for real, positive values of R) becomes:

$$I(q) = \int_0^\infty I(q, R)P(R)\mathrm{d}R = \sum_0^\infty I(q, R)P(R)\Delta(R) \tag{3.9}$$

When the density scaling is correctly implemented, the resulting value for $I(q = 0)$ becomes proportional to the profile area^2 (similarly, the amplitude is proportional to the profile area). This implies that the scattering of large objects has much more

impact on the scattering pattern than the scattering of small objects. One could consider this when choosing the step size for the numerical integration (Equation 3.9). Instead of using equidistant sampling points of $P(R)$, a finer mesh could be used for objects of large size and high probability. Another option is to divide $P(R)$ up into sections of equal probability, which would result in a finer division of probable sizes and a rough division of improbable sizes. Any implementation would do, but for large size distributions, sufficient thought should be given to the matter as the number of divisions in a numerical integration should be kept low to keep iteration speed high, but large enough to approximate the underlying integration well enough.

For this example, intended to show the effect of polydispersity on the scattering pattern, an implementation using equidistant sampling points is adequate. For $P(R)$, a lognormal distribution is chosen, because it produces real, positive numbers between 0 and ∞.

$$P(R) = \frac{1}{RS\sqrt{2\pi}} \exp\left(-\frac{(\ln(R) - M)^2}{2S^2}\right) \tag{3.10}$$

The parameters S and M can be calculated from the mean μ and variance σ of the distribution through:

$$\begin{aligned} M &= \ln\left(\frac{\mu^2}{\sqrt{\sigma+\mu^2}}\right) \\ S &= \sqrt{\ln\left(\frac{\sigma}{\mu^2}+1\right)} \end{aligned} \tag{3.11}$$

Figure 3.12 shows four lognormal distributions centered around a mean μ of 100 Å. The curves have not been normalised to aid the visual representation, by leaving out the fraction $\frac{1}{RS\sqrt{2\pi}}$ out of Equation 3.10. The resulting intensity from cylindrical systems with these (relatively mild) polydispersities is shown in Figure 3.13. This figure shows that the difference between $\sigma = 0.1$ and $\sigma = 1$ affects the intensity by reduction of the depth of the oscillations. When larger polydispersities are simulated, a clear dampening of the oscillations is observed at higher angles. The reason for this lies in the difference in periodicities of the intensity curves for the individual contributions to the numerical integration. To illustrate, the contributing intensities in the numerical integration for $\sigma = 10$ are shown in Figure 3.14 without scaling with $P(R)$.

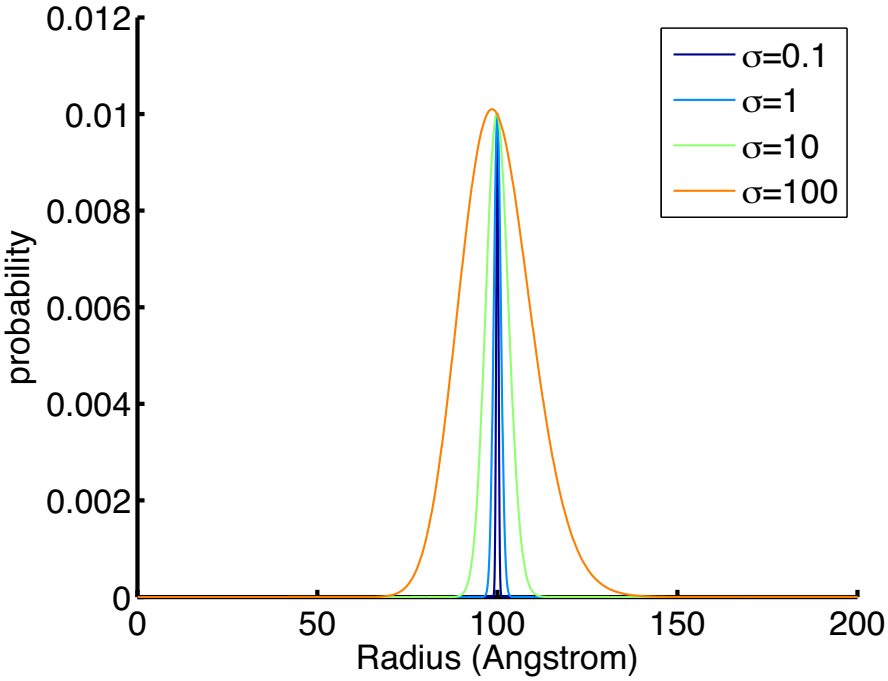

Figure 3.12: *$P(R)$ for variances ranging between $\sigma = 0.1 \ldots 100$, normalised to P(100)=0.1 for visual purposes.*

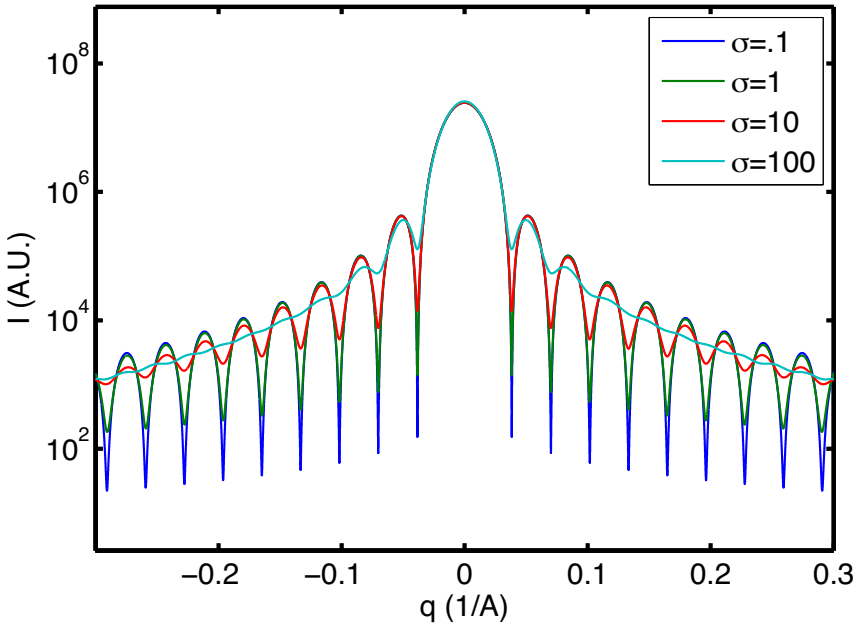

Figure 3.13: *Intensity of cylindrical "samples" with varying polydispersities.*

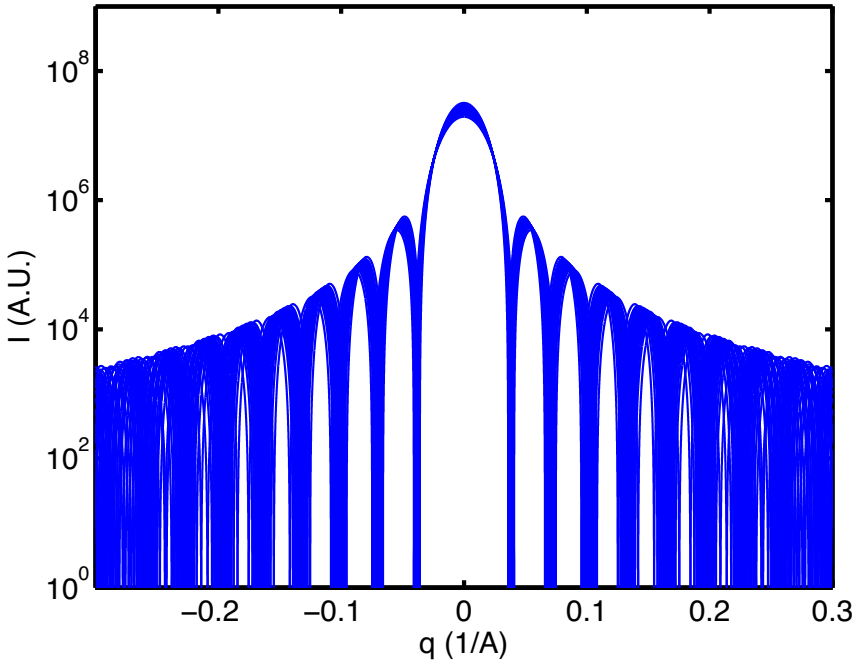

Figure 3.14: *Intensity of the individual contributions to the numerical integration to reach the curve for* $\sigma = 10$ *in Figure 3.13.*

3.3 The effect of graded interfaces

Thus far, it has been assumed that the width of the interface region between the two phases is infinitely small, so that the electron density transition from one phase to the other is infinitely sharp. While for some systems this approximation may be valid (such as solid state systems with a large electron density contrast between the two phases, such as voids in metals), in some cases this approximation may need to be abandoned. Examples of this may be found in polymers that can take up part of the solvent in an interface region. Since it is prudent to understand and perhaps recognise the effects of this on the scattering pattern, a short example may be in order.

The effect of a finite width of the electron density transition region (graded interfaces) has been hinted at in paragraph 3.1.2 when the diamond-like shape was discussed. It has been described in detail in literature by (amongst others) Koberstein et al. [1980]; Ruland [1971]; Vonk [1973]. In the previously outlined 1D scatterer simulation, such an interface region will affect the electron density in a manner identical to the "blurring" effect used in image manipulation. This implies that every sampling point in the electron density is to be affected by the density of the immediate neighbours to that point. An easy way of achieving this is through Fourier transforms:

$$\rho(x)_{\text{smeared}} = \text{FT}^{-1}\left(\text{FT}(\rho(x)) \cdot \text{FT}(G(x))\right) \tag{3.12}$$

Where the $\cdot$ operator is a Hadamard product (also known as entrywise or Schur product) in numerical implementations. $G(x)$ is the real-space probability function with which each sampling point is smeared, and for this example, a Gaussian (Normal) distribution is chosen with a width of $\sigma = 10$ Å. The cylinder profile and the smearing function can be seen in Figure 3.15. The resulting electron density is then shown in Figure 3.16.

The effect of the smearing on the intensity is shown in Figure 3.17 for several smearing widths. As is observed, with increasing smearing width, the steepness of the slope increases as well. What happens, in effect, is that the intensity profile gets multiplied with the Fourier transform of the smearing function. This can be see in Equation 3.12, in which the inverse Fourier transform can be left out if the scattering amplitude is sought:

$$A(q) = \text{FT}(\rho(x)) \cdot \text{FT}(G(x)) \tag{3.13}$$

Similarly, the intensity is the absolute square of this product:

$$I(q) = \mid \text{FT}(\rho(x)) \cdot \text{FT}(G(x)) \mid^2 = \mid \text{FT}(\rho(x)) \mid^2 \cdot \mid \text{FT}(G(x)) \mid^2 \tag{3.14}$$

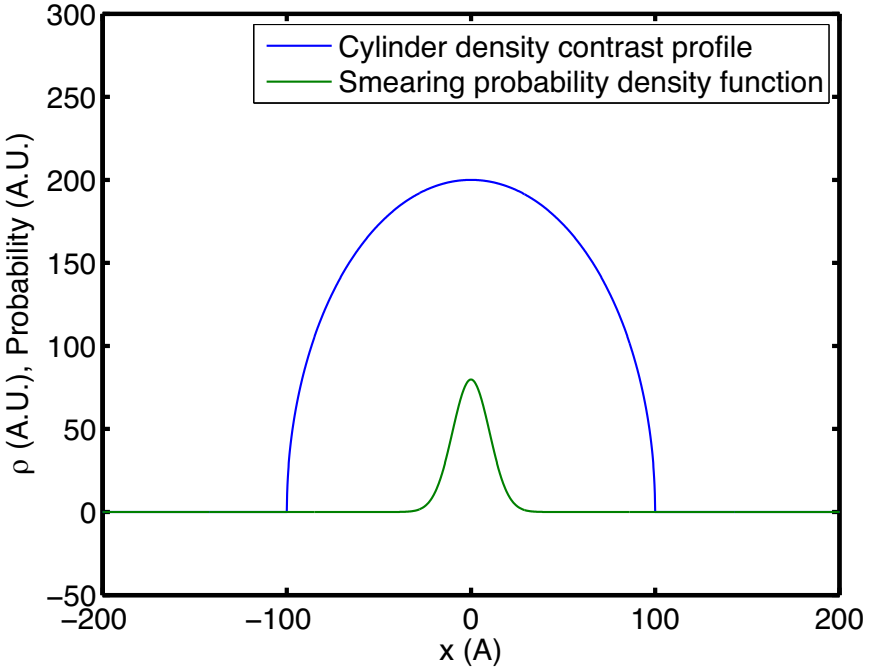

Figure 3.15: *The original cylinder density profile and the smearing profile*

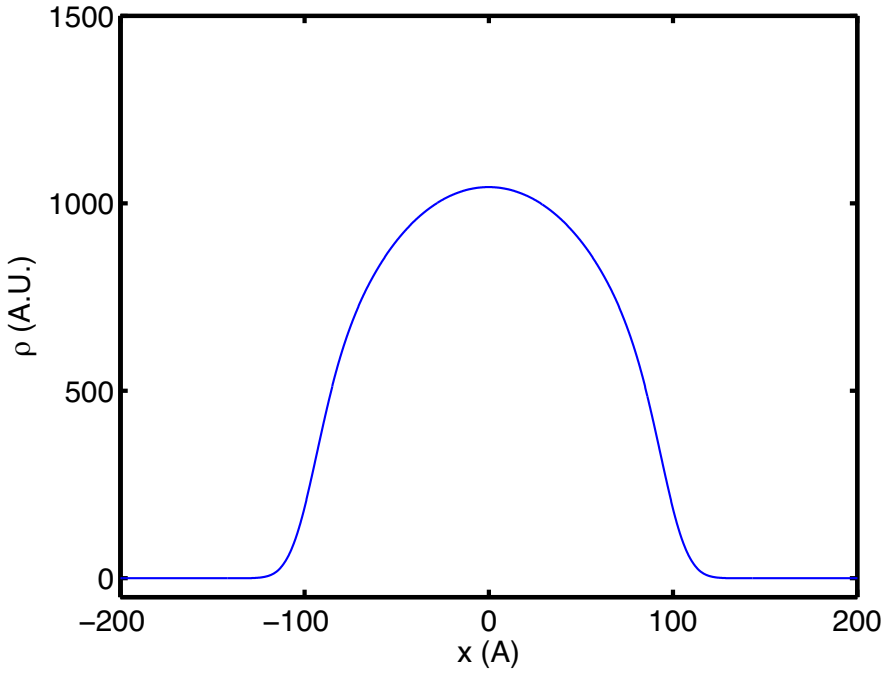

Figure 3.16: *The smeared electron density*

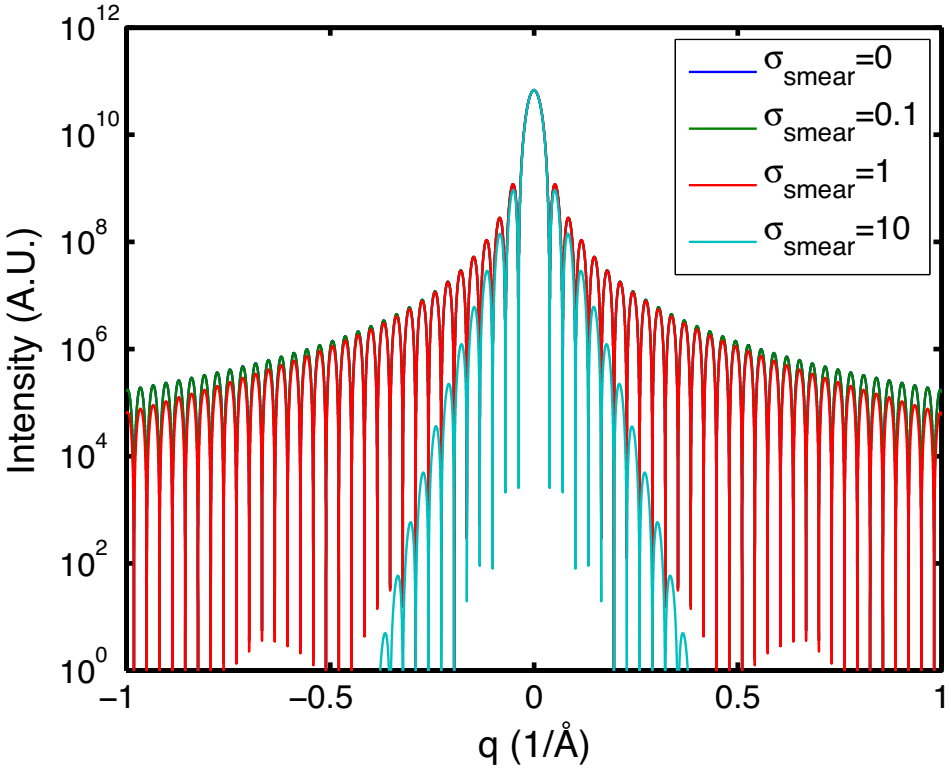

Figure 3.17: *The intensity resulting from cylindrical profiles smeared with gaussian profiles with widths of* $\sigma = 0, 0.1, 1, 10$. *The scattering pattern for* $\sigma = 0$ *is overlapped by that of* $\sigma = 0.1$.

Thus, the same intensity profile of the smeared function can be obtained by multiplying (using the Hadamard product) the intensity for a perfect scatterer with the Fourier transform of the smearing function. The Fourier transform of our Gaussian smearing function is another Gaussian smearing function, with an inverted smearing width in Fourier space. Thus, identical results for $\sigma = 0.1, 1, 10$, shown in Figure 3.16, can be obtained by multiplictation of the intensity for $\sigma = 0$ with a Gaussian probability density function (PDF) with widths of $\sigma = \frac{1}{0.1}, \frac{1}{1}, \frac{1}{10}$ respectively. Other Fourier-space smearing functions have been reported by others [Koberstein et al., 1980; Ruland, 1971; Vonk, 1973].

3.4 Packed structures and the effect of detector smearing

Since only 1D packing can be achieved using the simulation methods described so far, we shall limit ourselves here to examples containing 1D periodicities. These packed structures are also discussed in Chapter 5 in this thesis, where they are applied to interpret the scattering from bent filaments.

The implementation of periodicity in the structure can be done in two ways, either through replication of the profile in real space, or through multiplication in Fourier space. The first method is very straightforward; a single profile is replicated (copied) a number of times before the scattering of the total structure is computed through Fourier transformation. The second method can be beneficial in terms of computation speed, however, and is more elegant in its implementation. This second method works similarly to the method described in the previous section (Section 3.3). The density of a single profile is convoluted (operator $*$) with a periodic function $s(x)$ which is zero everywhere except at the centres of replication, where it is (for example) 1:

$$\rho(x)_{packed} = \rho(x) * s(x) = \mathrm{FT}^{-1}(\mathrm{FT}(\rho(x)) \cdot \mathrm{FT}(s(x))) \tag{3.15}$$

The procedure is shown in Figure 3.18. As before, the inverse Fourier transform can be omitted if amplitudes or intensities are sought after:

$$I(q) = \mid \mathrm{FT}(\rho(x)) \cdot \mathrm{FT}(s(x)) \mid^2 = \mid \mathrm{FT}(\rho(x)) \mid^2 \cdot \mid \mathrm{FT}(s(x)) \mid^2 \tag{3.16}$$

In other literature, the Fourier transform of the elementary shape is often referred to as the "form factor", and the Fourier transform of the position function heralds as the structure factor or lattice factor.

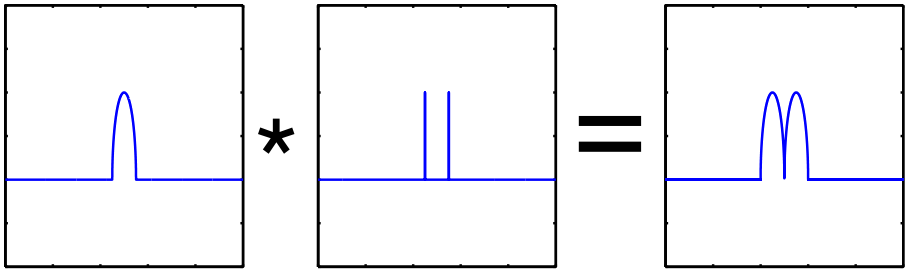

Figure 3.18: *Convolution process of the shape density with a structure density.*

The Fourier transform of a periodic lattice is another periodic lattice with a periodicity proportional to the inverse of the periodicity in real space. In other words, a lattice with a large periodicity in real space will have a small periodicity in Fourier space and vice versa. To illustrate this effect before moving onwards, consider Figure 3.19. Here, the cylindrical profile with a radius of 100 Å has been replicated 10 times, and fills the entire "box" in real space. The resulting scattered intensity consists of infinitely sharp peaks spaced $\Delta q = \frac{2\pi}{200}$ apart [¶]. The intensity decay visible in the simulated scattered intensity originates from the "form factor" intensity, which is an oscillatory function decaying proportional to $I \propto q^{-3}$ as shown in Figure 3.3. The "lattice factor" is then a periodic arrangement of infinitely sharp, equal height "spikes", which is multiplied with the "form factor" intensity in Fourier-space.

Changing the periodicity to double that of the previous example, results in a shift in periodicity to $\Delta q = \frac{2\pi}{400}$ (Figure 3.19). While in this second example the intensity decay power is still proportional to q^{-3}, the analyst of the scattering patterns should be very aware here of the possibility for moiré-like effects occurring, as there are two periodicities which are close to one another. One example of this is shown in Figure 3.19. Now the periodicity of the spikes of the lattice factor no longer coincides with the periodicity of the cylinder form factor, and thus the spikes end up on different positions of the individual oscillations of the form factor. This leads to different intensities at the spike positions. With periodic systems, therefore, analysis of the slope of the intensity is no longer a guarantee for the correct determination of the real-space shape[‖].

So far, only systems with virtually infinite periodicities have been simulated. If the

[¶]The peaks are made finitely sharp in the example by implementing a small Fourier-space smearing of $\sigma = 0.0004$ Å, in order to be able to graph the peaks. This Fourier-space smearing can be considered as detector-based smearing due to finite pixel widths, channel sharing or a point-spread function on the detector.

[‖]Other shapes and sructures can be simulated using the EDsel_gui_v2.m matlab program.

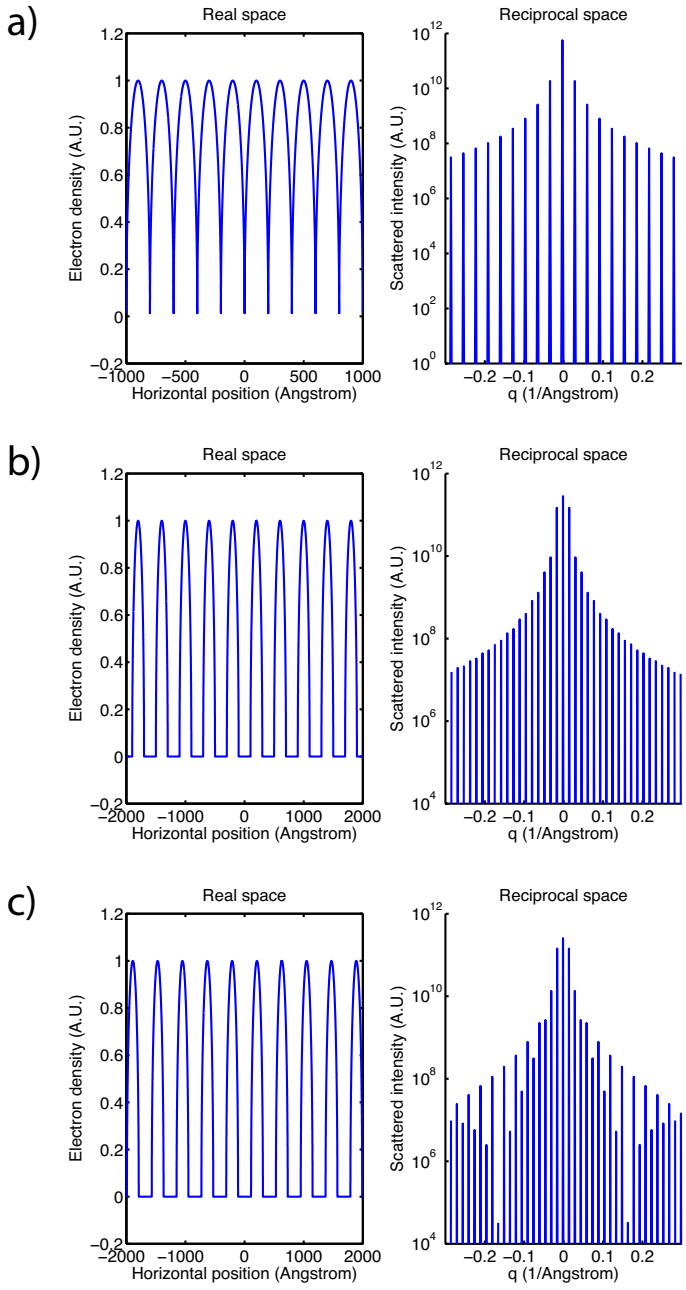

Figure 3.19: *Periodic arrangements of cylindrical profiles with a radius of 100Å spaced (a) 200 Å , (b) 400 Å and (c) 420 Å apart (left), and their scattering intensity (right).*

periodic lattice is finite, which it always is, this will affect the width of the spikes of the lattice factor. These spikes will become broader with a reduced length of the periodic lattice, to end up at a lattice factor of 1 for non-periodic structures. The finite width of the X-Ray beam will also broaden the spikes, as will imperfections in the periodicity. This broadening is sometimes used in the analysis of crystals, where the crystal width (and other imperfections) can be determined from the width of the diffraction peaks. Even the beam width at the sample position can be determined from this broadening.

3.5 Scattering from superellipsoidal objects of revolution

Up to this point, only 1D simulations of projected profiles have been considered and explained in detail. An increase of the dimensionality of the simulations to 2D makes the simulation much more flexible. With 2D simulations, the scattering pattern of aligned 3D structures can be calculated through projection of the electron density (as done in the previous 1D simulation for 2D cross-sections). Alternatively, a 2D slice can be taken through a 3D scattering object, which, when subjected to Fourier transformation, becomes the *projected* scattered amplitude. We will here shortly consider both uses of the 2D simulation, before moving on to the simulation of a 3D structure, and the direct calculation of its (3D) scattering pattern without the need for projections.

3.5.1 Projected objects of revolution

A 3D shape can be projected onto a 2D plane by considering the beam path to have a direction through the 2D projection as shown in Figure 3.20 for a cylinder.

The projected density onto a plane has to be computed of an object of revolution with the revolution axis perpendicular to the beam (and therefore with a circular cross-section parallel to the beam). If we assume our axes to be according to Figure 4.2, then it can be shown that the projected density onto the x, z-plane of our object of revolution, revolved around z is:

$$\rho(x) = 2r_c(z) \sin\left(\arccos\left(\frac{x}{r_c(z)}\right)\right) \tag{3.17}$$

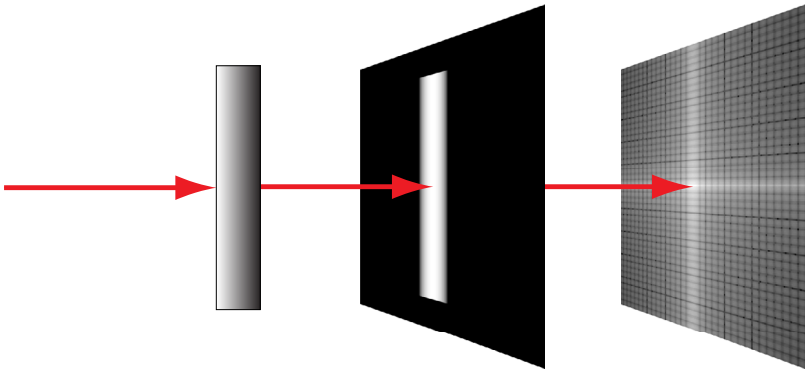

Figure 3.20: *Projection of an isolated 3D object (left) onto a 2D surface perpendicular to the X-ray path (middle) and the scattering intensity computed from the projection (right).*

Where $r_c(z)$ is the radius description of our object at height z in the x, z-plane.

This function then provides us with the ability to turn any arbitrary object with a radius r_c in the x, z-plane into a projected shape of revolution. The function is plotted in Figure 3.21 for $r_c = 1$.

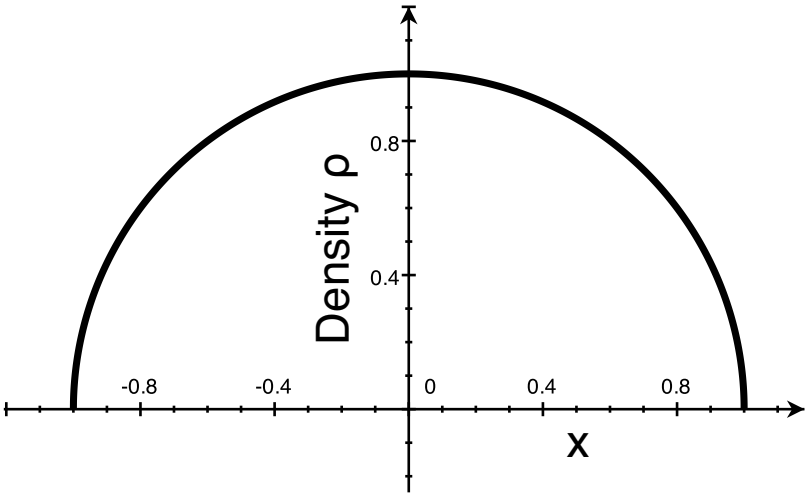

Figure 3.21: *The density on the imageplane 3.17 for $r_c = 1$ at a certain height z.*

3.5.2 Cross-sections

In the 1D simulations, only the intensity from perfectly oriented (i.e. anisotropic in all directions), projected cross-sections could be considered. Using 2D simulations, a slice through the object with the slice plane parallel to the X-ray beam can be used to find the scattering pattern of such objects with arbitrary rotations around the main axis.

Let us consider an infinitely long object with a superellipsoidal cross-section, aligned with the infinitely long axis perpendicular to the X-ray beam, identical to what was done in the 1D simulations. Since the scattering object is infinitely long, the scattering pattern that appears on the 2D detector has only intensity in one direction on the 2D detector, i.e. perfectly perpendicular to the infinitely long axis.

We may take a slice through our object, perpendicular to the infinitely long axis (as shown in Figure 3.22). This density can then be Fourier transformed, resulting in another 2D Fourier-space image. This image is not detected on the detector, but what is observed is the intensity along a line through this Fourier-space image, passing through the centre, parallel to the detection plane (this is known as the Ewald construction with a tangent plane approximation). While rotation of the detector would not allow probing of different orientations in Fourier-space, rotation of the real-space object rotates the Fourier-space with it, allowing for probing of different orientations as shown in Figure 3.23.

Thus, if we have a system of scatterers with non-circular cross-sections, the scattering of the object in different orientations can be simulated by considering the intensity along different directions through the 2D Fourier transform of the cross-sections. A scattering pattern of a superellipsoidal scatterer which exhibits fibre symmetry, i.e. with the long axes aligned in one direction, but with the cross-sections randomly oriented around this "fibre" axis now becomes possible to simulate. Given that the cross-sections have random orientation, we need to integrate through all lines through the centre of the Fourier-space image. Given the symmetry of the Fourier transform, however, only a quarter of the image needs to be analysed (c.f. Figure 3.24). This has as yet not been implemented in this project, but if it were the Bresenham line algorithm may prove to be a key component [Bresenham, 1965].

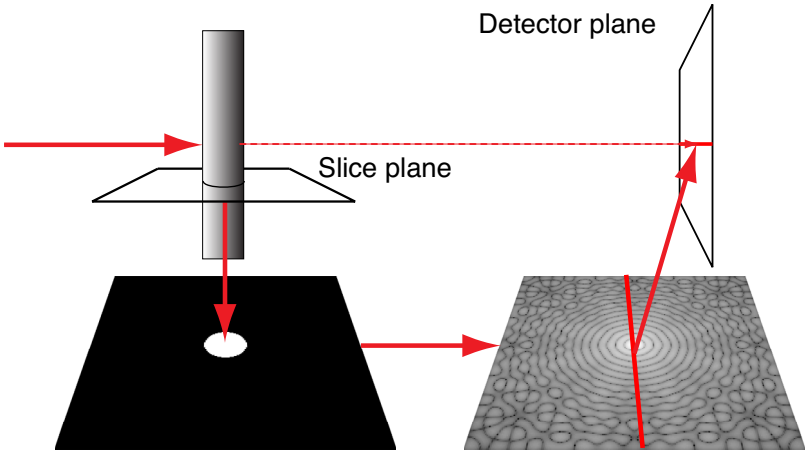

Figure 3.22: *Slice through an isolated 3D object (left) resulting in a 2D cross-section (below, left) parallel to the X-ray path (middle) the scattering of that cross-section (below, right) with the red line indicating the direction of the detector plane and the intensity that will be detected.*

3.6 Scattering from 3D systems

What can be done in 2D, can also be done in 3D. With 3D simulations, we can now simulate an entire nanostructure, and calculate its scattering pattern. If so wished, its scattering pattern can be determined in different orientations by taking planar slices through the centre of the 3D Fourier transform of the shape (these can be planar slices due to the validity of the tangent plane approximation at small angles). The 3D simulation is used in this research as a tool for validation of a scattering pattern analysis function. The 3D simulation as implemented here takes all structural details into account and is, therefore, an ideal tool to test limits of analysis functions. The general outline of the simulation software and some implementation details are provided below.

3.6.1 implementation

A 3D simulation program has been coded, which consists of the functions, ordered in the order of execution, shown in Table 3.1. Two different types of scatterers can be simulated, cylindrical scatterers and ellipsoidal scatterers. As opposed to the 1D and 2D scattering simulations, superellipsoids have not been implemented. The individual steps listed in Table 3.1 to generate a scattering pattern, have been scripted in a matlab program named “Igen_wrapper.m” for cylindrical scatterers

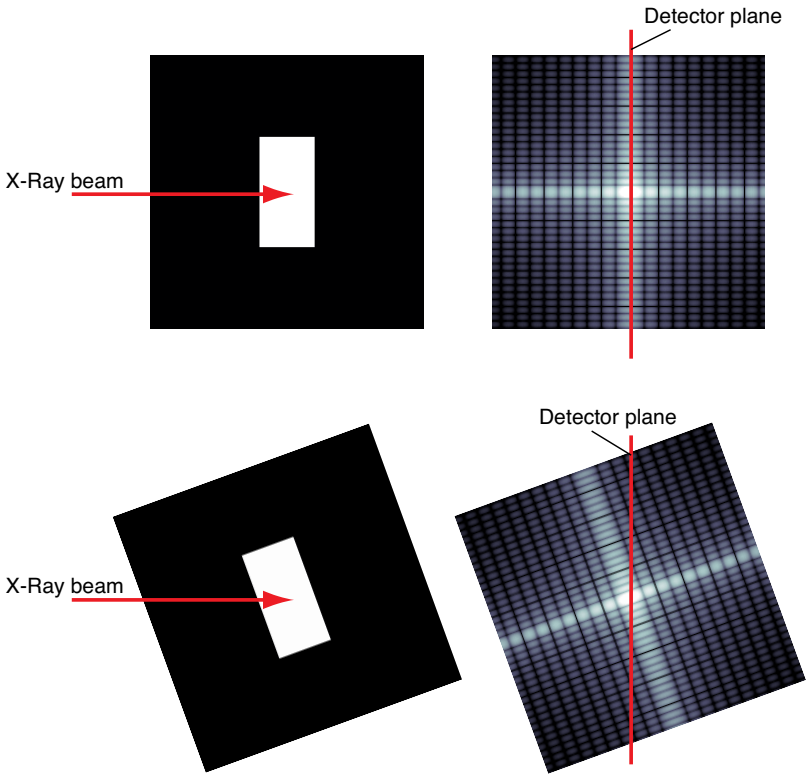

Figure 3.23: *Cross-section through a superellipsoidal object. Rotation of the object in real space brings about an identical rotation of the Fourier-space transform. The slice through Fourier-space indicates the detected intensity. Formally, this is the tangent plane approximation (valid at small angles) of the Ewald-sphere.*

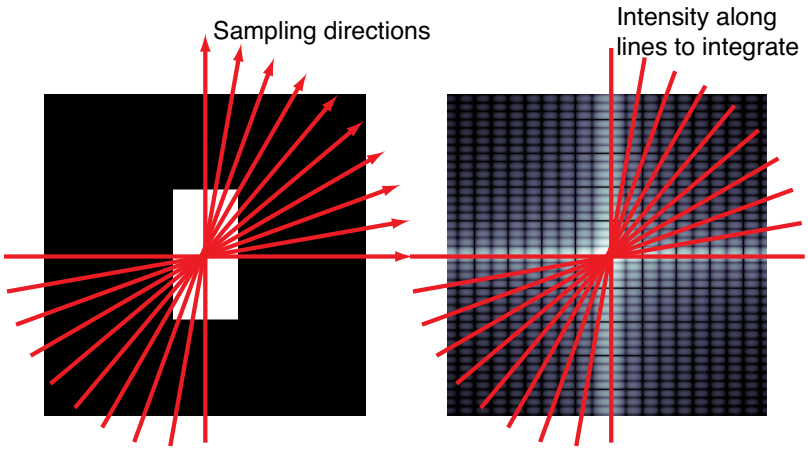

Figure 3.24: *Integration method for determining the scattering over samples with fibre symmetry (i.e. isotropic around a single axis).*

and "Igen_wrapper_ellipsoids.m" for ellipsoidal scatterers. These programs take a structured array as input, which contains the distribution parameters required by the parametrisation routines, a volume fraction (0.01–0.1 recommended), the number of quantisation points (256 recommended), the total size of the simulated box (2000 Å recommended), and the number of repetitions (100 recommended, which averages out to a nice low-noise scattering pattern).

These functions are mostly straightforward, but there are a few details that deserve a little elaboration. The first detail lies in step 1 (the steps are listed in Table 3.1), and concerns periodic boundary conditions. Periodic boundaries are not considered by the Fast Fourier Transform algorithm, and thus the minimum q (and Δq) is related to the length of the box sides. However, scatterers that end abruptly on one side of the box (because they are longer than the box, for example), bring about scattering in the pattern from these "flat sides". In order to remove this scattering, the scatterer should continue on the other side of the box. There is a recursive routine present in the scatterer generation routines, that follow the main axis of the scatterer and determines whether it falls outside the box or not. If so, it generates a copy of the scatterer with its centre placed a box length back, and determines for this scatterer whether it runs outside the box (i.e. it is recursive). What it does not do, however, is check the axes orthogonal to the main scatterer axis for boundary issues. Therefore, there is a small chance that a scatterer may lie very close along a box edge, so that the side of the scatterer is cut off by the box sides. This was considered such a small chance for elongated scatterers, that it is not checked for.

Table 3.1: *Functions making up the 3D scattering simulation software package to simulate scattering from structures of cylindrical or ellipsoidal scatterers.*

Step	cylinder sim. name	ellipsoid sim. name	function description
1.	cylindergeneration_-periodic_-boundary.m	ellipsoidgeneration_-periodic_-boundary.m	parametric description of cylinders or ellipsoids placed in a 3D box according to supplied distribution parameters.
2.	coordtogrid.m	coordtogrid_-ellipsoids.m	Determining for a 3D quantized volume which points lie within and which lie outside a scatterer.
3.	gridstoI.m	gridstoI.m	3D Fourier transform of the grid and subsequent fft shift operation, placing the zero-frequency component in the centre of the Fourier transform.
4.	I3sincsqr.m	I3sincsqr.m	Convolution with a 3D sinc function to improve intensity values, similar to the method described in Equation 3.5.
5.	Iq3DtoI.m	Iq3DtoI.m	Extraction of the slice along the right direction out of the 3D intensity, and permutation of the result to obtain an $nxnx1$ image.
(6.)	CoordinatesToPov.m	CoordinatesToPov_-ellipsoids.m	optional translation of the coordinates to a POV-Ray input file for 3D rendering of the simulated structure.

In addition to that, a hard shell potential has been implemented, which checks overlap of the last generated scatterer with its predecessors. It has been disabled as no effort was spent making it compatible with the recursive loop algorithm described in the previous paragraph, but it may be interesting for future implementations to know how it works. The essence revolves around the computation of the shortest distance between two lines in 3D, and a check whether that distance is shorter or larger than the sum of the local radii of the scatterers (for ellipsoids, with the radius dependent on the position on the axis, this is a little more complex than for cylinders where the radius at each point on its axis is constant). The shortest distance d is computed using the method as given by Weisstein [2007], for lines described by points $\mathbf{x_1}, \mathbf{x_2}$ on the one line and $\mathbf{x_3}, \mathbf{x_4}$ on the second line.

Then:

$$d = \frac{\mid (\mathbf{x_3} - \mathbf{x_1}) \cdot [(\mathbf{x_2} - \mathbf{x_1}) \times (\mathbf{x_4} - \mathbf{x_3})] \mid}{\mid (\mathbf{x_2} - \mathbf{x_1}) \times (\mathbf{x_4} - \mathbf{x_3}) \mid} \tag{3.18}$$

If the shortest distance is larger than the two radii, the scatterers are considered not to touch. However, if it is shorter, a check must be made if the shortest distance actually falls within the lengths of both scatterers, as equation 3.18 does not take the finite length of the scatterers into account.

In the quantisation algorithm, some optimisation has been implemented. Initially, the distance between each 3D grid point in the box and the scatterer axis would be compared with the radius of the scatterer. Since this computation requires a large amount of computing power, the quantisation algorithm places a smaller sub-box around the scatterer. The bounding box in which the scatterer axis is contained, is grown with $\sqrt{3} \times 1.5 \times r_{scatterer}$ to ensure that the endpoints of the cylinder are properly contained by the box. This is shown in Figure 3.25. Subsequently, the distance is computed between each point $X0$ in the grid and the scatterer axis, through:

$$d = \frac{\mid (\mathbf{X2} - \mathbf{X1}) \mid \times \mid (\mathbf{X1} - \mathbf{X0}) \mid}{\mid \mathbf{X2} - \mathbf{X1} \mid} \tag{3.19}$$

For the points that lie within the radius of the scatterer (especially with cylindrical scatterers), one final check is to be done to prevent rounded ends of the cylinders. This is a check at which position t on the scatterer axis (defined by the two points $\mathbf{X1}, \mathbf{X2}$) the shortest distance of the point to the axis is located. If $t > 1$, then the point is outside of the cylinder. t is computed using:

$$t = -\frac{(\mathbf{X1} - \mathbf{X0}) \cdot (\mathbf{X2} - \mathbf{X1})}{\mid \mathbf{X2} - \mathbf{X1} \mid^2} \tag{3.20}$$

Finally, the indexes of the grid points that have been shown to lie within the scatterers are given as output by the program. One may note that it is perhaps possible to come up with a better routine for determining which points in a box lie within a scatterer. Something along the lines of a Bresenham line algorithm could be much more efficient, especially so for scatterers that are not parallel to one of the box axes (when the scatterer main axis lies parallel to one of the major axes of the box, the bounding box is small, requiring the distance calculation for only a small number of points).

Finally, it is highly recommended for users to visually check their results. Half of the human brain is geared towards visual interpretation, so if visual representation is not used, it could be said that one is working with half a brain only. For visualisation of the 3D box with the scatterers inside, a matlab routine exporting the coordinates to POV-Ray format is available. To visualise 3D densities or

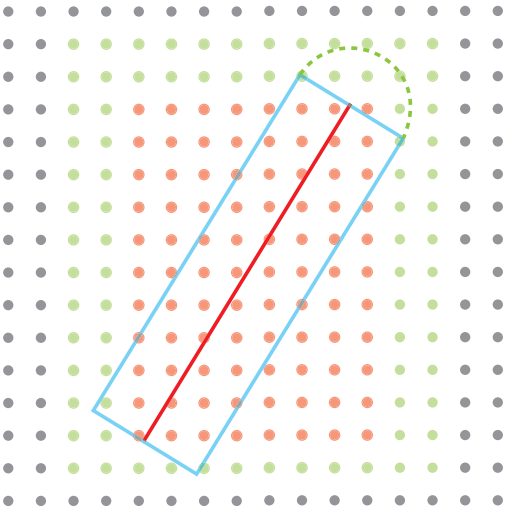

Figure 3.25: *Extra gridpoints (green) required to expand the gridpoints in the bounding box (red dots) defined by the cylinder axis (red line) endpoints, due to the radius of the cylinder (blue box).*

intensities, the program ItoDF3.m can be used, which exports the 3D density in a binary file readable by POV-Ray.

3.6.2 results

A simulation can be run based on the distribution results for Twaron 1000 (based on the analysis results using the newly developed model discussed in the next chapter). The "Distributions" structured array that is used as an input for the "Igen_wrapper_ellipsoids.m" script is shown in Figure 3.26, the number of divisions per side is set to 300 (quantizing the box to $300 \times 300 \times 300$ points), the box length is set to 2000 Å. This generates a structure an example of which is shown in 3.27. The scattering pattern of this structure is shown in Figure 3.28, or more precisely, this is a cut through the 3D Fourier space intensity in a direction parallel to the main axes of the ellipsoids. As is observed, the scattering pattern is relatively noisy. This can be alleviated by running the simulation about 100 times, taking about 20 minutes, resulting in the averaged scattering pattern shown in Figure 3.29.

The interpretation of this scattering pattern and others will be discussed in the next chapter. The software is available on request.

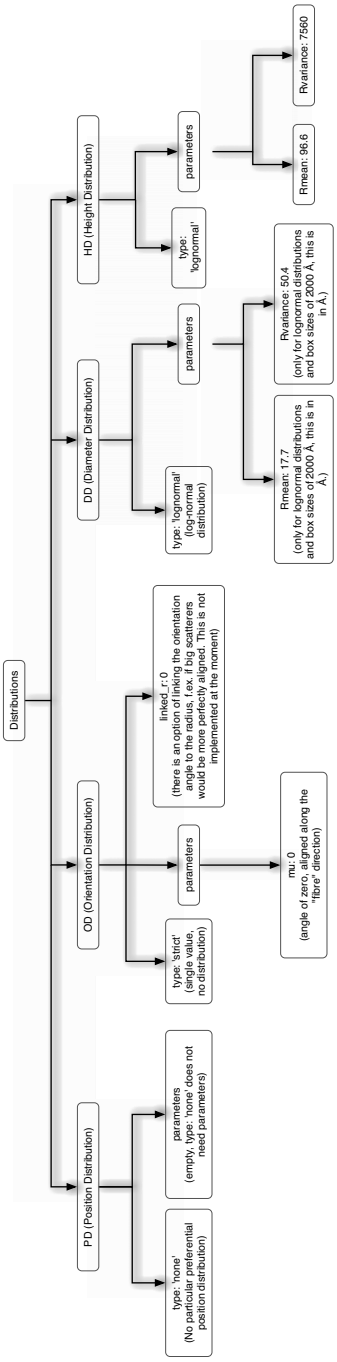

Figure 3.26: *Distribution settings used for simulating the nanostructure of Twaron 1000.*

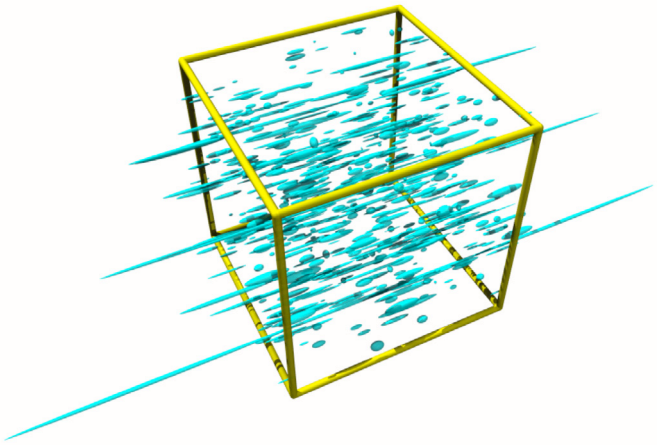

Figure 3.27: *Simulated nanostructure filling the box to a volume fraction of 0.01.*

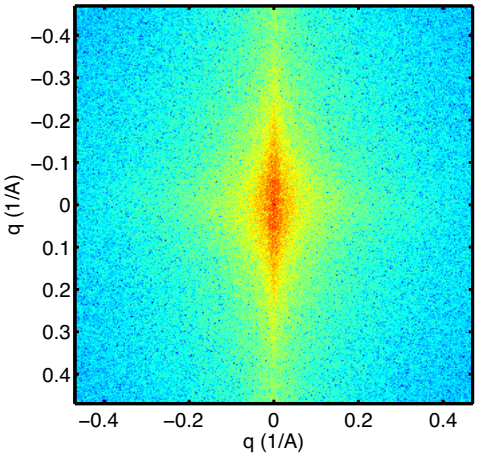

Figure 3.28: *Scattering pattern obtained from a single run of the simulation program. Intensity on a logarithmic scale.*

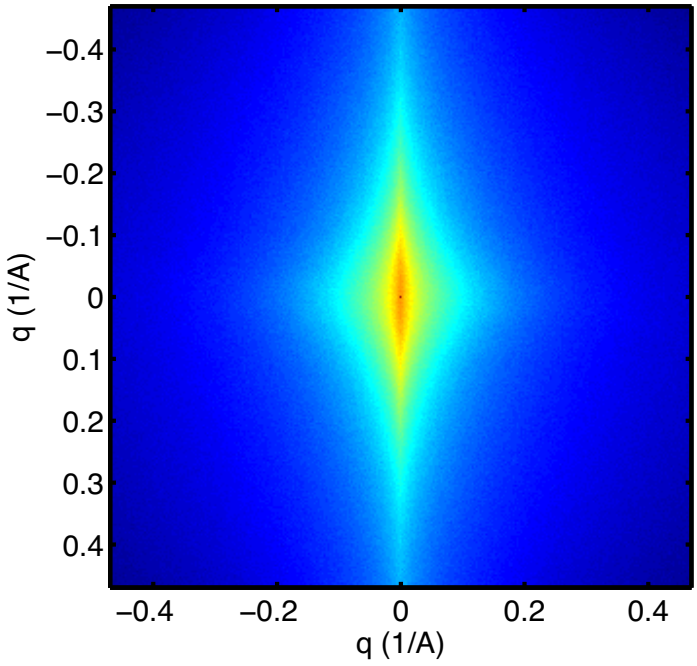

Figure 3.29: *Scattering pattern obtained from a 100 repetitions of the simulation program. Intensity on a logarithmic scale.*

Chapter 4

Analysing the Nanoporous structure of PPTA fibres

4.1 Introduction

The analysis of scattering data originating from these fibres is rather complex. Some complicating factors for this type of sample are the polydispersity, shape and alignment of the scatterers, resulting in a smoothly decaying, anisotropic scattering pattern [Dobb et al., 1979]. Previous analysis methods have focused on limiting the analysis to sections of the scattering patterns to obtain physically relevant parameters [Grubb et al., 1991; Wang et al., 1993].

Whilst much data is left unused when analysing only a small segment of the data, few analysis techniques exist that are capable of analysing the full 2D scattering pattern to use the remaining data without bias. Of note is the 2D analysis method by Helfer et al. [2005], who simulated the scattering pattern from imperfectly aligned monodisperse cylindrical scatterers with finite length, oriented according to a Maier-Saupe orientation distribution. Additionally, Stribeck [2001] uses 2D chord distribution functions (a form of the interface distribution function, adapted to study highly anisotropic materials) to visualize the structural parameters extracted from the scattering patterns in real space.

This chapter focuses on the methodology development for the analysis of the full 2D scattering patterns obtained from aramid fibres. Its merit is tested in relation to the already available methods, as well as to simulations. Lastly, its applicability is shown when applied to a commercial aramid fibre and its precursor.

4.2 Experimental

4.2.1 Sample Preparation

Two samples are considered, one so-called "as-spun" material that has not undergone a tensioned heat treatment procedure, and the commercially available aramid fibre Twaron 1000. The as-spun material can be viewed as a precursor to the commercially available fibre. Both samples consist of a bundle of PPTA filaments, and have been obtained from Teijin Aramid BV, the samples do not contain spin finish. The samples are mounted on rectangular frames of 13 by 18 millimeter in size, similar to the method described by Hermans et al. [1959]. The frames hold an average of about 1000 filaments per mm.

All samples were prepared at minimum one week before the synchrotron SAXS measurements, and they were dried in vacuum before transportation in a box kept dry with silica gel. Upon arrival at the synchrotron facility, the samples were stored in vacuum to prevent the uptake of moisture.

4.2.2 Beamline Details

Synchrotron experiments were performed at the I711 beamline at the MAX-lab synchrotron in Lund, Sweden. The collimation was a square collimation, 0.5 by 0.5 millimeter in size. The wavelength used was 1.235 Å, with a sample-to-detector distance of 1.449 meters. The scattering patterns were recorded using a Marresearch 165 CCD detector, quantized into 2048^2 pixels. Transmission values (where applicable) were determined using a beamstop-mounted detector.

4.2.3 Determination of coefficient of variance using a lab source

In order to determine the coefficient of variance for some model fits, 5 frames of Twaron 1000 and 5 frames of as-spun Twaron were measured for 1 hour on the Risø DTU SAXS instrument. This instrument consists of a rotating anode generator running with a copper anode producing radiation with a wavelength of 1.5418 Å(CuK_α). The beam is collimated to a diameter of 1 mm using pinholes. The sample-to-detector distance was set to 1.45 meters. The detector is a Gabriel-type wire detector, quantized into 1024^2 pixels. Transmission values were determined by detecting fluorescence orthogonal to the beam of an iron foil which can be

placed in front of the beamstop. The coefficients of variance were calculated by comparing the fitting parameters obtained from analysis of the measured data from each frame. The coefficient of variance (CV) is defined as

$$\mathrm{CV} = \frac{\mathrm{Standarddeviation}}{\mathrm{mean}} \tag{4.1}$$

4.2.4 Classical analyses

The literature provides several analysis methods that can be applied for determining the orientation of scatterers in the sample, and for the determination of the average size parameters of the scatterers. We will refer to two main methods that have classically been used to determine the orientation parameters of fibres. These two methods are the invariant-based method, and the "Ruland Streak" method, respectively. For the determination of size parameters, several options are available, namely the Guinier, Debye-Bueche and Porod methods.

Orientation analysis through the Invariant method

An invariant-based orientation parameter determination for samples with fibre symmetry has been developed by Effler and Fellers [1992]. They noted that the invariant for anisotropic scattering patterns has a different meaning than for isotropic samples. For anisotropic samples, the (direction-dependent) invariant Q_ψ, defined as:

$$Q_\psi = \int_0^\infty q^2 I(q,\psi)\mathrm{d}q \tag{4.2}$$

is a measure of the square of the average electron density distribution in the direction ψ, where q is the momentum transfer, defined as $q = \frac{4\pi}{\lambda}\sin(\theta)$ with λ the wavelength of the incident radiation, and 2θ the scattering angle. In the numerical implementation of the integration in this report, no extrapolation to $q = 0$ and $q = \infty$ is performed for this determination. Analysis of the variation of Q_ψ as a function of ψ using equation 4.2 results in the expression of the orientation parameter as $\langle\sin^2\psi\rangle$ or the Hermans orientation parameter F_H through $F_H = 2\langle\sin^2\psi\rangle - 1$:

$$\langle\sin^2\psi\rangle = \frac{F_H + 1}{2} = \frac{\int_0^{\frac{\pi}{2}} Q_\psi \sin^2\psi \mathrm{d}\psi}{\int_0^{\frac{\pi}{2}} Q_\psi \mathrm{d}\psi} \tag{4.3}$$

This equation can be numerically solved using a sufficiently small step size. For a perfectly oriented scatterer, $\langle\sin^2\psi\rangle$ is 1 and for randomly oriented scatterers this is 0.5 (corresponding to an F_H of 1 and 0 respectively).

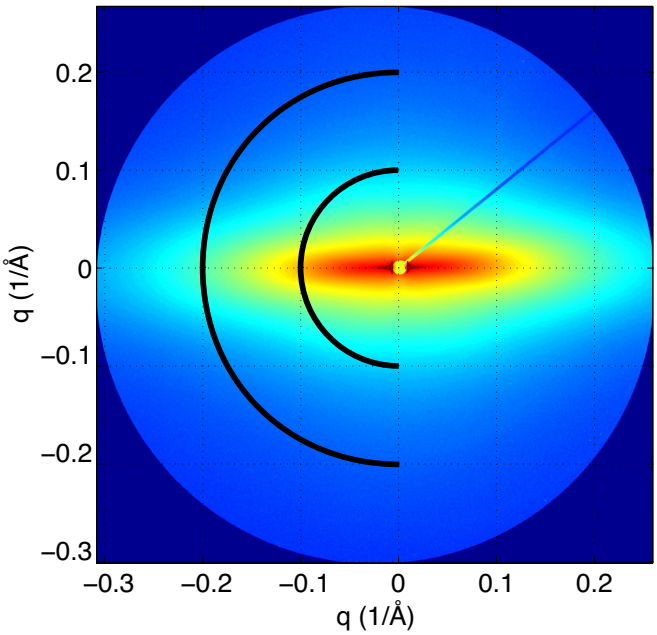

Figure 4.1: *Azimuthal regions for the determination of the integral breadth, overlaid on top of a scattering pattern of Twaron 1000, obtained at MAX-lab. Intensity shown on a logarithmic scale.*

Orientation analysis through the Ruland Streak method

The degree of alignment of scatterers can also be obtained using the so-called Ruland Streak method. This method was proposed by Perret and Ruland [1969]. The method assumes well-oriented scatterers with a high aspect ratio, for example needle-like voids as found in carbon fibres. The main scattering contribution is found along the normal of the main axis of the scatterer. A single scatterer will produce a scattering streak along this normal. A rotation of the main axis of the scatterer in the plane of the detector, will see a similar rotation of the streak. Thus, the distribution G_N of the normals of the scatterers in the detector plane, can be directly measured.

The method consists of determining the integral breadths of an azimuthal region (i.e. a domain at constant q), as shown in Figure 4.1. The integral breadths are defined as:

$$B_{obs}(q) = \frac{\int_{\psi_{max}-\frac{\pi}{2}}^{\psi_{max}+\frac{\pi}{2}} I(q,\psi)\mathrm{d}\psi}{I(q,\psi_{max})} \tag{4.4}$$

And the error of this computation is defined as:

$$\epsilon_b = \sqrt{\sum_{\psi} I(q,\psi)} + \sqrt{I(q,\psi_{max})} \tag{4.5}$$

Where B_{obs} is the observed integral breadth of the azimuthal profile, ψ_{max} is the angle at which the peak maximum is found and $I(q,\psi)$ is the background corrected intensity. Thus, the integral breadths provide a means of quantifying the width of the azimuthal profiles, irrespective of the peak shape. It remains, however, sensitive to noise, which for regions of low intensity can increase the integral breadth.

It is noted by Perret and Ruland [1969] that this observed integral breadth is equal to the breadth of the distribution of the normals of the scatterers, and should thus be independent of q. This is true for infinitely long scatterers. For scatterers with finite length L, there is an additional contribution, present mainly at low q, originating from the length L of the scatterers. This contribution is dependent on q. For a Gaussian orientation distribution of the axes of the scatterers, the observed integral breadth B_{obs} is related to q, L, and the integral breadth of the normals of the scatterers B_ψ by:

$$B_{obs}^2 = B_\psi^2 + \frac{4\pi^2}{L^2 q^2} \tag{4.6}$$

This holds for relatively narrow orientation distributions. For a Lorentzian (Cauchy-like) orientation distribution of the axes, this becomes:

$$B_{obs} = B_\psi + \frac{2\pi}{Lq} \tag{4.7}$$

Both equations are applied when analysing the experimental data, and are fit to the B_{obs} vs. q data. The equation that describes best the observed values of B_{obs} is the most likely candidate in terms of type of orientation distribution [Stribeck, 2007].

The Debye-Bueche correlation length determination

It has been established that approximating methods developed for isotropic systems are also applicable to systems with fibre symmetry [Ruland, 1978]. This

implies that, for example, the Debye-Bueche method for random interfaces can be applied to oriented systems [Debye and Bueche, 1949]. The method is then to be applied to the unprojected data in a certain direction (e.g. perpendicular to the fibre axis), and the results are then only valid for the nanostructure in that particular direction [Ruland, 1978].

The Debye-Bueche scattering function for a system of random interfaces is expressed as [Debye and Bueche, 1949]:

$$I(q) = \frac{I_0}{(1 + q^2 L_c^2)^2} + I_{fl} \tag{4.8}$$

where I_0 is a intensity scaling factor, L_c is the Debye correlation length (a characteristic size parameter related to the mean lengths between interfaces present in the sample) and I_{fl} is a constant, modeling the scattered intensity from electron density fluctuations in the phases according to Ruland [1971].

If there are two distinct, non-interacting distributions of interfaces originating from objects of considerably different sizes (i.e. if the sample contains scatterers with a bimodal size distribution), then the two can be considered to have separate, independent contributions to the scattering intensity. With relevance to our study, these two objects of considerably different sizes could consist of: 1) a structure of fibrils with interfibrillar voids) and 2) a nanoporous structure of (much smaller) voids inside the fibrils. Under this assumption, a "Double Debye" function can be construed:

$$I(q) = \frac{I_{0a}}{(1 + q^2 L_{c1}^2)^2} + \frac{I_{0b}}{(1 + q^2 L_{c2}^2)^2} + I_{fl} \tag{4.9}$$

The Porod length determination

The Porod relationship applicable for scattering from smooth interfaces, is expressed as:

$$I(q) = \frac{K_p}{q^4} + I_{fl} \tag{4.10}$$

for sufficiently large q. Here too, the fluctuation term I_{fl} has been added [Ruland, 1971].

A size parameter L_p can be determined from a Porod fit applied to data on an arbitrary intensity scale, through:

$$L_p = \frac{\pi \int_0^\infty I(q) q \mathrm{d}q}{Q} \tag{4.11}$$

To solve this equation, the first moment (numerator) and the invariant (denominator) have to be determined. The invariant is defined as [Glatter and Kratky, 1982]:

$$Q = \int_0^\infty q^2 I(q) \mathrm{d}q \tag{4.12}$$

and can be obtained through solving the invariant for the intensity described by both the Debye function (equation 4.8, without fluctuation terms as indicated in [Ruland, 1990]), and the Porod function (equation 4.10), bounded by the crossover limit q_{co}:

$$\begin{array}{rcl} \int_0^{q_{co}} \frac{I_0 q^2}{(1+q^2 L_c^2)^2} \mathrm{d}q = & \frac{I_0}{2L_c^2} \left(\arctan(L_c q) - \frac{L_c q}{L_c^2 q^2 + 1} \right) |_0^{q_{co}} \\ = & \frac{I_0}{2L_c^2} \left(\arctan(L_c q_{co}) - \frac{L_c q_{co}}{L_c^2 q_{co}^2 + 1} \right) \end{array} \tag{4.13}$$

and

$$\int_{q_{co}}^{inf} \frac{q^2 K_p}{q^4} \mathrm{d}q = \frac{K_p}{q_{co}} \tag{4.14}$$

The total invariant Q then is:

$$Q = \frac{I_0}{2L_c^2} \left(\arctan(L_c q_{co}) - \frac{L_c q_{co}}{L_c^2 q_{co}^2 + 1} \right) + \frac{K_p}{q_{co}} \tag{4.15}$$

The numerator is derived in a similar manner as Q:

$$\begin{array}{rcl} \pi \int_0^\infty I(q) q \mathrm{d}q = & \pi \left(\int_0^{q_{co}} \frac{q L_c}{(1+q^2 L_c^2)^2} \mathrm{d}q + \int_{q_{co}}^\infty \frac{q K_p}{q^4} \mathrm{d}q \right) \\ = & \pi \left(-\frac{1}{2(q_{co}^2 L_c^3 + L_c)} + \frac{1}{2L_c} + \frac{K_p}{2q_{co}^2} \right) \end{array} \tag{4.16}$$

4.2.5 Model set-up

A new analysis model is built up around a system of well-oriented ellipsoidal scatterers, independently polydisperse in both the long and short axes of the ellipsoids. This is a modification of the method of Helfer *et al.* [Helfer et al., 2005], who modelled a system of oriented, monodisperse, cylindrically shaped scatterers. The full description for the scattering intensity of a system of polydisperse oriented scatterers is:

$$\begin{array}{rcl} I(\mathbf{q}) = I(q,\psi) = & C_1 \int_0^\infty \int_0^\infty V(R_1,R_2)^2 \int_0^{2\pi} \int_0^{\frac{\pi}{2}} \\ & F^2(q, R1, R2, \phi, \theta, \psi) h(\theta) \sin(\theta) \\ & \mathrm{d}\theta \mathrm{d}\phi f(R_1) g(R_2) \mathrm{d}R_1 \mathrm{d}R_2 \end{array} \tag{4.17}$$

where $\mathbf{q}$ is the scattering vector with magnitude q and ψ is the angle on the detector (Figure 4.2). θ is the angle between the fibre axis and the long axis of the ellipsoid, and ϕ is the angle between the projection of the long axis on the $x-y$-plane and the x axis. The diffraction geometry is graphically displayed in Figure 4.2. F is the form factor of the scatterer and C_1 is a scaling factor. The distribution $h(\theta)$ is the orientation distribution of the scatterers with respect to the fibre axis, and $f(R_1)$ and $g(R_2)$ are the size distributions for the ellipsoidal scatterers, one describing the short axis (R_1), and the other describing the long axis of the ellipsoid (R_2). The size distributions $f(R_1)$ and $g(R_2)$ are expressed using the log-normal probability density function $P(R)$, commonly used to describe particle size distributions, and defined as [Weisstein, 2005]:

$$P(R) = \frac{1}{RS\sqrt{2\pi}} \exp\left(-\frac{\left(\ln(R) - M\right)^2}{2S^2}\right) \tag{4.18}$$

The parameters S and M are related to the mean μ and variance σ of the distribution through:

$$\begin{aligned} M &= \ln\left(\frac{\mu^2}{\sqrt{\sigma+\mu^2}}\right) \\ S &= \sqrt{\ln\left(\frac{\sigma}{\mu^2}+1\right)} \end{aligned} \tag{4.19}$$

For numerical purposes, it is more convenient to use the orientation distribution function $\tilde{h}(\theta)$, defined as:

$$\tilde{h}(\theta) = 2\pi \sin(\theta) h(\theta) \tag{4.20}$$

In this report, we initially assume a perfect orientation of the scatterers, and therefore the description of the 2D scattering intensity simplifies to:

$$\begin{aligned} I(\mathbf{q}) = I(q,\psi) = \; & C_2 \textstyle\int_0^\infty \int_0^\infty V(R_1,R_2)^2 \\ & F^2(q, R1, R2, \phi, \theta, \psi) f(R_1) g(R_2) \mathrm{d}R_1 \mathrm{d}R_2 \end{aligned} \tag{4.21}$$

where C_2 is a scaling factor.

The form factor of an ellipsoidal scatterer is obtained as a modification of the form factor of a sphere. This can be achieved by replacing the sphere radius R in the Rayleigh scattering function by R_{ell}, defined as [Pedersen, 1997]:

$$R_{ell} = \sqrt{\left(R_1^2 \sin^2\gamma + 4R_2^2 \cos^2\gamma\right)} \tag{4.22}$$

where γ is the angle between $\mathbf{q}$ and the main ellipsoid axis. We then obtain for the form factor of our ellipsoidal scatterer:

$$F(q, R_1, R_2) = 3\frac{\sin(qR_{ell}) - qR_{ell}\cos(qR_{ell})}{(qR_{ell})^3} \tag{4.23}$$

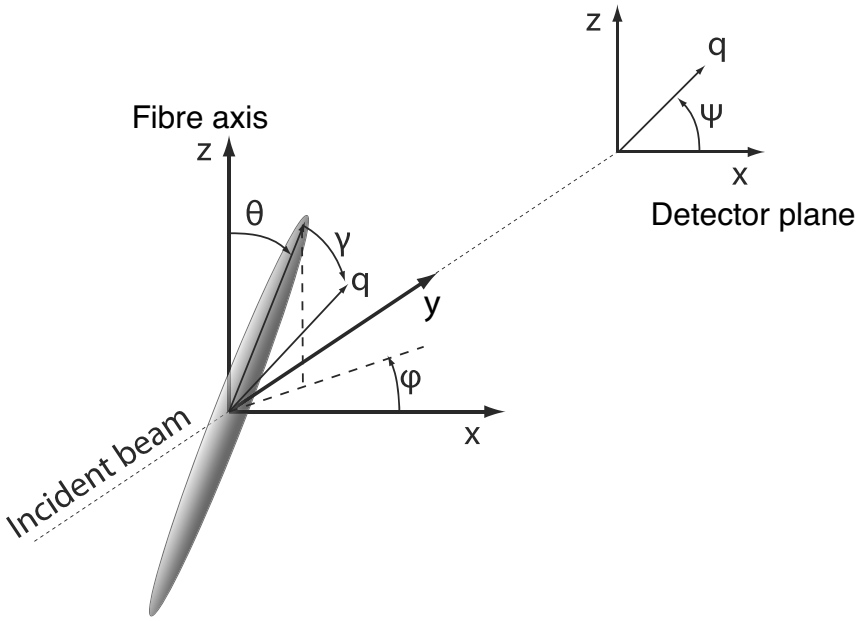

Figure 4.2: *Diffraction geometry used in the model description.*

Note that a structure factor is not included in the scattering function (equation 4.21). This has been done since the ellipsoidal void structure is assumed to be non-interacting and the individual scatterers are able to intersect. One could expect some typical distance between voids imposed by for example crystal sizes or fibrillar sizes, but the observed small-angle scattering gives no indication of such characteristics. This implies that no volume is excluded, and no structure is imposed at higher scatterer concentrations. A structure factor is therefore not considered.

Adaptations to this model which will be discussed below include an implementation of an orientation distribution of the ellipsoids, and the addition of large size scatterers to the log-normal distributions to approximate a bimodal distribution. The orientation distribution has been implemented as a rotational smearing of the modeled scattering pattern (equation 4.21) in ψ. This amounts to a rotation of the ellipsoids only in the XZ plane (i.e. assuming $\phi = 0$). This has been done to speed up the calculation of the rotationally smeared intensity (as an additional numerical integration over ϕ would significantly increase the computational time), and yields results which approximate the orientation distribution in θ of the ellipsoidal scatterers. This approximation is valid *only* for small widths of the orientation distribution. The orientation distribution implemented here is

a Von-Mises distribution function [Weisstein, 2009], modified for high values of κ by P. Malchev at Teijin Aramid. We use for the probability density distribution function in degrees:

$$P = \begin{cases} \frac{\kappa}{2\pi} \frac{\exp\left(\kappa \cos(x\frac{2\pi}{360})\right)}{2\pi \mathrm{J}(0,\kappa)} & \text{if } \kappa < 100 \\ \frac{\kappa}{2\pi} \exp\left(\kappa \cos\left(x\frac{2\pi}{360}\right)\right) & \text{if } \kappa > 100 \end{cases} \tag{4.24}$$

where J is the Bessel function of the first kind, and κ is an inverse measure of the width of the orientation distribution.

The second adaptation is the addition of large scatterers. For some materials that will be described below, a significant amount of scattering at low q reduces the fitting capability of the model. This extra scattering at low q is taken into account by the addition of a large, slightly polydisperse (to reduce oscillatory behaviour) ellipsoid to the model. Such large scatterers could be related to a more pronounced fibrillar structure present in these fibres. This is implemented by adding to the intensity obtained from the model (equation 4.21), the intensity obtained from equation 4.21 only now with distributions for the short axis radius R_{L1} and long axis radius R_{L2} for large scatterers, i.e.:

$$I_{\text{adapted}}(\mathbf{q}) = I(\mathbf{q}, f(R_1), g(R_2)) + C_3 I(\mathbf{q}, f(R_{L1}), g(R_{L2})) \tag{4.25}$$

where C_3 is the scaling factor for the intensity from the large scatterers. The distributions for the large scatterers are linked through the aspect ratio α through:

$$g(R_{L2}) = \alpha f(R_{L1}) \tag{4.26}$$

and the widths of the distributions are fixed to small values (sufficiently large to dampen oscillatory behaviour), so that only the short axis radius R_{L1}, aspect ratio α and scaling factor C_3 are added as fitting parameters.

The model intensity values are calculated on a grid spanning 90 degrees in ψ from the x-axis (Figure 4.2), and the q-range that has been selected to be fit. Due to the orientation distribution implementation, the 90 degrees in ψ are divided into 90 sections, and the q-range is divided into 20 sections. This number has been shown to be more than sufficient to accurately model the intensity decay of the data. For each pair of thus gridded q and ψ, the intensity on the grid is computed. The model intensity for each q and ψ value in the data is then interpolated from the grid using a 2D linear interpolation method available in Matlab.

The fitting procedure is carried out using a prototype open-source SAXS analysis package named "SAXSGUI", developed by dr. K. Joensen of JJ X-Ray Systems A/S in collaboration with Rigaku and several individual contributors. The data is

linearly binned using bins containing 4x4 image pixels. The q-range fit is $0.025 - 0.25$ Å^{-1}, and the ψ range extends 90 degrees to either side of the main axis of the scattered streak. The minimization function is a least squares residual function:

$$\epsilon^2 = \sqrt{\frac{\sum_{i=1}^{N} \left(I_{\text{model}} - I_{\text{measurement}}\right)^2}{N}} - n_{\text{param}} \tag{4.27}$$

where i is the datapoint index, and N is the total number of datapoints in the fit, and n_{param} is the number of fitting parameters.

4.2.6 Simulation set-up

In order to verify the applicability of some of the analysis methods, scattering patterns have been numerically simulated. In order to achieve this, a three-dimensional box is filled with perfectly aligned non-interacting ellipsoids, polydisperse in both the short radius as well as the long radius using separate log-normal distributions *. The positioning of the ellipsoids within the box is purely random. In order to suppress edge effects (from truncated ellipsoids) during the Fourier transform procedure, the ellipsoids that cross the box boundaries are subject to periodic boundary conditions. The box is divided into 300^3 voxels, Fourier transformed, and convoluted with a sinc function (Fourier transform of a voxel) similar to the method described by Schmidt-Rohr [2007].

The first row of parameters listed in Table 4.1 is used for initial tests. The other listed values offer values for aspect ratio tests that are used to determine the effects of aspect ratio on the orientation distribution analysis methods. Each simulated scattering pattern consists of the average of 100 invocations of the simulation (i.e. the structure is regenerated and its scattering pattern computed 100 times).

The obtained simulated scattering pattern (shown in Figure 4.4) can now be used to test the applicability of some of the models.

*This simulation will be described in more detail in a forthcoming article

Table 4.1: *Simulation parameters.*

$f(R_1)\ \mu$	$f(R_1)\ \sigma$	$g(R_2)\ \mu$	$g(R_2)\ \sigma$	Volume fraction	approx. aspect ratio
17.7	50.4	96.6	7560	0.01	5.45
20	50	2	5	5e-4	0.1
20	50	4	10	1e-3	0.2
20	50	10	25	2.5e-3	0.5
20	50	20	50	5e-3	1
20	50	40	100	0.01	2
20	50	100	250	0.025	5
20	50	200	500	0.05	10
20	50	2000	5000	0.1	100

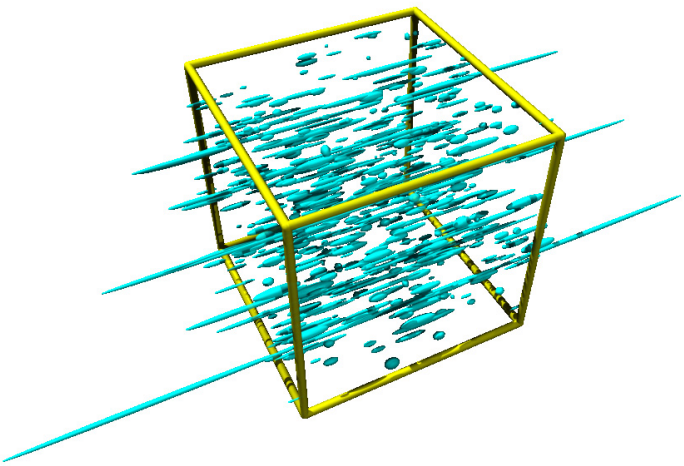

Figure 4.3: *An example of a simulated volume filled with ellipsoids, with the parameters* $f(R_1)\ \mu = 17.7$, $f(R_1)\ \sigma = 50.4$, $g(R_2)\ \mu = 96.6$, $g(R_2)\ \sigma = 7560$, *so that the volume fraction is 1%.*

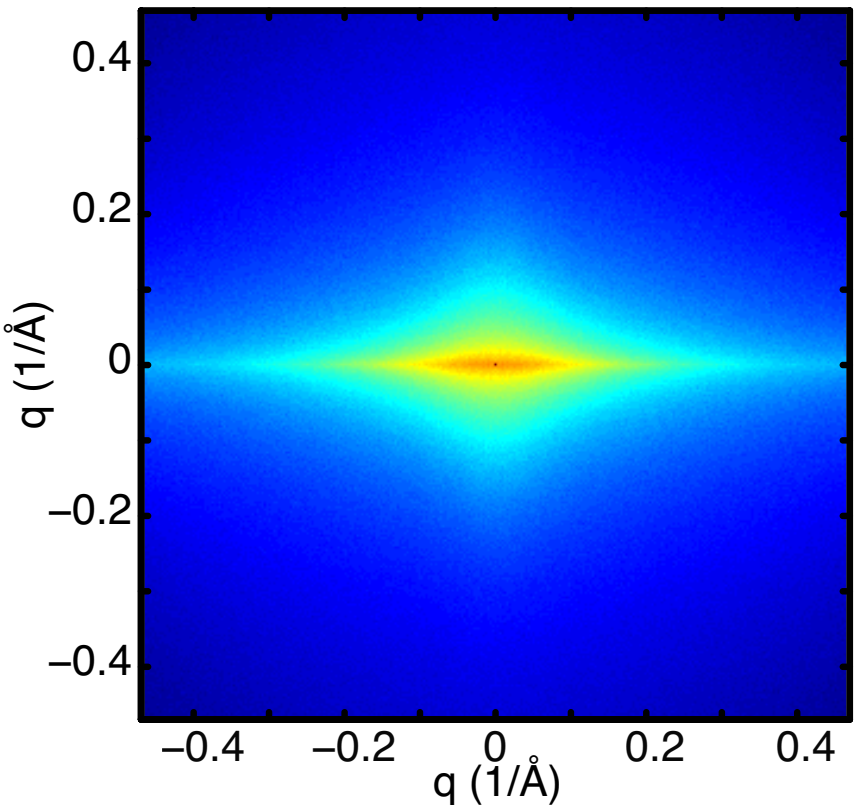

Figure 4.4: *Simulated scattering pattern obtained from a system of ellipsoids, with the parameters* $f(R_1)$ $\mu = 17.7$, $f(R_1)$ $\sigma = 50.4$, $g(R_2)$ $\mu = 96.6$, $g(R_2)$ $\sigma = 7560$, *and a volume fraction of 1%. Intensity shown on a logarithmic scale.*

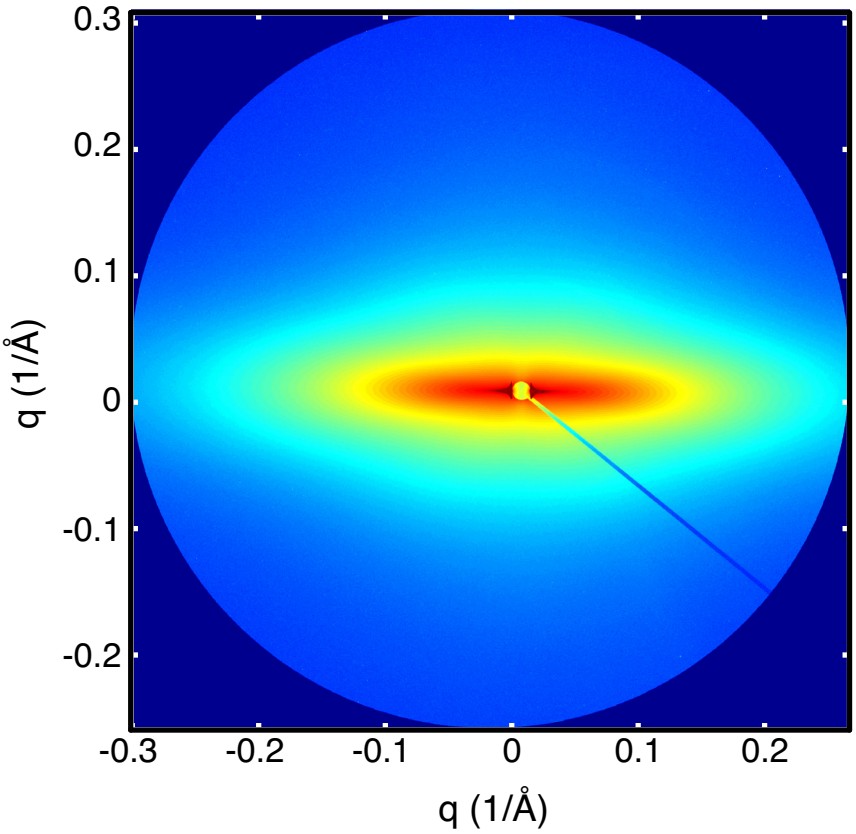

Figure 4.5: *A scattering pattern obtained from a 30-minute exposure at MAX-lab of a bundle of Twaron 1000 filaments mounted on a frame. Intensity shown on a logarithmic scale.*

4.3 Results and discussion

4.3.1 Classical and new data analysis models applied to PPTA

Example measurement

A 30-minute measurement of Twaron 1000 was chosen as an example measurement, to which the applicability of the methods could be tested. The 2D scattering pattern of this sample is shown in Figure 4.5.

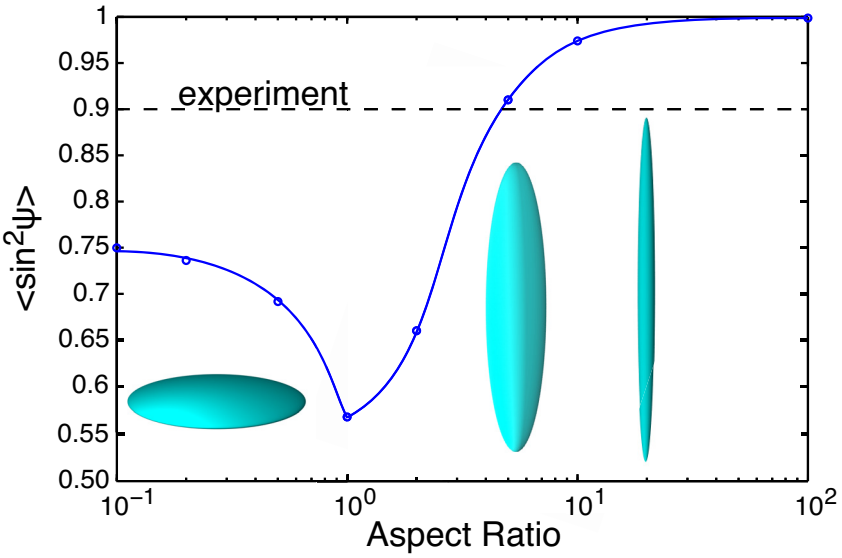

Figure 4.6: $\langle \sin^2 \psi \rangle$ *determined via the Effler invariant method with parameters given in Table 4.1, versus the mean aspect ratio for scattering patterns obtained from simulations of perfectly oriented, polydisperse ellipsoidal scatterers. The dashed line indicates the experimentally found value for Twaron 1000, the solid line is a Bezier curve drawn to guide the eye.*

Classical analysis models

Effler Invariant method Analysis of the measured scattering pattern using the Effler Invariant method in the q-range of $q = 0.03 - 0.2$ Å^{-1}, results in an orientation parameter value of $\langle \sin^2 \psi \rangle = 0.899(3)$. This value is the average over all four quadrants. The corresponding Hermans orientation factor F_H is 0.80.

An analysis of the simulated data shown in Figure 4.4 of polydisperse, perfectly aligned ellipsoids with a relatively low aspect ratio results in an orientation parameter value of $\langle \sin^2 \psi \rangle = 0.881(9)$. This result for a perfectly aligned system shows that the Effler Invariant method is sensitive to the aspect ratio of the scatterers, which affects the intensity in the directions off-normal to the scatterers. This effect may be investigated more closely, i.e. by plotting the $\langle \sin^2 \psi \rangle$ value as a function of mean aspect ratio for several simulations of perfectly oriented, polydisperse ellipsoidal scatterers, resulting in the diagram as shown in Figure 4.6. The point at an aspect ratio of 1 indicates a value of $\langle \sin^2 \psi \rangle = 0.56$. Note that separate size distributions were used for the length and the width, and that therefore the aspect ratio in Figure 4.6 is the average of all scatterers.

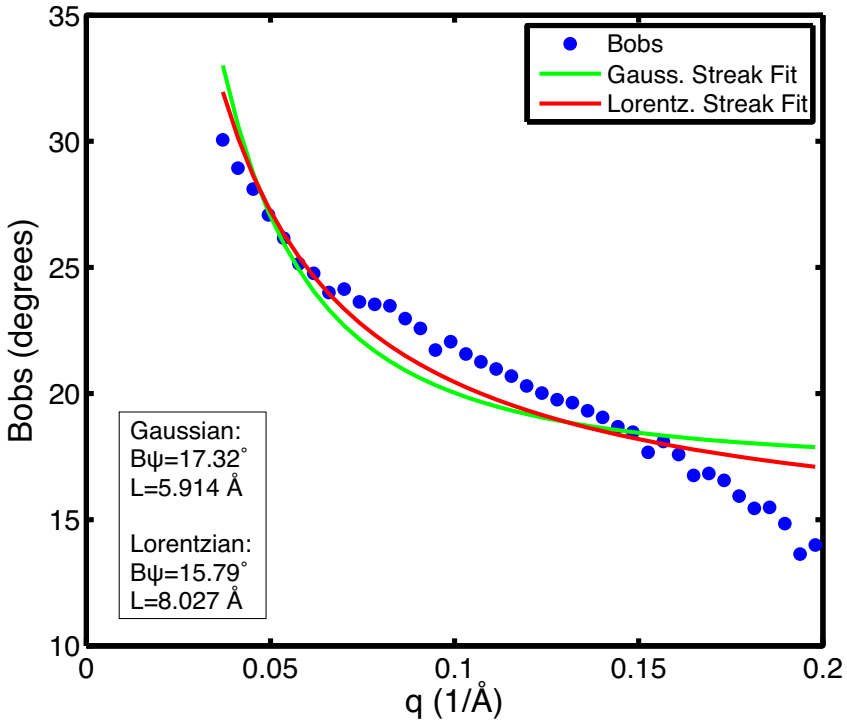

Figure 4.7: *Streak fits to the scattering pattern obtained (at MAX-lab) from a bundle of Twaron 1000 filaments.*

From this figure, and given the experimental value of $\langle \sin^2 \psi \rangle = 0.899$, we find that the mean aspect ratio of the scatterers in the sample must lie above ≈ 5. If the sample were to contain scatterers with much larger aspect ratios, the introduction of an orientation distribution of these scatterers could then lower the $\langle \sin^2 \psi \rangle$ value to reach the found value of 0.899.

Thus, through the analysis presented above, it has been established that the sample contains well-oriented scatterers, with a mean aspect ratio larger than 5.

Ruland Streak method For the application of the Ruland Streak method, the q-space ($q = 0.01 - 0.25$ Å^{-1}) has been divided into 40 azimuthal sections (i.e. with a width of $\Delta q = 0.006$Å^{-1}). For each section, the integral breadth has been determined using all datapoints within that section. The result is shown as the blue dotted line in Figure 4.7.

The streak methods, based on both Gaussian and Lorentzian distributions fit poorly to the data. The best fitting profile is that of a Lorentzian distribution of the scatterer normals. The integral breadth B_ψ that is obtained is a value that approaches the integral breadth of the azimuthal curve of the *200* reflection of the PPTA crystallites (found to be 14.8 degrees for Twaron 1000). The length that is determined through the streak method (5.9 or 8.0 Å) appears unrealistically small, as will become apparent in the next paragraphs. Since the fit is also relatively poor, it cannot be considered to be accurate.

These results indicate that the streak method is not exceptionally suited for the analysis of the nanostructure of aramid fibres, which is also supported by the absence of the "butterfly-like" intensity map often encountered in SAXS data subjected to this analysis. The reason for the poor applicability is that the broadening at low angles can no longer be solely ascribed to the length of the scatterer, but also has contributions from the sides of the ellipsoids. Additionally, a contribution to the intensity from a separate system of scatterers with a separate orientation distribution (such as highly oriented fibrillar scattering) may affect this determination.

Debye-Bueche analysis The results of the Debye-Bueche analysis show that the Debye-Bueche model fits reasonably well to the data (shown in Figure 4.8) for Twaron 1000. Above $q = 0.09$ Å^{-1}, however, the model fails to describe the data. For the as spun material, the Debye fit is less satisfactory (cf. Figure 4.9).

Upon closer investigation of the intensity curve of the as-spun sample (Figure 4.9) two slopes can be distinguished in the Debye plot indicating that we may have interface distributions centred around two distinct sizes. This is where the previously mentioned "double Debye" relationship comes into play. By adding intensity from a second interface distribution function, some of the sizes present may be determined. The result of this is depicted in Figure 4.10. The difference in appearance of the intensity in the "Debye"-plots are due to a difference in I_{fl}, which has converged to a (too) large value in the fit with the single Debye function (I_{fl} is determined separately when fitting the Debye and Porod functions). We now obtain two correlation lengths, one very large (and most likely unreliable due to the lack of sufficient data at very low q), and one ordinary size correlation length.

Application of the Debye-Bueche fitting model to the simulated data (shown in Figure 4.4) results in a fit similar to that of Twaron 1000, resulting in a correlation length L_c of 11.9 Å. This correlation length is related to the void size L_v through $L_v = L_c(1-\nu)^{-1}$, where ν is the volume fraction of voids, and therefore the

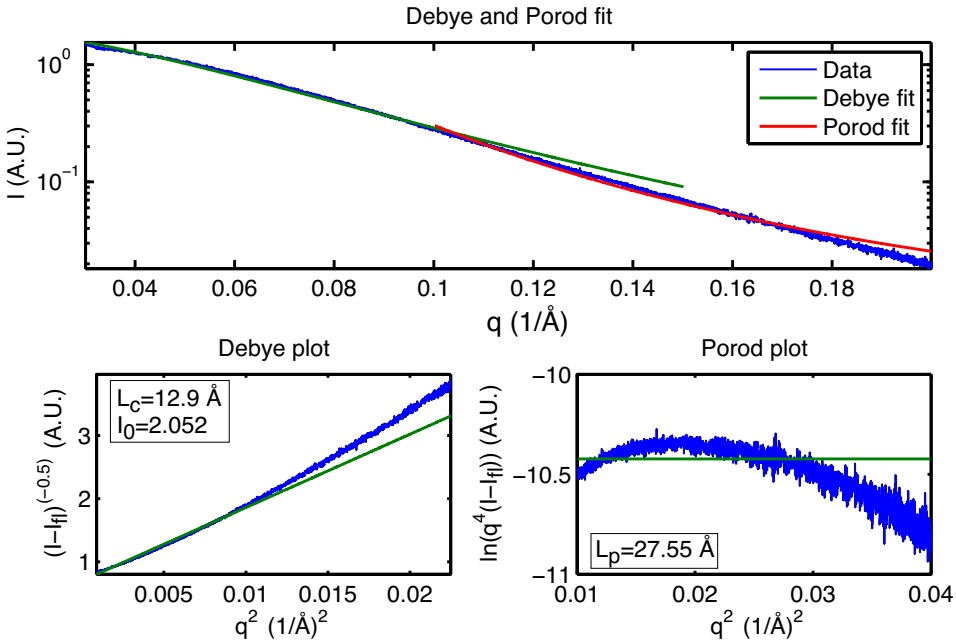

Figure 4.8: *Results from the Debye-Bueche and Porod analysis, as well as the associated Debye and Porod plots applied to the equatorial intensity of Twaron 1000 (a pie section with a width in ψ of 1 degree).*

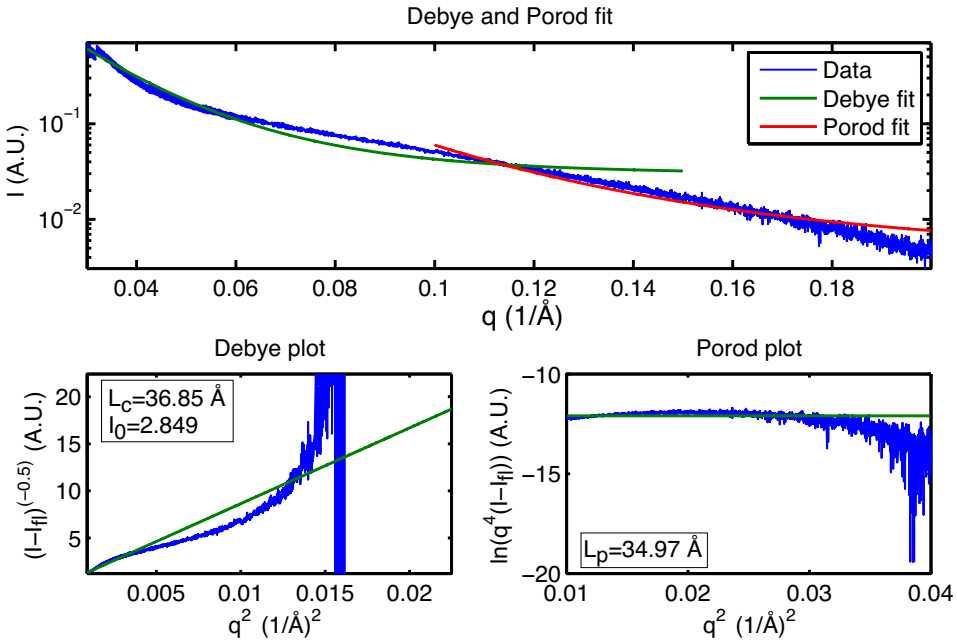

Figure 4.9: *Results from the Debye-Bueche and Porod analysis, as well as the associated Debye and Porod plots applied to the equatorial intensity of as-spun Twaron (a pie section with a width in ψ of 1 degree).*

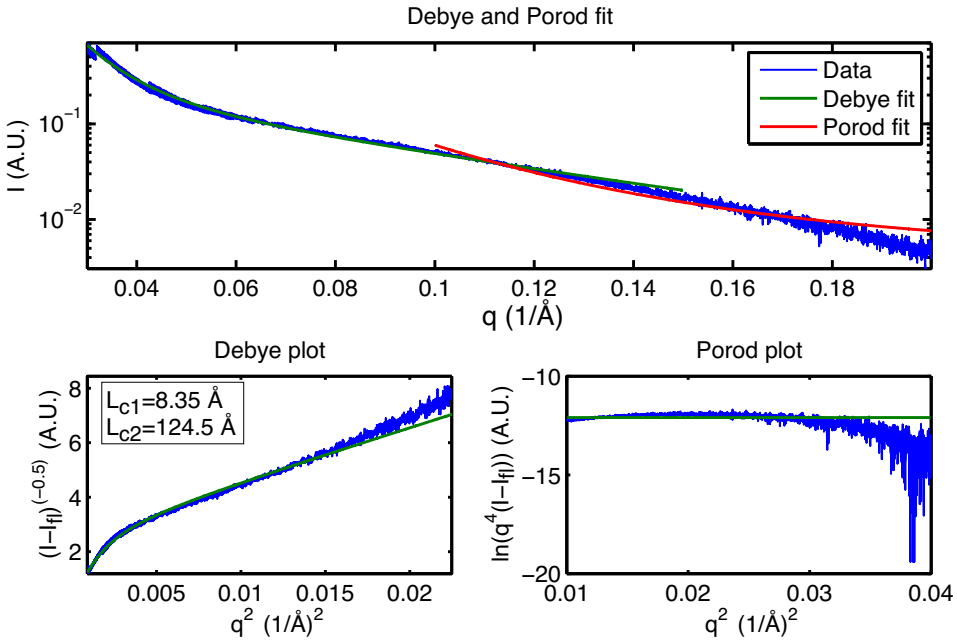

Figure 4.10: *Results from the bimodal Debye-Bueche analysis, as well as the associated Debye and Porod plots applied to the equatorial intensity of as-spun Twaron (a pie section with a width in ψ of 1 degree).*

correlation length approaches the void size for low volume fractions. This is very close to the "mode", also known as the maximum likelihood estimator, of the size distribution that was simulated (these distributions are identical to those shown in Figure 4.12; The maximum likelihood estimator of the short axis is about $R \approx 14$ Å). When we analyse the intensity scattered in the meridional direction (i.e. along the fibre axis), a correlation length of 30.8 Å is obtained. This, again, approaches the mode of the distribution of the long axis of the scatterer, which is at $R \approx 40$.

These results show evidence of the applicability of the Debye-Bueche method, returning a value somewhat below the mean value of the size distribution. Furthermore, the results for the as-spun material indicate that a standard unimodal correlation function fit is severely affected by large size scatterers. The application of a "double Debye"-type bimodal correlation function-based model reveals a significant contribution from large scatterers.

Porod analysis The Porod analysis for Twaron 1000 is shown in Figure 4.8. The fit is less than reliable, as is apparent from the Porod plot (the data should have a linear region at high q). One possible explanation is that the Porod region has not yet been reached in these measurements. Alternatively, there may be a change in the slope, due to graded interfaces [Koberstein et al., 1980], surface roughness [Tang et al., 1986], beginning wide-angle diffraction peaks [Stribeck, 2007], or other Porod slope modifications [Diez and Sobry, 1993; Ruland, 1971; S., 1993].

The Porod method appears to work a little better for the as-spun material, where before the intensity drop at $q^2 = 0.03$ Å^{-2}, the data are described rather well by the model (cf. Figure 4.9). The value of the Porod length (L_p =28 Å) resulting from the Twaron 1000 fit does not compare well with the correlation length obtained from the Debye function (L_c = 13 Å), whereas for as-spun Twaron this Porod length (of L_p = 35 Å) does approach the Debye correlation length (of L_c = 37 Å). Since the Porod length value is heavily dependent on the extrapolation of the intensity to $q = 0$ and $q = \infty$, the extrapolation method may be equally at fault. Values for the surface-to-volume ratio have not been determined, as they assume isotropic scatterer orientation.

Applicability of classical analyses The results so far indicate that the applicability of the Ruland Streak method and the Porod method for the analysis of SAXS data of the investigated aramid yarns is limited. Other classical methods, i.e. the Debye-Bueche method and the Effler Invariant method appear to work

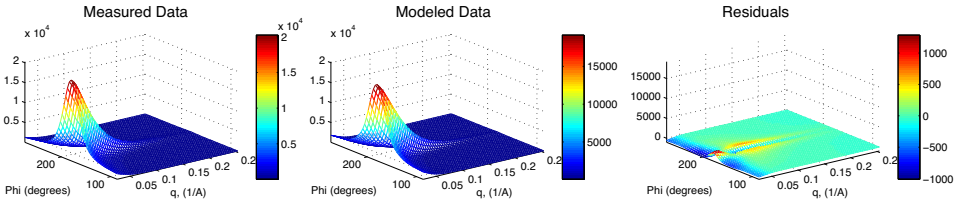

Figure 4.11: *Intensity plots of the Twaron 1000 measurement, compared to the intensity based on the polydisperse ellipsoid model, leaving a small amount of residual intensity.*

well, although for the latter method the aspect ratio of the scatterers must be sufficiently large. In the following paragraphs, results of our new data analysis method will be presented, which makes use of the full 2D scattering pattern. This method not only allows the extraction of average size parameters from the scattering pattern, but it also allows the determination of the complete size distributions of the scatterers in both lateral and longitudinal directions.

Full 2D-data analysis model

Fitting the new model to the Twaron 1000 measurement works very well when done within a q-range of $0.03 - 0.25$ Å^{-1} (c.f. Figure 4.11). This fit results in size distributions as shown in Figure 4.12. The residuals are small, but show systematic deviations. This indicates that the model, whilst good, leaves some intensity unaccounted for. This intensity may be partly due to the shape, orientation and size-distribution assumptions, which will be addressed shortly.

A more intuitive way of showing these distributions, is as the ellipsoids they represent. The maximum likelihood estimator has been plotted in Figure 4.13 as the thick solid line, the mean as the dashed line and the 90% confidence interval as the shaded area. From Figures 4.12 and 4.13, it is clear that the short axis size distribution of the ellipsoids is rather narrow, whereas there is a large variance in the long axis length of the scatterers.

For the precursor material, i.e. the as-spun (AS) Twaron, the fit of the new data analysis model is not satisfactory. Much residual intensity remains, particularly at higher q (see Figure 4.14). As indicated above, when the classical models were discussed, the scattering at low q in the AS Twaron scattering pattern shows a contribution from large scatterers. Thus, our new data analysis model fails here, since only a log-normal distribution is considered and not a bimodal distribution.

Given the residuals for both Twaron 1000 and AS Twaron, it has become necessary to address the causes of the discrepancy. Two variations of the model are discussed

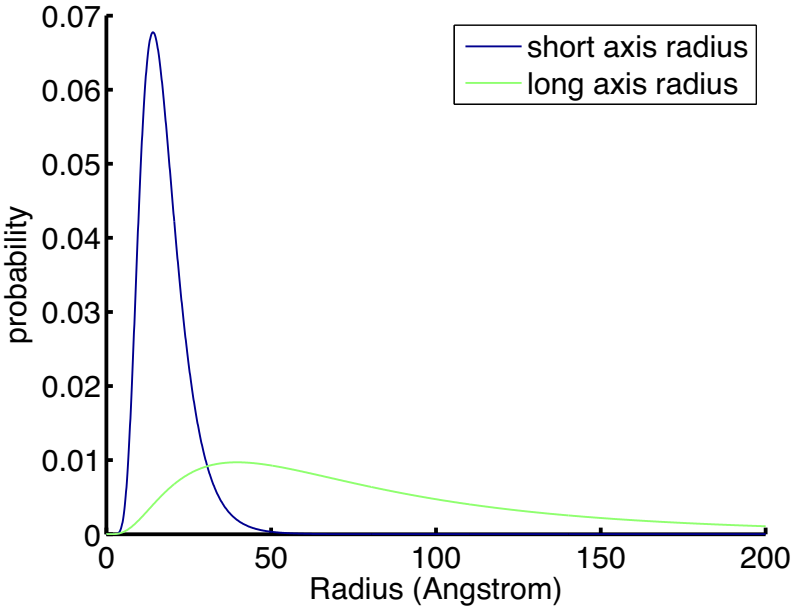

Figure 4.12: *Short axis and long axis size distributions found by fitting the polydisperse ellipsoid model to the Twaron 1000 measurement, shown in Figure 4.5.*

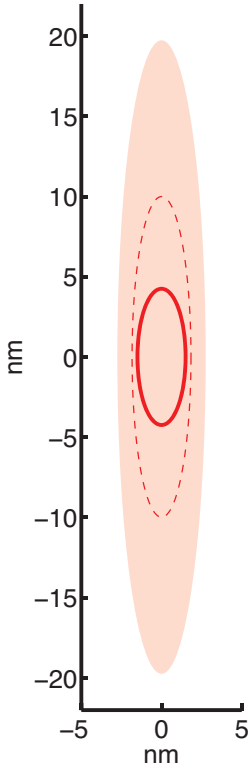

Figure 4.13: *Ellipsoids indicating the maximum likelihood estimator (solid line), mean (dashed line) and 90% confidence interval (shaded area) of the size distributions from Figure 4.12.*

Table 4.2: *Fitting results.*

Original model							
Sample	$f(R_1)$ μ Å	$f(R_1)$ σ Å	$g(R_2)$ μ Å	$g(R_2)$ σ Å			ϵ^2 (A.U.)
Twaron 1000	18.4	49.4	99.9	7600			181
AS Twaron	22.8	250	115	36.4			134
Model with additional large scatterers							
Sample	$f(R_1)$ μ Å	$f(R_1)$ σ Å	$g(R_2)$ μ Å	$g(R_2)$ σ Å	R_{L1} Å	α	ϵ^2
Twaron 1000	19.2	36.7	97.8	5960	223	10.9	147
AS Twaron	12.5	37.5	57.4	2370	243	10.6	55
Model + orientation distribution							
Sample	$f(R_1)$ μ Å	$f(R_1)$ σ Å	$g(R_2)$ μ Å	$g(R_2)$ σ Å	κ		ϵ^2
Twaron 1000	15.5	44.4	91.7	1.95e4	69.1		86
AS Twaron	18.5	134	179	5.32e5	11.2		116

here, which are the addition of a large scatterer to take the low-q scattering into account, and the addition of an orientation distribution to test the assumption of perfectly aligned ellipsoids.

The numerical results from the fitting procedure for various models are given in Table 5.1. The squared sum of residuals (in arbitrary units) is also given to facilitate comparisons. The residuals are graphically displayed in Figure 4.14, so that systematic deviations from the model can be shown.

The accuracy of the resulting parameters can be estimated through calculation of the coefficients of variance (CV = $\frac{\text{Standarddeviation}}{\text{mean}}$). These have been determined from measurements recorded on the DTU Risø rotating anode-based SAXS instrument. The coefficients of variance are given in % in Table 4.3, and are shown to be small even for a laboratory source, and a good characterization of the material can therefore also be obtained from measurements obtained from a laboratory source. One exception is the coefficient of variance of the width of the radius distribution of the model modified with an additional large scatterer, which is about 10%. This

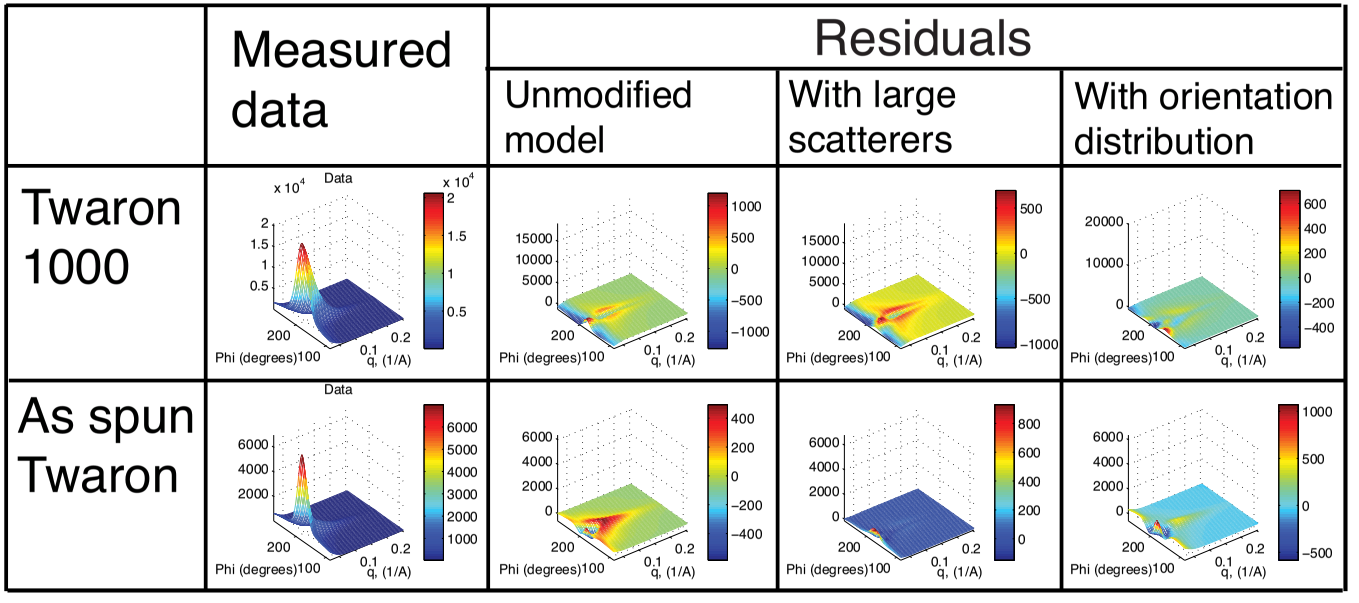

Figure 4.14: *Table of residuals for two modifications of the fit. For Twaron 1000, the most ideal adaptation is the inclusion of an orientation distribution, whereas for as-spun Twaron, additional (large) scatterers improve the fit considerably. Vertical scales are identical to that of the original data on the left-hand side.*

Table 4.3: *Coefficients of variance for the model parameters in percent.*

Model + orientation distribution						
Sample	$f(R_1)$ CV_μ	$f(R_1)$ CV_σ	$g(R_2)$ CV_μ	$g(R_2)$ CV_σ	CV_κ	
Twaron 1000	3.3	2.8	1.9	5.2	2.4	
Model with additional large scatterers						
Sample	$f(R_1)$ CV_μ	$f(R_1)$ CV_σ	$g(R_2)$ CV_μ	$g(R_2)$ CV_σ	CV R_{L1}	CV α
AS Twaron	1.9	11.5	2.0	5.9	0.37	7.6

is likely due to the interfering scattering from the large object.

These results show that for Twaron 1000 the residuals are reduced slightly when an additional scatterer is introduced, but systematic deviations remain. Considering a simple (single-parameter) orientation distribution however, reduces most of the remaining residuals from the original plot, and has a more drastic effect on the squared sum of residuals (shown in Table 5.1). The orientation distribution width has a FWHM of approximately 16 degrees around its mean. These results clearly indicate that the fit to the data can be improved by considering an orientation distribution, and the resulting modeled intensity now more closely follows the scattering pattern as shown in Figure 4.15. Introduction of shape anisotropy, however may be another avenue for improvement.

The results for AS Twaron, however, tell a different story. There, the inclusion of an orientation distribution makes the orientation parameter converge to a very large width of the orientation distribution (low value of κ), reducing slightly the sum of squared residuals. A much better improvement, however, is achieved when large sized scatterers are introduced in the model. This deviation from the log-normal distribution indicates that there is a bimodal distribution present in these fibres, as previously indicated with the bimodal Debye-Bueche model. The sizes that are now obtained (c.f. Table 5.1) for the nanoporous distributions are significantly different from those obtained using the unmodified model. This shows that substantial errors in size estimates can be made if only a single model is used for analysis of both types of fibres, leading to equally erroneous conclusions.

Other results, published elsewhere, show a much higher degree of orientation of large scatterers present in these fibres [Pauw et al., 2009]. This supports the hypothesis that there are separate distributions of scatterers present, one representing (well-oriented) fibrillar scattering, and one originating from a void structure which has been characterized here. Results by Grubb et al. [1991] also support the no-

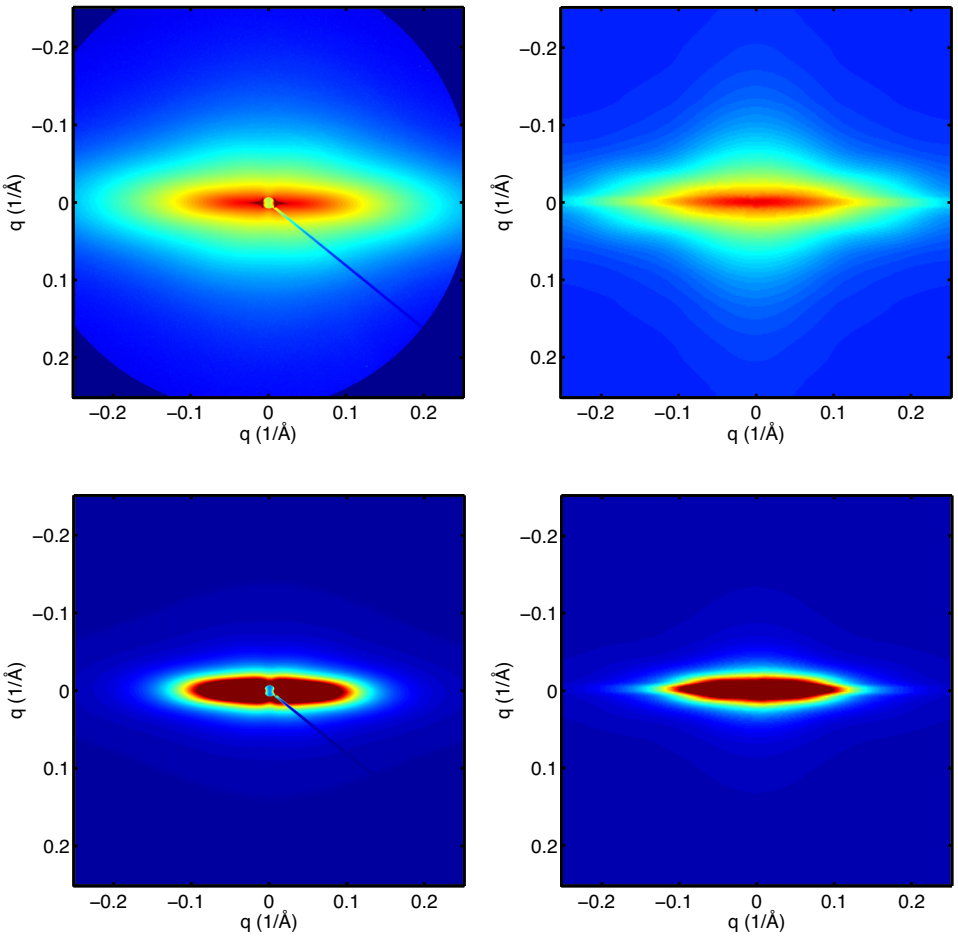

Figure 4.15: *Side-by-side comparison of the scattering pattern (left-hand side) obtained from a bundle of Twaron 1000 filaments and the scattering pattern from the fitting model modified with an orientation distribution (right-hand side). Intensity shown on a logarithmic scale (top) and on a linear scale (bottom).*

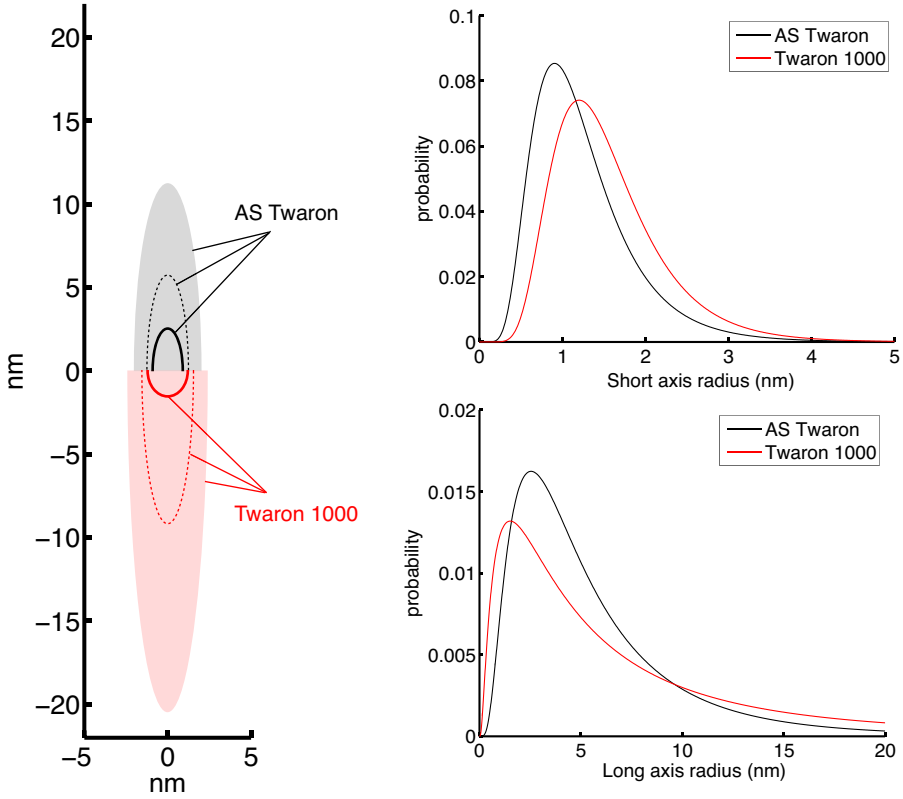

Figure 4.16: *The size distributions of AS Twaron and Twaron 1000 shown as ellipsoids (left) indicating the maximum likelihood estimator (solid line), mean (dashed line) and 90% confidence interval (shaded areas) of the probability curves shown on the right.*

tion of a bimodal distribution. They suggested that differently sized scatterers may be present in the core and shell of the PPTA material. Using on-axis microbeam difraction Davies et al. [2008] also noted a difference in the small-angle scattering patterns originating from the shell of the material as compared to the core, concluding that differently shaped scatterers are present in the shell and the core of the material.

From the results for as-spun and heat-treated Twaron (Twaron 1000), some conclusions may be drawn on the changes in internal structure upon heat treatment. The changes in the pore structure are significant, as can be concluded from Figure 4.16 and Table 5.1. The average lateral pore size increases through heat treatment from 12.5 to 15.5 Å(in agreement with the results obtained from the Debye-Bueche method). The maximum likelihood estimator of the longitudinal size distribution

of the scatterers (Figure 4.16) shifts downward, but the average longitudinal scatterer size increases from 37.5 to 44.4 Ådue to the significantly larger tail of the distribution. The σ-parameters of the distributions increase significantly after heat treatment. The additional large scatterer contribution required in AS Twaron is no longer required in Tw1000, indicating that the heat treatment makes the contribution from the large scatterers less prominent.

These findings suggest that the heat treatment causes the small voids to be sintered, shifting the average size of the pores upward, in agreement with measurements obtained using a slit-collimated Kratky camera for the radii [Klop, 2001]. This sintering closes the gaps between the fibrils, effecting the shift of the fibrillar scattering to q angles beyond the resolution of the SAXS instrument (i.e. the scattered intensity disappears below the beamstop), and may well be linked to increases in crystallite sizes upon heat treatment [Jackson et al., 1994]. This then reduces the contribution of the large scatterer to the scattering pattern. The overall length of the scatterers increases, just like the σ-parameter of the distribution. Lastly, the increase in significance of the orientation distribution of the void structure in the Twaron 1000 is likely to be related to the increase in prominence of the small void contribution rather than to a real increase in void misalignment, as an *increase* of crystallite orientation has been observed with more stringent heat treatments [Krause et al., 1989; Rao et al., 2001].

4.4 Conclusions

The classical analysis methods (the Effler Invariant method and the Ruland Streak method) for the determination of the orientation distribution of scatterers in aramid fibres are insufficient for the determination of the degree of orientation for these scatterers. The application of the analysis models to simulated data and real data supports the notion that the main issue is the relatively low aspect ratio of the scatterers. The low aspect ratio causes off-axis contributions to the intensity that are interpreted as originating from the orientation distribution, whilst they are solely due to the scattering by the (near) perfectly aligned scatterer.

The analysis of the characteristic length-scales of the scatterers present, show that the application of the Debye-Bueche analysis model works. The resulting correlation length (approximating the void size) can be identified as the mode of the scatterer radius distribution in that particular direction. For samples with two distinctly different sized scatterers, a “double Debye” bimodal function can be construed.

Application of the 2D-model presented in this paper shows that the assumptions made are reasonable for describing most of the intensity found in the scattering patterns. The 2D model is based on a system of ellipsoidal scatterers, which are perfectly oriented with respect to the fibre axis. It is assumed that the size distributions of these scatterers can be described by log-normal distributions. Furthermore, the scatterers are assumed to be non-interacting, implying that the scatterers are allowed to intersect.

Adaptations of the model can improve the obtained fits, and may significantly affect the size parameters obtained. One adaptation required for the modeling of the scattering patter of the as-spun aramid material is that a large-sized scatterer should be included. A second adaptation that can be considered for analysis of the scattering pattern of Twaron 1000 is the introduction of an (in-plane) orientation distribution.

Application of the 2D model to the aramid yarn samples, shows that the heat treatment effects an increase in overall void size and distribution widths, both laterally as well as longitudinally, suggesting that the smaller voids are sintered away during the heat treatment. The interfaces between fibrils similarly disappear, making the fibrillar structure much larger. This then causes a shift of the large scattering contribution seen in AS Twaron to below the detection limits of the instrument.

Chapter 5

Tensile and axially compressive strain effects on the structure of PPTA

5.1 Introduction

Microfocused X-ray sources, such as the *cSAXS* beamline at the Swiss Light Source, allow local probing of the structure inside single filaments. The filament diameter of the Twaron studied in this work is typically around 12 micrometers, and the *cSAXS* beamline has a beam with a cross-section of 4 microns in the smallest dimension, thus allowing the local fibrillar structure to be probed.

Local probing is particularly valuable when the filament is exposed to local perturbations, such as bending or stretching. Understanding the filament structural response to bending is essential to the successful use of fibres in applications, as bending causes compressive, shear and tensile forces in the filaments which eventually leads to failure (cf. Figure 5.1). In aramid high-performance polymers the compressive stress at failure is about 20 % of the tensile stress at failure.

Bending failure modes of filaments can generally be classified into tensile failure and kink band formation. Tensile failure occurs with brittle fibres such as glass fibres and carbon fibres, whereas kink band formation occurs mainly in polymer fibres [Fidan et al., 1993]. The latter bending failure mode may be due to Euler buckling, which is expressed as kinks on the surface of the filament, starting from the compressed area of the filaments [Dobb et al., 1981; Dobb and Robson, 1990]. Raman spectroscopy has shown that at these kink bands, the strain in the fibre is

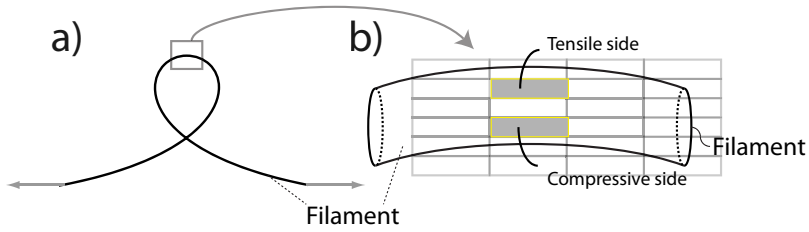

Figure 5.1: *a) The elastica loop experiment, and b) the apex (top) of the loop, where regions under stress are indicated. The size of the shaded areas corresponds to the size of the X-ray beam available at the cSAXS beamline, showing that three to five non-overlapping measurements can be made across the filament diameter.*

reduced [Andrews et al., 1997].

A simple method to control bending is to force the filament into a loop, a method known as the "elastica loop test" (cf. Figure 5.1) [Fidan et al., 1993]. The strain in the sample can then be calculated from the radius of curvature, which is smallest at the apex of the loop, corresponding to the highest strain. In elastic deformation, the zero-strain point occupies the centre of the filament, but will shift as soon as non-elastic deformation takes place. A similar recent experiment shows that bending (of carbon fibres) introduces a strain in the sample, with the zero-strain point close to, but not necessarily exactly at the centre of the filament [Loidl et al., 2005].

In the present study, microfocused SAXS was used for *in-situ* monitoring of loop deformation, using the elastica loop test with a custom-made "loop device". From the scattering pattern we were able to establish the evolution of fibrillar separation in regions with an axially compressive strain, and fibrillar compaction in regions with an imposed tensile strain.

5.2 Experimental

5.2.1 Sample Preparation

The sample was a filament of as spun poly-(*para*-phenylene terephtalamide) (PPTA, a precursor to commercially available Twaron), 12 micrometer in diameter, spun from a liquid crystalline solution of PPTA in sulfuric acid. The filaments have not undergone a heat treatment procedure after the washing and drying steps. The

heat treatment procedure is commonly applied to commercially available filaments to optimize the physical properties.

All samples for the SAXS studies were prepared one week before the scattering experiments, and allowed to dry in vacuum before transportation to the SAXS beamline in a box kept dry with silica gel. Upon arrival at the synchrotron, the samples were subjected to a further 12 hours of vacuum drying before being stored in a box with desiccant. The samples were handled carefully to ensure no damage prior to the bending experiments.

5.2.2 Scanning Electron Microscopy

Scanning Electron Microscopy (SEM) experiments were performed at the Center for Electron Nanoscopy at the Technical University of Denmark (DTU), using a FEI Quanta 200F, operated with an electron acceleration voltage of 2 keV, a spot size of 2.0 nm, and a working distance of 4.5 mm.

5.2.3 SAXS measurements

The SAXS experiments were carried out at the coherent SAXS (*cSAXS*, X12SA) beamline of the Swiss Light Source, using a monochromatic beam with a wavelength of 0.100 nm. The scattered X-rays were collected using a two-dimensional detector, specifically a Pilatus 2M, with a pixel size of 172×172 μm^2 and a total of 1461×1560 pixels [Eikenberry et al., 2003]. The detector area consists of 24 rectangular modules, mounted in a 3×8 arrangement, with small gaps between the modules. This detector was pivotal to the success of the experiment, as it has no electronic (background) noise and a pixel-limited point spread function. Typical exposure times were 1 second per frame, with a read-out time of 5 ms. A 7 m helium-filled flight-tube spanned the flight path between the sample and the detector. The sample was kept in air during the measurements. Alignment was facilitated by a remotely controlled optical microscope, which was also used to monitor and measure the loop width and height. The beam was focused using the second monochromator crystal and a Rhodium-coated mirror to a rectangular cross section of 20×4 μm^2 ($h \times v$, FWHM) at the sample position. The PPTA filaments were sequentially measured with the filament axis oriented parallel to the main axis of the (20 micrometers wide) cross-section of the focused beam (as visualized in Figure 5.1).

The measurements were carried out as mesh scans, where sequential exposures were made after small translations of the sample (typically about 25 microns hor-

izontally, and 5 microns vertically), thus obtaining a "map" of the scattering from different parts of the filament. For each iteration, the loop diameter was reduced, its new size and shape determined by on-line optical microscopy and a new SAXS map was measured. The full duration of all the measurements on one filament typically lasted several hours.

5.2.4 Loop device

For the bending experiments, a custom sample holder was made to meet two criteria: the filament should be kept in a size adjustable loop, and the filament should be accessible for X-ray transmission measurements. A microchannel device to guide the filament and contain the cross-over point was constructed out of sandwiched poly(methyl methacrylate) (PMMA) plates. The bottom plate contains a structure shown in Figure 5.2 (inset) embossed using a CO_2 laser, with a channel depth of approximately 100 microns. The top piece was subsequently attached to the bottom plate by curing under load at 90°C for 30 minutes.

When loading the microchannel device with the filament, care was taken not to damage the filament section that was to be measured. Both ends of the filaments were clamped to a spindle with reversed threads, designed to pull the filament ends apart at equal speed. This increases the strain in the whole loop, and in particular at the apex where the radius of curvature is the smallest. The spindle is driven by a stepper motor, and the sample holder was proven to operate reliably and reproducibly. The clamps and mounted filament are visible in Figure 5.2. During the experiment the cross-over point of the filament is kept in position by the small "notch" and "nose" structures. The filament moves without visible effort through the device, i.e. no "jumps" or other sudden motions are observed during operation, indicating a smooth motion of the filament through the device.

5.2.5 Data reduction

The detector pixels are indexed in terms of momentum transfer q and angle ψ, where q is defined as $q = \lambda^{-1} 4\pi \sin\theta$ with λ the wavelength, and 2θ the scattering angle. ψ is the polar angle in the detector plane. As the scattering is confined to a sharp line of oscillations on the detector, cf. Figure 5.3, a line is extracted along a direction of ψ of maximum scattered intensity using an adapted Bresenham line extraction algorithm (details to be published elsewhere).

Intensity maps were generated by plotting the integrated intensity (over the extracted line) of all measurements of a loop onto a grid to create a scattered intensity

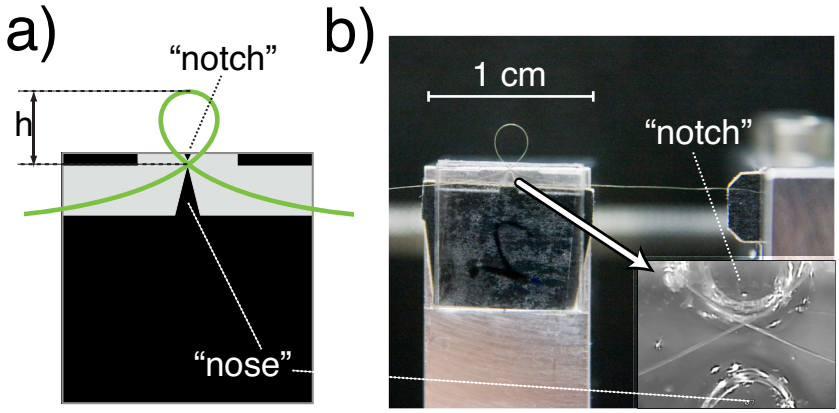

Figure 5.2: *The elastica loop contained within the microchannel device is shown in* a)*, with the loop height* h*, "notch" and "nose" structures indicated (the filament thickness is exaggerated for clarity).* b) *shows the loop device as installed at the SLS, mounted on the motorized stretching device. The inset in* b) *shows the filament cross-over point contained in between the "notch" and "nose" structure of the microchannel device.*

"image" of the object. Compared to integrating over the entire detector area, this procedure yields a better signal-to-noise ratio.

A least squares minimization function was used for the fitting, with logarithms of the intensities to increase the relative weight of the low intensity data points, i.e.:

$$\chi^2 = \frac{\sum_N \left(\log(I_{calc}) - \log(I_{obs})\right)^2}{N - n_{fitparam}} \tag{5.1}$$

Here, χ^2 is the minimization parameter, N the number of datapoints, $n_{fitparam}$ the number of variables of the fitting function, I_{calc} the calculated (model-)intensity and I_{obs} the observed intensity.

A number of models have been tried in an attempt to fit the experimental data, some of which are detailed below. One of the models that was attempted is the analytical scattering function for infinite cylinders [Oster and Riley, 1952]:

$$F_{\mathrm{cyl}} = \frac{2\mathrm{J}_1(qr_c)}{qr_c} \tag{5.2}$$

where J_1 is the Bessel function of the first kind and r_c the radius of the cylinder in Å.

One numerical model capable of describing the experimental data is a numerical model of packed cylinders. A projection of the electron density profile of a cylindri-

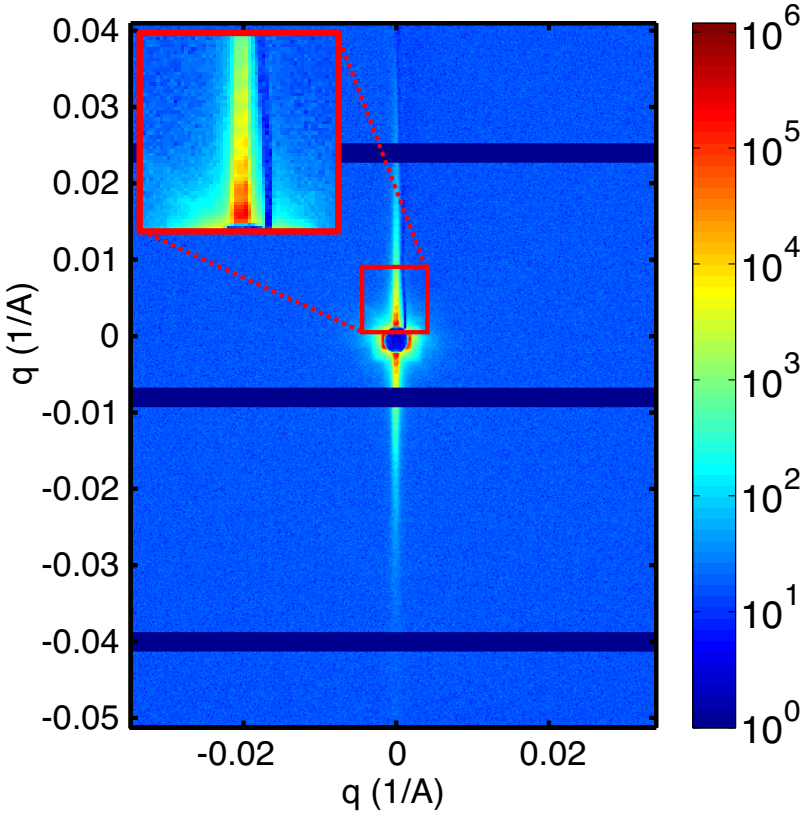

Figure 5.3: *A selected region of the total detector output on a logarithmic intensity scale for a measurement through the PPTA filament, showing the highly anisotropic scattering pattern, the beamstop and the gaps between the detector modules. The main axis of the scattering pattern is vertical ($\psi = 90$ degrees), indicating that the measurement was done on a horizontal part (top) of the looped filament.*

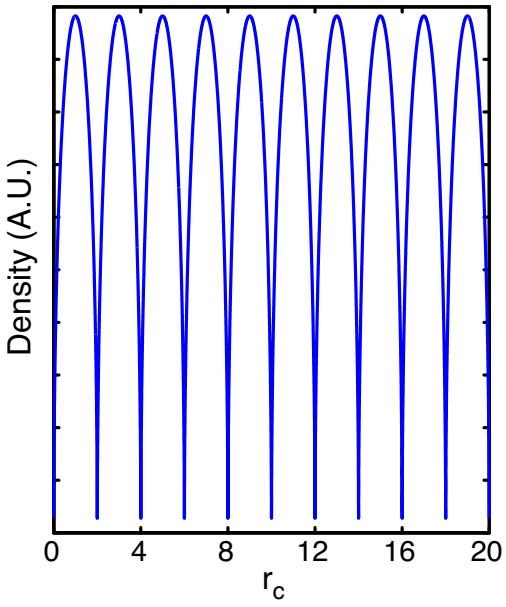

Figure 5.4: *The projected (electron) density profile $\rho(x)_{packed}$, corresponding to a close packed array of ten cylinders with cylinder radii of 200 nm and a spacing of 400 nm, spanning the approximate width of the beam.*

cal cross-section onto a line was used as a basis. Rewriting the Cartesian circular cross-section, we obtain for the projected electron density $\rho(x)$,

$$\rho(x) = \sqrt{1 - \left(\frac{x}{r_c}\right)^2} \tag{5.3}$$

where r_c is the radius of the cross-section in Å. In order to mimic a tightly packed 1D array of cylinders, the profile is replicated by placing copies of itself at a distance of $2r_c$ to generate $\rho(x)_{packed}$. The spacing between the cylinder centres (periodicity) is therefore $D_c = 2r_c$. The cylinders are replicated 10 times to numerically approximate a packed array limited by the width of the beam. The main features of the scattering pattern become independent of the number of replications when this number increases beyond $n \approx 3$. The entire line was quantized using 1×10^4 points, so that each cylinder in the 10-cylinder model is described using 1000 points (cf. Figure 5.4).

The scattered intensity from this profile is proportional to the absolute square of the Fourier transform of the electron density contrast [Stribeck, 2007], i.e.:

$$I(q) = |\mathrm{FT}(\rho(x)_{packed})|^2 \tag{5.4}$$

with FT indicating a one-dimensional Fourier Transform. The intensity decay at higher angles obtained from such numerical computations can be improved slightly by convoluting the intensity with the Fourier transform of a box function with the width of the distance between the sampling points. This procedure reduces the error introduced by the discrete Fourier transform, as is explained in detail by Schmidt-Rohr [2007]. Finally, effects such as beam profile, polydispersity and graded interfaces are modelled by convoluting the intensity with a single Gaussian, since our main interest lies in the determination of the spacing between the scatterers. The width of this Gaussian depends on the size of the scatterers. For small scatterer sizes of about 50 to 100 nm (corresponding to spacings of 100 to 200 nm), the smearing width was set to $\approx 0.001\text{Å}^{-1}$, and for scatterers with large sizes (i.e. ≤ 200 nm, $D_c = 400$ nm) it was set to $\approx 1.5 \times 10^{-4}\text{Å}^{-1}$.

5.3 Results and discussion

5.3.1 Electron microscopy measurements

Figure 5.5 shows a SEM micrograph obtained from a loop of as spun material, where part of the skin layer has delaminated. In Figure 5.6, the inner structure is shown in a filament which was cut using scissors. In the first of the obtained SEM micrographs, a fibrillar structure can be observed lying underneath the skin of the filament (Figure 5.5). The dimensions of these fibrils are about one hundred nanometers (Figure 5.6), whereas the filament diameter is approximately 12 micrometers. The skin in this sample is partially delaminated from the bulk of the filament. The outside of the filament is much less rough than the fibrillar structure lying underneath. In some micrographs, a pronounced ribbon or tape-like fibrillar shape is observed throughout the filament (Figure 5.6), with a high aspect ratio ($\approx 2 - 10$) of the cross-section. In other micrographs the fibrils appear to have a more circular cross-section.

5.3.2 X-ray scattering

Mesh scans through the loop are analysed using the method described in the data reduction section, yielding values for the intensity (and rotation angle) of the scattering pattern. Obtained intensity maps are shown in Figure 5.7. Here, maps are shown for one loop of as spun PPTA at four different strain levels (i.e. loop sizes). The heights of the loop (measured from the cross-over point to the apex of the loop, indicated as h in Figure 5.2) are 7.70, 6.00, 3.92 and 2.93 mm. From

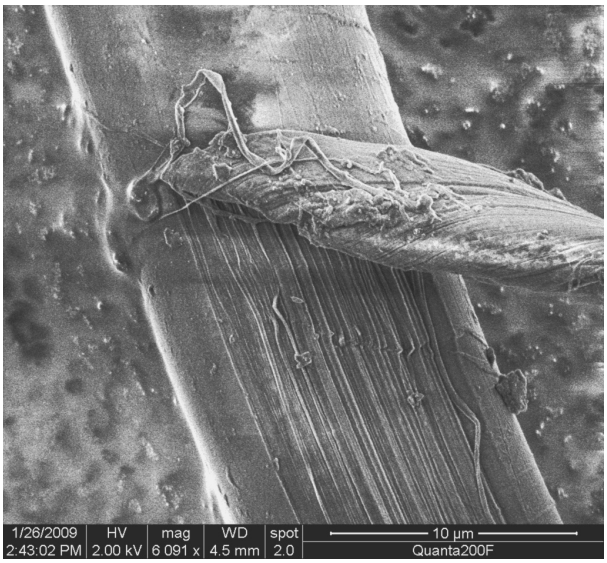

Figure 5.5: *Electron micrograph showing the fibrillar structure underneath the delaminated surface of a single as spun PPTA filament.*

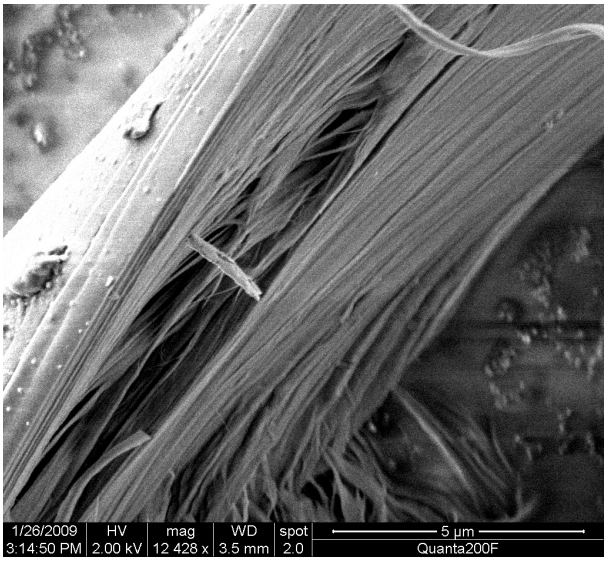

Figure 5.6: *Electron micrograph showing the fibrillar structure underneath the surface of a cut single filament of as spun PPTA. Note in particular the presence of stacked band-shaped fibrils, which are the subject of the subsequent SAXS measurements.*

the simultaneously recorded microscopy images of the loop it was verified that the loop did not shift laterally or rotate during the experiment.

The intensity maps reveal a significant increase in intensity as the loop is pulled smaller. In the loops of smaller diameter, the intensity tends to concentrate near the compressive (inner) side of the apex of the loop. Bending did not have a discernible effect on the degree of anisotropy in the scattering pattern,which remained a sharp line during the experiments. It is therefore unlikely that the increased scattered intensity can be attributed to a strain-induced increase in orientation as observed by Ran et al. [2001]. Excluding that, the integrated intensity underneath a scattering curve is proportional to $V_{irr}\nu_1\nu_2(\rho_1-\rho_2)^2$, where V_irr is the irradiated sample volume, ν_i and ρ_i are the volume fractions and the electron densities of the contrasting phases, respectively. A significant increase in scattering must be caused either by a change in volume fraction (when the volume fractions are not close to $\nu_1 \approx \nu_2 \approx 0.5$) or through a change in electron density contrast. This implies that for these loops, we may either have an increase in the volume fraction of voids (as cracks, slip planes or gaps between buckled fibrils), or that moisture is forced out of voids and thereby increasing the contrast, or a combination of both. This implies that we cannot analyse the total scattered intensity to retrieve the volume of the scatterers without more knowledge of the void content. With the filaments placed in air during the measurement, it is possible that moisture enters some voids accessible from the surface [Saijo et al., 1994]. This will have an effect on the scattered intensity, lowering the contrast between polymer and voids. The intensity scattered from samples with moisture-filled voids is estimated to be approximately 25% that of empty voids by density considerations. It is furthermore not known what effect strain has on the moisture content of these fibres, as it may result in mechanical drying as for example observed with spider silk [Riekel and Vollrath, 2001].

Analysis of the rotation angle of the main line of intensity of the scattering pattern demonstrates that the main scattering pattern axis is always perpendicular to the filament for all observed loop sizes. Analysis of this rotation behaviour enables the calculation of the radius of curvature. The equation $e = r/R_m$ yields the compressive strain (and tensile strain) for filaments with a radius r [Fidan et al., 1993], R_m being the radius of curvature at the apex of the loop. The radii of curvature determined for our four loop sizes are 2.97, 2.27, 1.43 and 1.05 millimeters, corresponding to strain values of 0.0040, 0.0053, 0.0084 and 0.0110, i.e. around published values for PPTA fibre critical compression strains of 0.006 to 0.008 [Fidan et al., 1993]. Reversibility of the loop-induced strain effects have not been investigated.

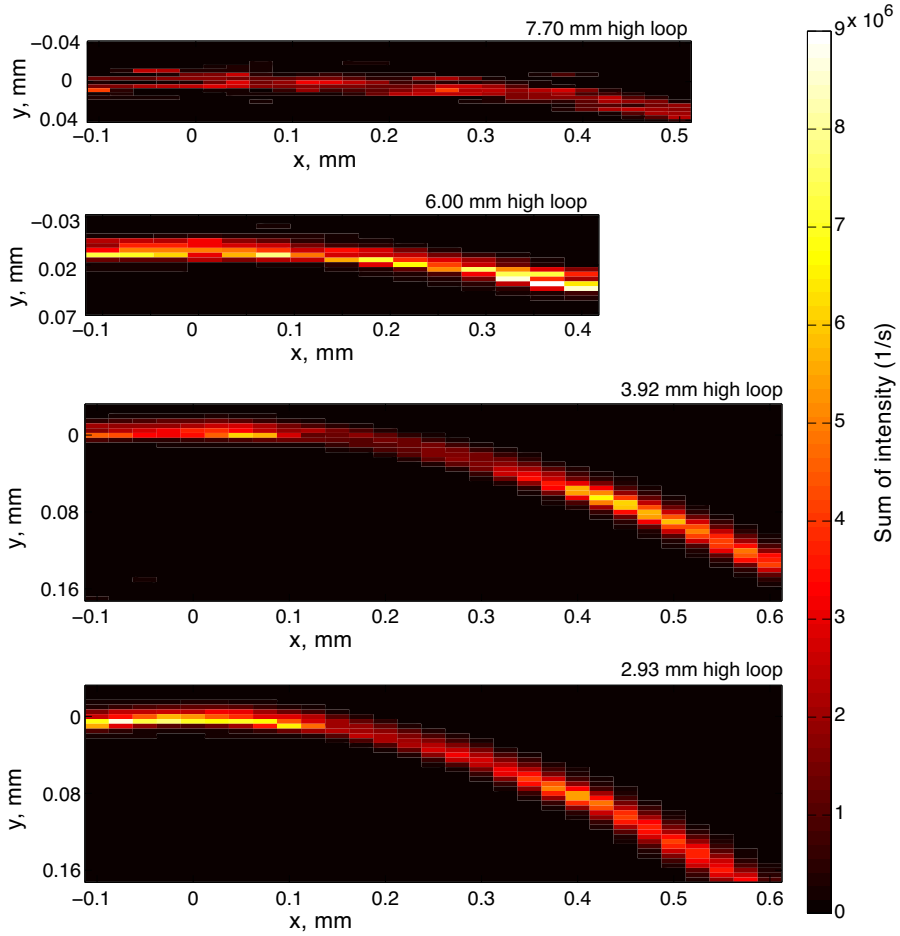

Figure 5.7: *Intensity maps, colour axis units in counts per second integrated over the extracted 1D plots. It is readily seen that the radius of curvature decreases when reducing the loop size (top to bottom), accompanied by an increase of the scattered intensity.*

5.3.3 Localized structure of scatterers

The SAXS scattering patterns obtained from looped as-spun PPTA samples show pronounced periodic intensity oscillations at most measuring points, indicating the presence of relatively monodisperse objects and/or a periodic structure in the filament (see, for example, Figure 5.8). These oscillations are not observed in straight, unstrained filaments (not shown), nor are they seen in looped heat-treated samples (i.e. filaments of commercially available Twaron, which is essentially the as spun material after it has been subjected to heat-treatment under tension). Heat treatment affects the crystallite size in PPTA [Jackson et al., 1994], and may therefore also affect the polydispersity of the fibrillar structure, which may result in the disappearance of oscillations due to polydispersity in the structure.

Observation of these oscillations was unexpected, but a thorough consideration of instrumental sources or other artefacts adds to the confidence that the scattering originates from the sample. The orientation of the streak-shaped scattering pattern being perpendicular to the fibre axis indicates that the scattering originates from the sample. The periodicity is furthermore indicative of a structure at least an order of magnitude smaller than the beam dimension and correlation volume, and two orders of magnitude smaller than the dimension of the sample, making surface scattering effects unlikely. A well-defined skin layer could also cause oscillations to appear, however, this would scatter as an isolated lamellar structure and be visible only when illuminating the edges of the filament, and not when measuring through the core of the filament.

The period of the oscillations indicates a structure with a characteristic dimension of approximately 100-600 nm. The intensity decay follows a q^{-3} slope, which suggests a cylindrical structure. Hypothetically, crack formation or local fibril failure in the samples could result in isolated cylinder-shaped voids. A fit of the data to the form factor of a single cylinder (Equation 5.2), however, shows an offset of the oscillations (Figure 5.8), whilst the period matches. Attempts to fit a lamellar scattering function to the data showed an improved match, but a satisfactory fit could not be achieved, nor with other isolated scatterers of superellipsoidal shape.

Simulating a structure of (a small number of) packed cylinders (shown in Figure 5.4), on the contrary, fits very well to the experimental data (Figure 5.8), as the packing introduces Bragg scattering. This packing has a periodicity identical to the diameter of the cylindrical scatterers, while the cylinder form factor ensures a q^{-3} dependency of the intensity. For the analysis of these experiments, it has been assumed *for computational purposes* that the diameter of the cylindrical scatterers is identical to the spacing between the cylindrical scatterers. It should be noted

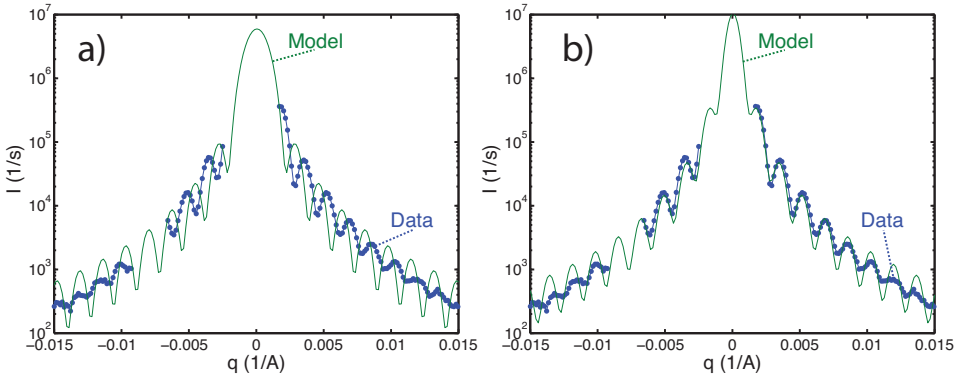

Figure 5.8: *1D scattering plot obtained from the compressive side of a 7.70 mm high loop (intermittent line with datapoints indicated), fitted to:* a) *a cylinder scattering function (continuous line) of a single, perfectly oriented cylinder with a radius of 184.8 nm, and* b) *the scattered intensity of packed cylinders (continuous line) for cylinders with a spacing of 369.6 nm. The two gaps in the data set originate from the beamstop (centre gap) and a gap between detector modules (left-hand gap).*

here that the important factors effecting the oscillations in intensity, are not the size of the scatterers but the periodicity and shape of the scatterers. In other words, the scattering profiles should be roughly cylindrical in shape and spaced at regular intervals, as it is the spacing that determines the period of the oscillations, and the shape that determines the q dependency of the intensity. Instead of a 1D array of close-packed cylinders, a similar oscillatory pattern can be achieved by separating a polydisperse pack of cylindrical profiles at regular intervals, which more closely approaches our physical interpretation which will be discussed at the end of this chapter.

The dampening of the oscillations in the data at higher q can be modelled as an effect of polydispersity, and it was found that considerable polydispersity in the structure was allowed before the oscillations dampen out (to be published elsewhere). Other aspects that play a role in the analysis is the limited beam width which limits the number of cylinders that are irradiated depending on the size of the cylinders and the spacing between the cylindrical scatterers. While we found that the period and offset of the oscillations is not affected in calculations of a pack consisting of a reduced number of cylinders for this experiment, it will be prudent for experiments using smaller beam width to more accurately model the beam profile.

We will here limit ourselves to discussing the possible structures in terms of the simplest possible model accounting for all the experimental observations, which as

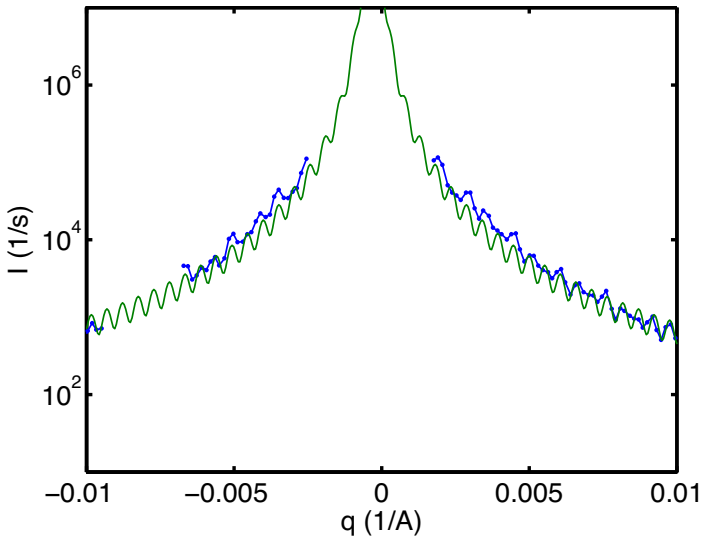

Figure 5.9: *Scattering pattern obtained from the tensile side of the 1.43 mm high loop, where the oscillations indicate a structure with a periodicity of about 800 nanometers.*

discussed turned out to be a 1D array of close-packed cylinders.

An analysis of all obtained scattering patterns allows the generation of a map of the found spacings of the cylindrical structures giving rise to the oscillations, which is shown in Figure 5.11. The observations in that map include the following (which is also tabulated in Table 5.1 and shown in a histogram in Figure 5.12): The 7.70 mm loop exhibits pronounced oscillations. On the tensile (outer) side of the loop, we find oscillations caused by packed cylindrical structures with spacings of approximately 600 nm . On the compressive side, these spacings are about 360 nm. The right side of the map shows intermediate spacings of about 500 nm. The tensile and compressive regions appear to be well separated. The "zero"-strain region appears to be located nearby the centre of the filament. There is one region (indicated in blue) where the scattering pattern did not exhibit clear oscillatory behaviour.

Tightening of the loop further enhances the clear separation of the observed domain sizes in the loop, with the spacings in the tensile side approaching 840 nm whereas the spacings in the compressive side are reduced to about 280 nm in size. The high frequencies in $I(q)$ become challenging to fit, as the period of the oscillations approaches the pixel periodicity, corresponding to a maximum measurable spacing of about 2000 nm for that detector. Additionally, the pixel width effectively forms bins, reducing the visibility of the oscillations. Therefore, moiré-like effects in

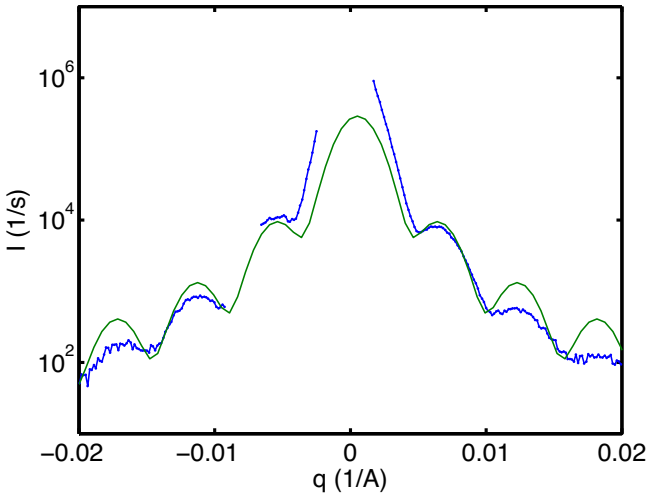

Figure 5.10: *Scattering pattern obtained from the compressive side of the 1.05 mm high loop, where the oscillations indicate a structure with a periodicity of about 100 nanometers.*

Table 5.1: *Tabulation of the loop parameter and fitting results.*

Loop height (mm)	Radius of curvature (mm)	Max. Strain (%)	comp. side mean spacing (nm)	comp. side std. dev.	tensile side mean spacing (nm)	tensile side std. dev.
7.70	2.97	0.40	366	127	562	81
6.00	2.27	0.53	282	302	838	290
3.92	1.43	0.84	252	270	1144	312
2.93	1.05	1.10	167	236	900	308

combination with the pixel size reduce the accuracy of the determination at higher frequency (larger radii) (see for example Figure 5.9).

Further tightening of the loop shows the spacing in the tensile section approaching 1140 nm (c.f. Figure 5.9), while on the compressive side, the spacing shows a reduction to approximately 240 nm.

The smallest loops tend to exhibit less pronounced oscillations. The tensile side mean spacing remains stable at around 900 nm, and compressive side spacings are about 160 nm (c.f. Figure 5.10). All of the results are tabulated in Table 5.1.

The overall trend is that upon the application of tensile strain, there is a slight increase in scattered intensity. The spacing between the scattering elements in-

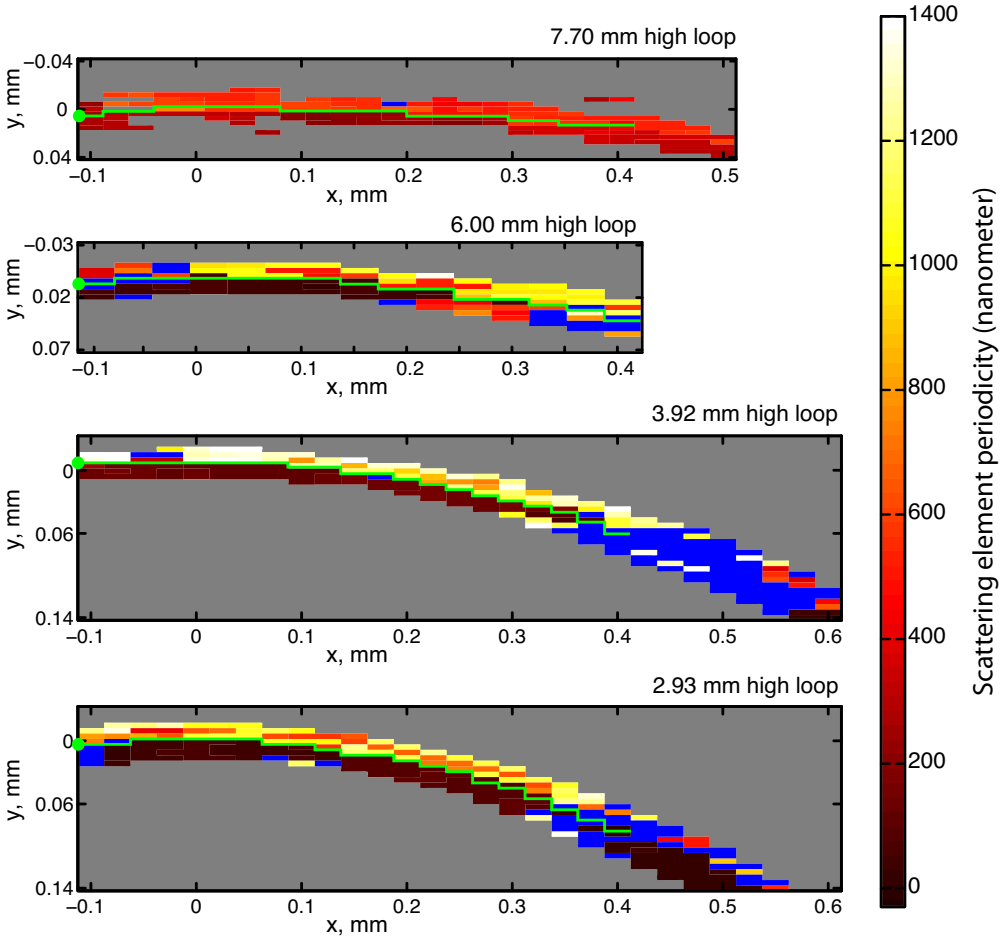

Figure 5.11: *Maps of the scatterer spacings generated from the SAXS data. The horizontal and vertical axis units are in millimeters, color axis units depict the spacing (in Å) between the cylinder centres that was used to fit the oscillations in the extracted 1D plot. The blue colour indicates regions where no clear oscillations were seen. The green line, halfway between the top and bottom of the filament, indicates the separation boundary between regions of compressive and tensile strain.*

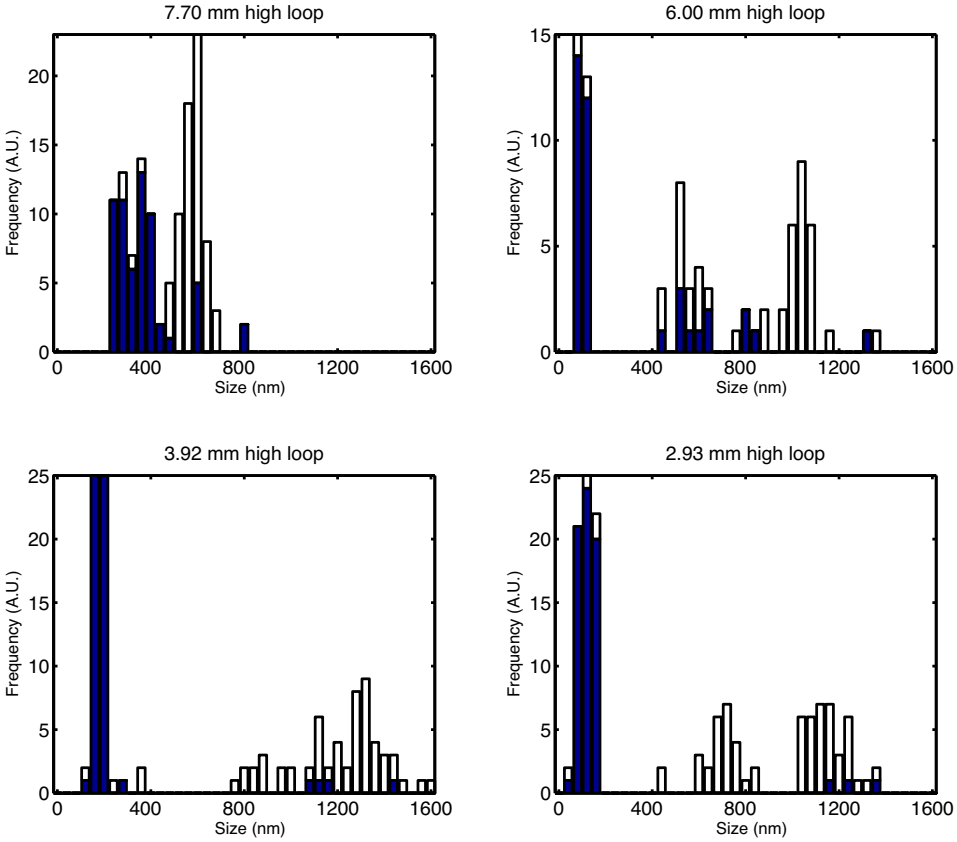

Figure 5.12: *Size histograms for the compressive (dark) and tensile (white) sections of the loops.*

creases initially from about 300 nm for the 7.7 mm high loop, to approximately 500 nm for the 2.93 mm loop, and remains there for the duration of the experiment. On the compressive side, the scattering intensity increases more than in the tensile section, and the spacings between the scattering elements are continuously reduced from 500 nm to less than 200 nm.

This can be explained by considering each macrofibril inside the filament to be a packing of smaller fibrils. Upon bending, the strain upon the macrofibril causes it to split into its component fibrils along crack planes, perpendicular to the direction of the bending. On the compressive side, an increasing number of cracks and splits causes the apparent size to reduce. This is supported by observations by Greenwood and Rose, who made observations that kink band formation is related to fibrillar separation in axially compressed fibres [Greenwood and Rose, 1974]. This fibrillar separation results in an improved contrast in the projected electron density profile and thus a higher scattered intensity. On the tensile side, sets of fibrils are packed tightly together, so that virtually no interfibrillar space exists (i.e. boundaries disappear) and they scatter as a single element. This significantly increases the periodicity (spacing) between the scatterer centres. These effects are conceptually indicated in Figure 5.13.

In this artist's impression, several aspects of the internal structure have to be consolidated. Firstly, the structure in the SEM micrographs indicate a tape-like fibrillar structure underneath a smoother skin layer. Others have indicated the presence of a radial texture present in PPTA filaments [Davies et al., 2008; Li et al., 1983], which may also be present. A radially oriented fibrillar structure not unlike the one shown here closely resembles the structure as determined by Yabuki et al. [1976]. Finally, in order to achieve the structure required for obtaining the scattering pattern, at least part of the structure must show periodic interfaces parallel to the direction of bending. These periodic interfaces are indicative of strain relief effects caused by the axial strain gradient present. Differences in periodicity between the tensile side and compressive side may indicate a different method for tensile and compressive stress relief at those sides. At the compressive side, there is evidence for fibrillar separation, at the tensile side, these may be slip planes.

Information on the strain release mechanism, localization and other aspects of the strain release may be clarified in further experiments. A smaller beam size would be required, with a lower limit of one micron (as the beam has to remain larger than the scatterers we wish to observe). Rotation of the bent filament with respect to the incoming beam should reveal more about the directionality, shape and rotation of the scattering objects. An in-vacuum sample chamber would reduce the background scattering and moisture uptake in the sample. Lastly, in-situ WAXS experiments can act as a local probe for the strain on the crystallites,

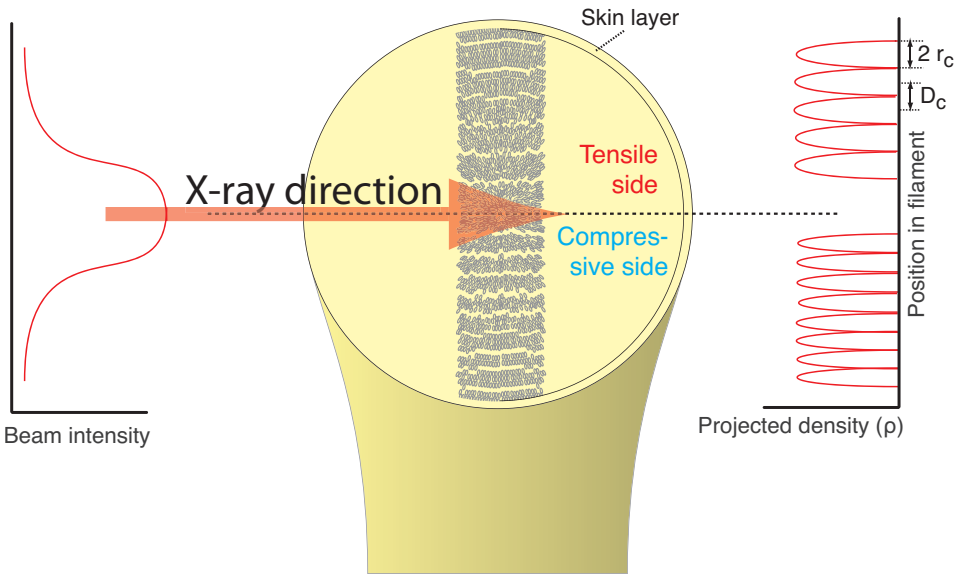

Figure 5.13: *Artist's impression of the cross-section of the looped filament, showing packing of fibrils in the tensile side, and fibrillar separation occurring in the compressive side. The projected electron density is shown on the right-hand side, showing cylindrical profiles with radii of approximately 250 nm (and a spacing D_c of 500 nm) on the compressive side and 400 nm (D_c 800 nm) on the tensile side.*

as their reflection positions have been observed to be dependent on the strain [Gaymans et al., 1976]. Initial measurements obtained from the BW2 beamline at HASYLAB, however, show no visible effect of this strain on the diffraction peaks, supporting the notion of a strain relief mechanism.

5.4 Conclusions

To conclude, filaments of as spun PPTA material contain a packing of fibrils which is easily observed using SEM. These fibrils appear to have a cylinder- to tape-like shape with varying cross-section aspect ratios. The results obtained from microbeam SAXS experiments indicate that in this material (which has not undergone heat-treatment under tension), fibrillar separation can occur at bending radii smaller than several millimeters. This fibrillar separation process appears at the compressive side as a reduction in overall fibril spacing upon an increase in axially compressive strain. On the tensile side, there appears to be a fibrillar compaction (packing), where a clear increase in apparent fibrillar spacing results from the imposed strain, likely caused by the disappearing of interfibrillar boundaries due to the compaction. Whilst the onset of these processes was not observed, it is clear that they must occur at bending radii of several millimeters, as oscillations were not observed in straight filament sections. The fact that oscillations were not observed for heat treated filaments indicates that the heat treatment procedure significantly affects this quite remarkable fibrillar structure.

Chapter 6

Effect of annealing and stress on the nanostructure of PPTA

As the physical properties of the fibre change when undergoing a tensioned heat treatment procedure, it is important to get insight into the nanostructural behaviour under these conditions, as it may then become possible to reveal structure-property relationships. Therefore, now that an analysis methodology has been established, a closer look can be taken at the behaviour of the fibre under tensile load and increased temperature.

6.1 Design of the in-situ tensile stage

6.1.1 Design considerations

In order to apply stress and elevated temperatures to the fibre, an in-situ, in-vacuum heating tensile stage was constructed. The stage is capable of exerting stress on the (heated) fibre approaching the maximum tensile stress, which implies that considerable attention had to be paid to several aspects of the design, in particular to the clamps. The footprint of the stage was also kept small in order for it not to interfere with the SAXS set-up at the beamline. The weight had to be kept low so that it can be placed on top of motor stages (present at the beamline) used for alignment of the sample stage in the beam. While the sample chamber sits in air (on top of the motor stages), the sample itself should be kept in vacuum in order to prevent moisture uptake from affecting the scattering pattern, and therefore the tensile stage is enclosed by a small vacuum chamber with mica

windows. Heating is done (in vacuum) through radiative heat transfer alone, to ensure an unobstructed beam path.

The following decisions were made for obtaining the final design:

- The main feature of the clamp (c.f. Figure 6.1) is a u-turn around which the fibre is led, with the radius of curvature in the bend being 20mm (values recommended by Teijin Aramid BV range from 20 to 30 mm). The fibre is subsequently clamped on the other side using two clamps made from aluminium. The clamp material is stainless steel, chosen for its hardness. A shallow, round groove is added to ensure that the fibre is kept at the right height in the sample chamber, and that the filaments pack nicely. One clamp is stationary whilst the other is pulled.

- The mobile clamp (c.f. Figure 6.2) is pulled using pneumatics. This choice means that instead of the more common method of applying strain (using spindles), stress is applied. Using pneumatics instead of spindles, furthermore, results in a much smaller footprint, no heavy spindles, and a control system using reduction valves. The drawback is that the dynamic range of the sample stage is limited.

- The mobile clamp is prevented from moving in non-tensile directions by a central column, the lid and floor of the vacuum box.

- The box is made from stainless steel, as it has poor heat conductivity, a high hardness and a low tendency for moving elements against its surfaces to "snag" on the inside surfaces (as opposed to aluminium, for example, which damages very easily and moving elements along aluminium "snag" easily).

- The oven is made from aluminium, as it conducts heat nearly as good as copper, and is not as soft. Additionally, it also does not oxidize in an unsightly manner.

- The windows are made from thin sheets of mica, used before in a liquid sample oven, as they exhibit only a small amount of small-angle scattering. Rubber seals are Viton seals as they can withstand temperatures in excess of 200 degrees Centigrade.

- The control system for the pneumatic pistons consists of two reduction valves (one per side of the pistons), and two manometers with digital read-outs. Additionally, to prevent damage to the manometers, small pressure cylinders are placed between the control system and the pistons, so that when the fibre breaks and the clamp shoots outward, the sudden pressure changes experienced by the pistons are not directly relayed to the control system.

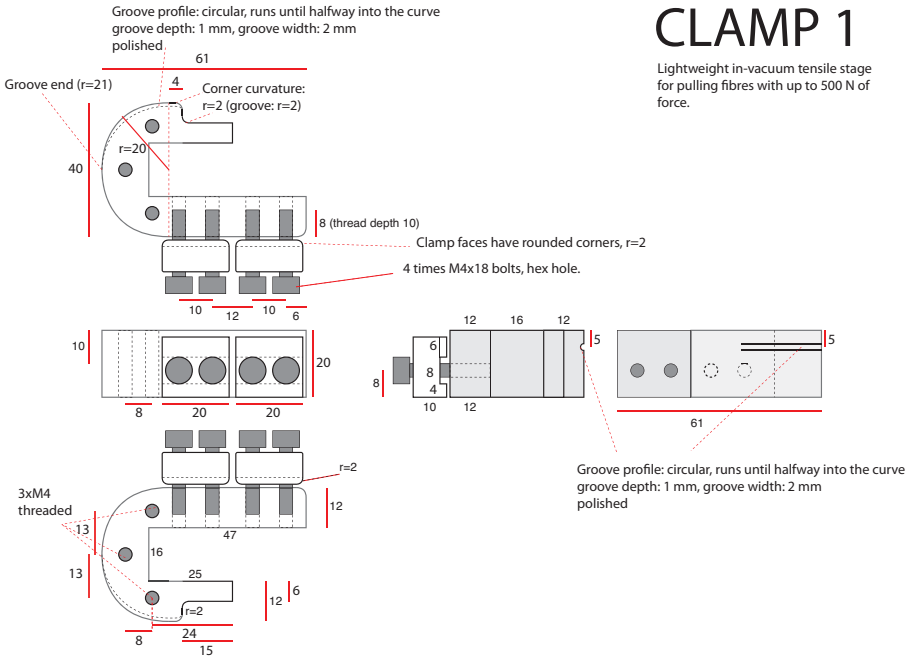

Figure 6.1: *Stationary clamp design.*

The temperature control system consists of a Eurotherm controller with a solid-state relay.

As can be seen in Figures 6.1 and 6.2, the clamps contain a gap in the centre. This gap is intended for a central column to fit in. Different clamps can then fit in the vacuum box around this central column if needed. The stationary clamp is also less long than the mobile clamp on the measurement side, which is done to make room for the oven. The clamps also do not touch the fibre after the curvature of the u-bend has been completed on the measurement side. Lastly, on the attachment side the grip faces are flat.

6.1.2 Tensile stage performance tests and operation notes

In order to test the sample chamber, the clamps were loaded with fibres of Twaron 1055. The fibre consistently broke at a pressure of about 7.2 bar with a non-evacuated chamber (With the chamber evacuated, the pressure read-out is off-set by one bar), which corresponds to 338 N (the pulling side of the piston exerts a force of 47 N/bar according to the supplied documentation). This corresponds

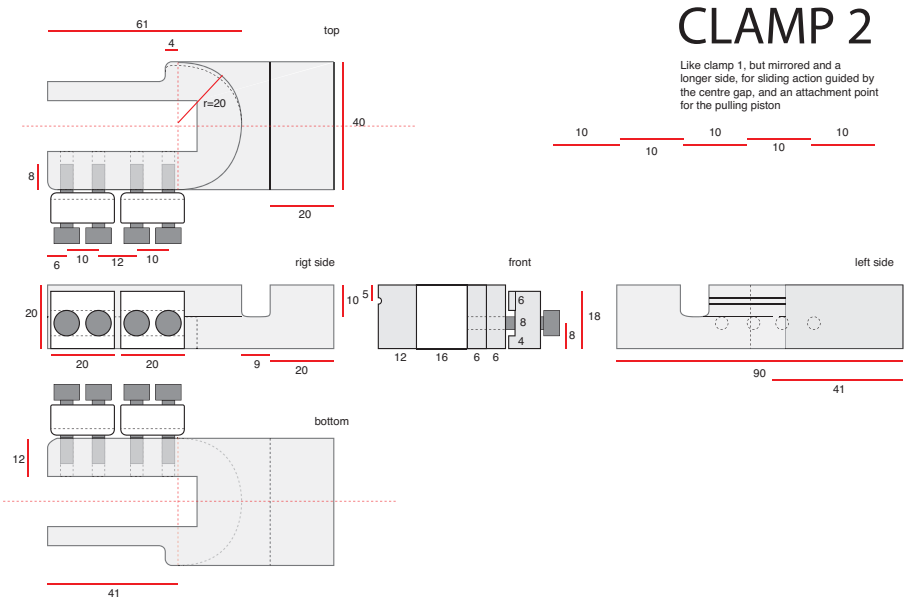

Figure 6.2: *Mobile clamp design.*

well with the Teijin values for that fibre, who found a maximum of 372 N, an average of 335N and a lower limit of 290N. During the beamtime, Twaron 1000 at normal temperature broke at about 8.8 bars in vacuum (366N). For Twaron 1000 at 200 degrees Centigrade, the fibre broke at 7.5 bar (305N) and 7 bar (282N). As spun Twaron broke at about 7.6 bars (310N) at room temperature, and 6 bars (235N) at 200 degrees. Only one sample exhibited slip at the clamping points during the experiments, and all the breaking points of the fibre appeared in the free-standing section of the fibre, i.e. not on the clamping points. Therefore, the tentative conclusion may be drawn that the tensile stage and clamps are suited for these samples.

The heating stage was limited to 200 degrees due to the teflon baseplate used to isolate the oven. This unfortunately meant that only a small part of the parameter space could be investigated.

Slight melting of the teflon during the initial stages of the experiments also meant the oven X-ray path was no longer in line with the entrance and exit windows, requiring expansion of this path through increasing of the oven X-ray path diameter from 2 to 4 mm.

The mica windows performed well, but the entrance window somehow exhibited some scattering when an X-ray beam of a large diameter was used. Replacing this

window with Kapton did not improve this, so that a microbeam was used for the experiments. In this case, none of the windows exhibited any scattering. In the future, a larger entrance window and exit window may be preferred, especially given the rather large distance (40mm) between the windows, which with small window holes requires a more accurate alignment of the sample chamber.

6.1.3 Suggestions for future improvements

The sample stage performed adequately, but for future versions, several aspects can be improved.

- Instead of using pistons that pull, pushing pistons may be more appropriate, as more force can then be applied. This means that smaller pistons can be used.
- more suitable piston designs are available that could push from the centre of the stage, reducing its footprint and reducing the requirements on the box shape and sturdiness.
- The oven has to be redesigned. The oven X-ray path should be made as short as possible, it's mounting should be done with three bolts so its angle can be adjusted, and the isolation baseplate should not be made of teflon, but ceramics instead so higher temperatures can be reached. Ideally, temperatures up to 500 degrees centigrade would be preferred.
- The entrance and exit windows should be made slightly larger depending on the distance between the windows.
- Mounting the stage on a lockable ball-bearing slide would mean that accessibility is improved, making it easier to replace samples. With a slide, the stage can be moved out from between the flight tubes when new samples are being mounted.
- For other samples, the dynamic range of the stage may be slightly limited (the pistons only start moving due to their construction when about 1 bar of pressure is applied, which implies that almost 50N has to be applied as a minimum). To improve this, the sliding clamp could be mounted on a ball-bearing slide to reduce friction, and a secondary set of (small) pistons can be mounted in a telescopic fashion to apply pretension or to apply stress below the dynamic range of the "big" pistons.
- The clamps could be made at least 5mm less high. The box lid and floor, if the force of the pistons does not have to be transferred through them, can

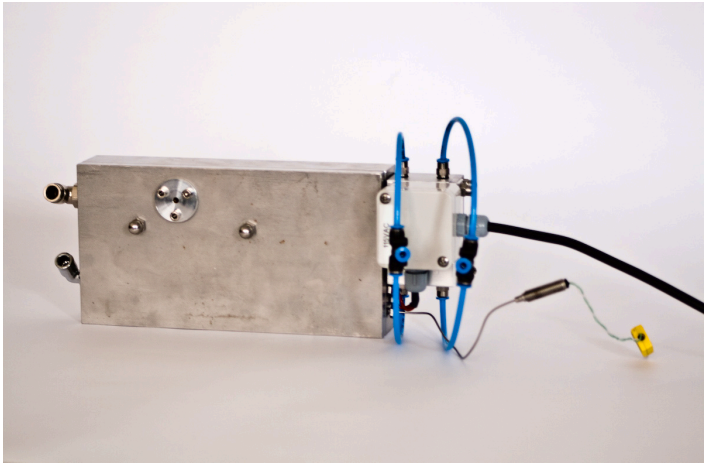

Figure 6.3: *Completed tensile stage.*

be considerably reduced in thickness.

- Pistons with rudimentary position sensing could aid in indicating when the pistons are fully retracted (i.e. when the sample is broken).

- Ideally, measuring the extension of the sample would be useful. This can be achieved optically, by drawing markers on the sample and measuring optically the extension, which would require the addition of an optically transparent window and an in-line microscope. Judging the sample extension from the clamp motion is unlikely to give reliable results as the fibre may slip on sections of the clamps during the pulling operation. Physical measurement devices would likely break the moment the sample breaks and the clamps move suddenly at high speeds

- Instead of pneumatics, the application of hydraulics would result in much smaller pistons being applied and a much reduced sudden clamp motion when the sample breaks. Additionally, the dynamic range may then be much larger. Much more care needs to be taken with hydraulics with respect to the connection and control of the pressure. The application of old HPLC or GPC pumps could provide an inexpensive solution for the control system.

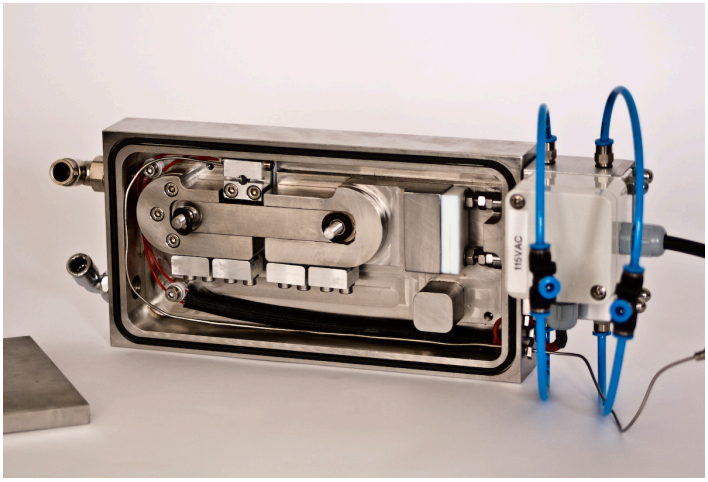

Figure 6.4: *Internals of the completed tensile stage.*

6.2 Statistics on the determined parameters

For determining the significance of observed changes in the structural parameters obtained from analysis of the experimental scattering patterns, the standard deviation or the coefficient of variance for these parameters have to be determined.

For this purpose, several measurement sets were selected. Firstly, five frames of Twaron 1000 were measured to determine the variance in the determined parameters between different samples of the same material. Additionally, several sequential measurements were obtained for Twaron 1000 at constant temperature and constant pressure in order to determine whether the nanostructure remained stable under prolonged duress. In neither case were any time-dependent effects observed during the measurement period of several hours, so that these sets can instead be used to determine what the variance is of the determined parameters for different measurements on the same sample. This can then be used to give statistical significance to observed nanostructural parameter changes upon the application of stress or elevated temperatures measured on the same sample.

The scattering patterns obtained from these measurements have been analysed using the newly developed model described in chapter 4, more specifically paragraph 4.2.5. The coefficients of variance determined for each parameter are tabulated in Table 6.1. From these results, it is apparent that the consecutive measurements on the same sample provide much better statistics than what is obtained from separate samples of material. This data furthermore supports the following observed

Table 6.1: *Coefficients of variance of the size distribution and orientation parameters from fitting with the polydisperse ellipsoid model modified with an orientation distribution as described in chapter 4.*

Samples	$f(R_1)$ CV_μ (%)	$f(R_1)$ CV_σ (%)	$g(R_2)$ CV_μ (%)	$g(R_2)$ CV_σ (%)	CV_κ (%)
#015-019: 5 frames of Twaron 1000	12	1.6	9.1	0.9	9.8
#030-036: 7 measurements of Twaron 1000 at 200°C	1.4	0.3	1.8	0.4	0.8
#002-006: 5 measurements of Twaron 1000 at 235N	5.7	0.6	1.7	0.5	4.2

changes, as the changes in observed structure discussed in the subsequent sections are small but statistically significant.

6.3 Stress and temperature effects on the nanostructure of Twaron 1000

The effect of stress and temperature on the nanostructure of Twaron 1000 has been investigated using the in-situ stage. All measurements resemble the pattern shown in Figure 6.6, and no clearly visible changes in the scattering pattern are observed. Subtraction of scattering patterns, however, do reveal that changes are taking place. The new analysis methodology developed in chapter 4 is able to detect changes in the nanostructural parameters and it is these changes that are interpreted here.

All results from the experiments are tabulated in Table E.1 for Twaron 1000, and tb:bw4ast for the as-spun Twaron samples. In the following paragraphs, only the most significant results are discussed in order to maintain coherence in the story. Unfortunately, these measurements were obtained only two months before the end of the project, and therefore what follows here is a limited analysis. More time is required to fully comprehend the impact of the effects of the combined stress and strain.

Table 6.2: *Samples related to the experiments with increasing stress at room temperature*

Sample #	description	$f(R_1)$ μ	$f(R_1)$ σ	$g(R_2)$ μ	$g(R_2)$ σ	κ
001	0 bar 27°C	16.3	37.9	100	2.3E+04	91.7
002-006	6 bar 27°C	15.8	39.6	112	2.59E+04	152
007	7 bar 27°C	15.4	40.8	112	2.85E+04	137
008	8 bar 27°C (broken)	15.1	41.8	110	2.93E+04	152
009	0 bar 27°C (new sample)	16.7	35	103	2.29E+04	92.4
010	2 bar 27°C	16.2	35.1	105	2.85E+04	100
011	4 bar 27°C	16.8	34.4	113	2.24E+04	124
012	8 bar 27°C	15.2	38.5	119	3.29E+04	169
013	0 bar 27°C (released)	16.2	42.8	111	2.31E+04	113

6.3.1 Increasing stress at room temperature

The effect of increased stress at room temperature has been investigated. 330N was gradually applied to the sample. The final structure at high stress is compared with the starting structure in Figure 6.5. From this figure we can clearly see an effect of stress on the alignment and the shape of the nanostructure in the fibre. The alignment increases as the stress is applied, and the length of the pores increases, while the width decreases slightly. This is in line with what such a nanostructure would do in an elastic situation.

Upon returning the clamp to the starting position, it was found that some inelastic strain has occurred at that point. In order to measure the fibre in the final situation, it had to be pulled taut, which was done by pulling the clamp using 2 bar of pressure on the pistons after which the pressure was released. The final state of the fibre after the strain cycle is a slightly altered structure from the starting point (comparing sample 013 with sample 009, as can be read from Tables 6.2 and E.1), indicating that some inelastic deformation has taken place.

6.3.2 Increasing temperature without stress

The effect of temperature can be observed by comparing a sample heated gradually to 200°C, with a sample at 50°C, as shown in Figure 6.7. No change in the orientation of the scatterers is observed, but the overall length does decrease slightly. The mean width increases, which may indicate sintering of voids with small dimensions, although it is difficult to determine this last observation with

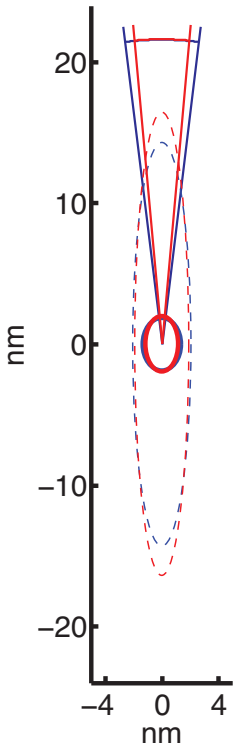

Figure 6.5: *The effect of 330N of force on a bundle of Twaron 1000 (red) as compared to the unstressed sample (blue)*

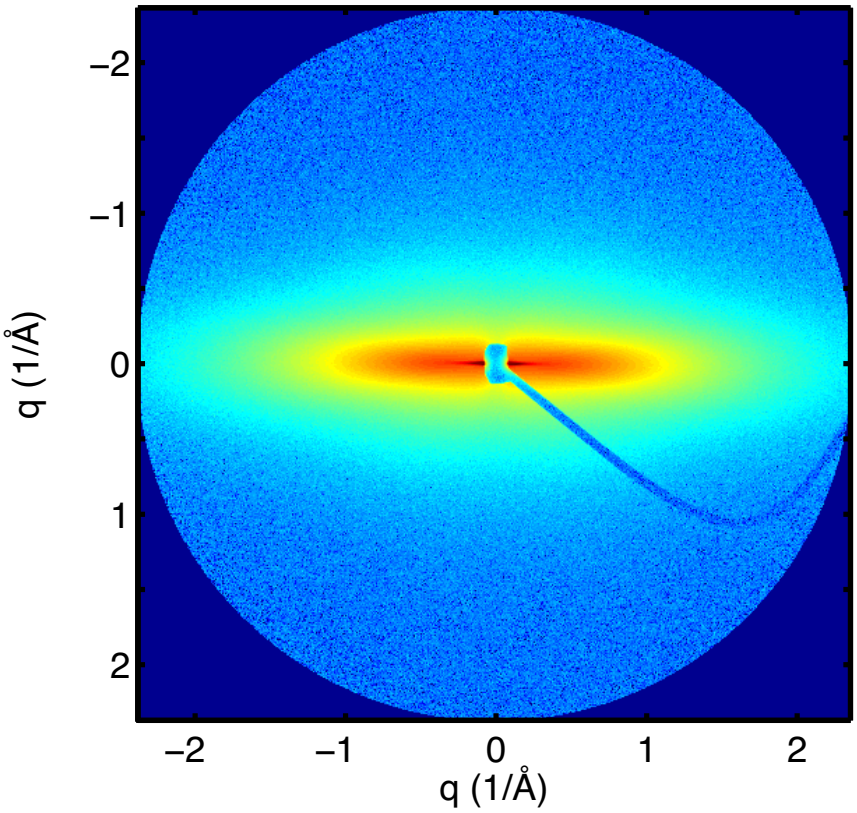

Figure 6.6: *A measurement of an unstrained bundle of Twaron 1000. No clearly visible change in scattering pattern is observed in these experiments.*

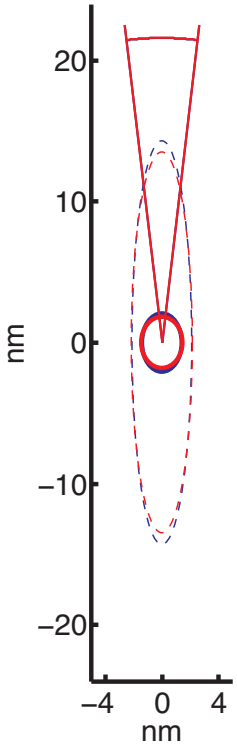

Figure 6.7: *The effect of 200° C on a bundle of unstressed Twaron 1000 (red) as compared to the initial unstressed sample (blue) at 50° C.*

sufficient accuracy. It is likely that the temperature achieved is still too low to observe any major changes in the structure. The sample numbers for this set have been given in Table 6.3.

6.3.3 Increasing stress at high temperature

The combined effect of the two previously discussed cases should prove interesting. On the one hand we have a reduction of the length of the voids when the temperature is increased, and on the other hand an increase in length is observed upon the application of stress. The effect of the application of stress on a sample heated to 200 degrees is shown in Figure 6.8. From that figure, we can determine that the effect of increased stress at high temperature is an increase in orientation (due to the applied strain), and a reduction in length (due to the increased temperature, the effect of which must be dominating). The width of the voids decreases as well,

Table 6.3: *Samples related to the experiments with increasing temperature without stress*

Sample #	description	$f(R_1)$ μ	$f(R_1)$ σ	$g(R_2)$ μ	$g(R_2)$ σ	κ
021	0 bar, 50°C	16.9	36.2	102	1.95E+04	98.6
022	0 bar, 100°C	17	35.1	100	1.9E+04	100
023	0 bar, 150°C	17.1	34.2	97.6	1.9E+04	100
024	0 bar, 200°C	17.4	33.7	97	1.93E+04	100
025	0 bar, 50°C (cooled)	17.2	36	97.8	2.04E+04	99.6

Table 6.4: *Samples related to the experiments with increasing stress at high temperature*

Sample #	description	$f(R_1)$ μ	$f(R_1)$ σ	$g(R_2)$ μ	$g(R_2)$ σ	κ
026	0 bar, 200°C	16.8	37.8	97.4	2.63E+04	86.4
027	2 bar, 200°C	16.7	35.9	102	3.26E+04	100
028	4 bar, 200°C	16.7	39.7	105	2.62E+04	137
029	6 bar, 200°C	15.5	43	97.7	3.27E+04	124
–	sample broke when pressure was increased beyond 6 bar, second sample broke at 5.8 bar, further tests postponed.					

indicating that concerning the width, the effect of the strain must dominate over the (almost non-existent) effect of the temperature. Table 6.4 lists the relevant samples.

6.3.4 Increasing temperature at high stress

The effect of high temperature on a sample of Twaron 1000 under strain can be observed in Figure 6.9. A minor (but likely insignificant) change in orientation can be observed, but the most significant effect is a decrease in length of the scatterers, and a small reduction in width is also visible. The samples relevant to this experiment are listed in Table 6.5.

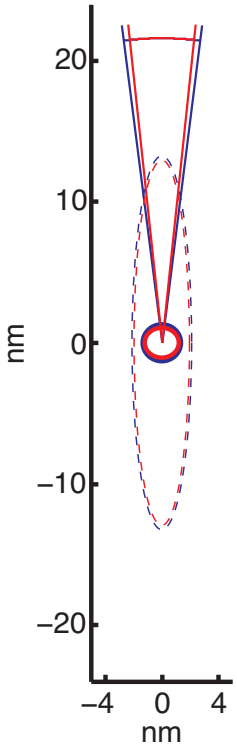

Figure 6.8: *The effect of 235N on a bundle of Twaron 1000 at 200° C (red) as compared to the initial unstressed sample (blue) at 200° C.*

Table 6.5: *Samples related to the experiments with increasing temperature at high stress*

Sample #	description	$f(R_1)$ μ	$f(R_1)$ σ	$g(R_2)$ μ	$g(R_2)$ σ	κ
037	6 bar, 50°C	16	38.2	117	2.69E+04	137
038	6 bar, 100°C	15.5	41.5	115	2.9E+04	137
039	6 bar, 150°C	15.2	42.6	110	3.31E+04	124
040	6 bar, 200°C	14.8	45.7	104	3.54E+04	124
041	6 bar, 50°C (cooled)	14.6	47.2	107	4.1E+04	124
042	0 bar, 50°C	15.1	48.4	108	3.4E+04	113

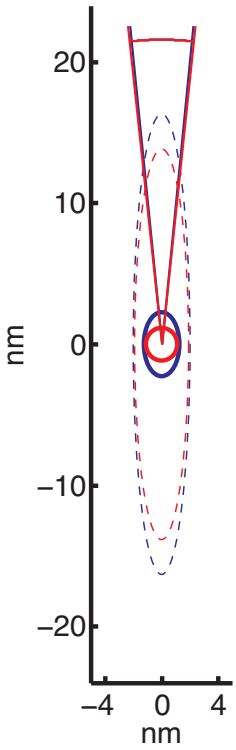

Figure 6.9: *The effect of 200° C on a bundle of Twaron 1000 under 235N of constant load (red) as compared to the initial sample (blue) at 50 ° C.*

6.3.5 Preliminary conclusions

From these four experiments, some initial conclusions may be drawn. The effect of stress on samples follows the expected behaviour for elastic scatterers. The voids elongate and their overall orientation increases. This could be related to the increase in crystalline orientation observed in wide angle diffraction by (amongst others) Ran et al. [2001].

The effect of temperature on the void structure is not very large at the temperatures that could be reached. The observed effect mainly indicates a reduction in length of the voids. This could be interpreted as a sintering effect on the ends of the voids (where the void is very narrow). This proposed structural effect appears to agree with the results obtained from the combined experiments. When the temperature is increased in samples which are under constant stress, elongated voids (and thus with longer narrow "tips") have their tips sintered close, reducing the length significantly. Increasing stess in samples under constant high temperature appears to immediately sinter the voids close that elongate due to the increased stress. However, other explanations are likely to describe this behaviour as well.

6.3.6 Other experiments and datapoints

Besides the measurements described above, many more measurements were obtained from which more information can be gleaned. Data fitting has already been performed on the samples, with the results given in Table E.1 for Twaron 1000, and E.2 for the as-spun Twaron samples. Described in Table 6.6 are the conditions under which the samples have been measured.

6.4 Final comments on these experiments

The initial results from these experiments show that the combined effect of elevated temperature and high stress can affect the internal nanostructure of PPTA fibres. The effect on the nanostructure is quite small, but more measurements at more extreme conditions (especially higher temperatures) may show a more severe impact and thus may shed more light on the behaviour under combined conditions. Faster measurement times and a better preparation could speed up the measurements significantly, which would allow for more rigourous exploration of the parameter space. For determination of the combined effects on the final struc-

Table 6.6: *Description of the remaining measurements*

Sample #	description
	Twaron 1000
	Increasing temperature at constant stress of 141N
043	4 bar, 50°C
044	4 bar, 100°C
045	4 bar, 150°C
046	4 bar, 200°C
047	4 bar, 50°C (return)
	Increasing temperature at constant stress of 47N
048	2 bar, 50°C
049	2 bar, 100°C
050	2 bar, 150°C
051	2 bar, 200°C
052	2 bar, 50°C (return)
	Increasing temperature at constant stress of 329N
053	8 bar, 50°C (broke after measurement when increasing to 100°C)
054–057	8 bar, 100-150-200-50°C but these samples are likely incorrect, fibre must have slipped in clamps
	AS Twaron
	Drying of AS Twaron
058–063	Ambient AS Twaron measured in 20 minute intervals
	Increasing pressure at room temperature
064	0 bar, 27°C, new sample of dried material
065	2 bar, 27°C
066	4 bar, 27°C
067	6 bar, 27°C, sample broke when increasing pressure to 8 bar.
	Increasing temperature at 235N
068	0 bar, 27°C, new sample
069	6 bar, 50°C
070	6 bar, 100°C
071	6 bar, 100°C (redo of 070, after a 1h beam dump)
072	6 bar, 200°C (sample broken, new fibre loaded)
	Increasing temperature without stress
073	0 bar, 50°C
074	0 bar, 200°C
075	0 bar, 50°C (cooled)

ture, it may be faster to have several samples prepared by the industry covering this parameter space, than using the tensile stage to obtain such samples.

Concerning the functioning of the analysis model and the sample stage, it has been shown that the analysis model is well suited for analysing the changes that occur in the nanostructure during this process. The statistical significance of the model has been shown to be adequate for the detection of these changes. The sample stage works well, the fibre clamps appear to be of the correct design, and the application of stress onto the sample using pneumatic pistons works well (although the system lacks flexibility in the dynamic range). The oven design could be significantly improved so that it better encloses the sample, and that it can reach higher temperatures.

Chapter 7

The Nanostructure in high-performance fibres

In order to test the validity of SAXS pattern analysis methods, 3D simulations have been constructed capable of simulating (scattering from) a structure of oriented, polydisperse ellipsoids. Additional 1D simulations have been set up for oriented systems to determine the effect of various phenomena on the scattering patterns. These include packing, polydispersity, graded boundaries and finite widths of the X-ray beam. Classical analyses have been shown to have only limited success in obtaining structurally relevant information on these simulated scattering patterns. Most notably, the invariant method and Debye-Bueche method were found to give satisfactory results. The invariant method to determine the degree of orientation was found to work but was limited by the finite aspect ratio of the particles. The Debye-Bueche method resulted in a length parameter which approximates the maximum likelihood estimator ("mode") of the size distribution of the simulated scatterers.

We have developed a novel analysis method that is able to quantify the polydispersity parameters of the nanoporous structure inside the filaments. Both length as well as width parameters can be extracted from this analysis, which achieves this by fitting the entire 2D anisotropic scattering pattern at once. The fitting model has been tested against scattering patterns from simulated nanostructures as well as experimentally obtained scattering patterns. Using adaptations of this general model, structural variations in different types of Twaron can be determined and quantitatively described.

Another interesting investigation is the investigation into the nanostructural behaviour of these crystalline polymers under axially compressive and tensile strain.

For this purpose, a single filament was put in a loop. The top of the loop (where the radius of curvature is smallest, and thus the imposed strain the highest) was then probed using microbeam SAXS at the SLS. SAXS data was extracted from the compressive as well as tensile region of the bent section. From the analysis of these unique results, it is concluded that upon bending, a regular strain (gradient) relief mechanism brings about a periodic occurrence of buckled fibrils (compression) and/or slip planes. This effect, only visible for as-spun (i.e. not heat-treated) Twaron, has been shown to be dependent on the amount of strain in the filament.

Investigations in the behaviour of the nanostructure under tensile stress and elevated temperatures showed a small but statistically significant effect of these two parameters on the nanostructure. The combination of the two parameters affected the structure differently, depending on whether the stress was increased at elevated temperatures or when the temperature was increased at high stress levels.

Chapter 8

Acknowledgments

I hereby thank my supervisors, Martin Vigild, Kell Mortensen, Enno Klop and Jens Wenzel Andreasen, who made an excellent support team. Each could look upon the topic from their own viewpoint, which often ensued into wonderful discussions at meetings, as energetic supervisors each fought to convey their ideas on the topic at hand. I also thank Dag Breiby and Oliver Bunk for their assistance during and after the looped filament experiments at the SLS.

I would also like to thank Thomas Hansen and Nicole MacDonald at the DTU Center for Electron Nanoscopy for their excellent efforts in obtaining successful electron microscopy images, and the people at the DTU KT workshop, who have produced various complex sample stages for me on a tight deadline. Without an internal workshop, the sample stages would likely not have been realised. I furthermore thank Jörg Vogel at DTU Nanotech for his work on the laser embossing of the microchannel device, and Søren Kynde for his help with translating the thesis summary into Danish.

Furthermore, I would much like to acknowledge the people at the Teijin Aramid BV for their interest and continued supporting effort and interesting topics, and my colleagues at DTU, Risø , KU and Karsten Joensen from JJ X-ray for their discussions. I would also like to thank Stephanie Ropenus and Peter Anderson for their help in maintaining a relaxed attitude towards the PhD process. This was also helped by a daily dose of online comics. Especially the Ph.D. comics (by Jorge Cham) have sometimes proven eerily familiar.

Last and foremost, I would like to thank my family for their support and Fenny Sanyoto, my wife, who has made this endeavour possible by being excited to move to new places and to provide me food and comfort in times of need.

Chapter 9

Bibliography

Aerts, J. (1991). Small-angle x-ray scattering of aramid fibre. *Journal of Applied Crystallography*, 24:709–711.

Afshari, M., Sikkema, D. J., Lee, K., and Bogle, M. (2008). High performance fibers based on rigid and flexible polymers. *Polymer Reviews*, 48(2):230–274.

Als-Nielsen, J. and McMorrow, D. (2004). *Elements of modern X-ray physics*. John Wiley & sons, 2 edition.

Andrews, M. C., Lu, D., and Young, R. J. (1997). Compressive properties of aramid fibres. *Polymer*, 38:2379–2388.

Beyen, A. (2007). *Specters, smart fellows and strategists*. Allmedia.

Bresenham, J. E. (1965). Algorithm for computer control of a digital plotter. *IBM Systems Journal*, 4:25–30.

Chae, H. G. and Kumar, S. (2006). Rigid-rod polymeric fibers. *Journal of Applied Polymer Science*, 100(1):791–802.

Ciccariello, S. and Riello, P. (2007). Small-angle scattering from three-phase samples: application to coal undergoing an extraction process. *Journal of Applied Crystallography*, 40(2):282—–289. Three-phase samples.

Davies, R., Burghammer, M., and Riekel, C. (2006). Simultaneous microfocus raman and microfocus xrd: Probing the deformation of a single high-performance fiber. *Macromolecules*, 39(14):4834–4840.

Davies, R. J., Burghammer, M., and Riekel, C. (2007). Probing the internal structure of high-performance fibers by on-axis scanning diffractometry. *Macromolecules*, 40(14):5038–5046.

Davies, R. J., Koenig, C., Burghammer, M., and Riekel, C. (2008). On-axis microbeam wide- and small-angle scattering experiments of a sectioned poly(p-phenylene terephthalamide) fiber. *Applied Physics Letters*, 92(10):101903.

Davis, H., Singletary, J., Srinivasarao, M., Knoff, W., and Ramasubramanian, M. (2000). Microstructure organization in para-aramid fibers. *Textile Research Journal*, 70(11):945–950.

Debye, P. and Bueche, A. M. (1949). Scattering by an inhomogeneous solid. *Journal of Applied Physics*, 20:518–525.

Diez, B. and Sobry, R. (1993). Oscillating and non-oscillating contributions in the porod law. *Journal de Physique IV*, 3:511–513.

Dobb, M. G., Johnson, D. J., Majeed, A., and Saville, B. P. (1979). Microvoids in aramid-type fibrous polymers. *Polymer*, 20:1284–1288.

Dobb, M. G., Johnson, D. J., and Saville, B. P. (1977). Direct observation of structure in high-modulus aromatic fibers. *Journal of Polymer Science: Polymer Symposium*, 58:237–251.

Dobb, M. G., Johnson, D. J., and Saville, B. P. (1981). Compressional behaviour of kevlar fibres. *Polymer*, 22:960–965.

Dobb, M. G. and Robson, R. M. (1990). Structural characteristics of aramid fibre variants. *Journal of Materials Science*, 25:459–464.

Dreiss, C. A., Jack, K. S., and Parker, A. P. (2006). On the absolute calibration of bench-top small-angle x-ray scattering instruments: a comparison of different standard methods. *Journal of Applied Crystallography*, 39:32—-38.

Effler, L. J. and Fellers, J. F. (1992). Structural orientation functions for anisotropic small-angle scattering. *Journal of Physics D: Applied Physics*, 22:74–78.

Eikenberry, E. F., Brönnimann, C., Hülsen, G., Toyokawa, H., Horisberger, R., Schmitt, B., Schulze-Briese, C., and Tomizaki, T. (2003). Pilatus: a two-dimensional x-ray detector for macromolecular crystallography. *Nucl Instrum Meth A*, 501(1):260–266.

Fidan, S., Palazotto, A., Tsai, C. T., and Kumar, S. (1993). Compressive properties of high-performance polymeric fibers. *Composites Science and Technology*, 49(3):291–297.

Freund, A. (1993). *Neutron and synchrotron radiation for condensed matter stud-*

ies, volume 1, chapter Chapter III- X-ray optics for synchrotron radiation, pages 79–93. EDP Sciences - Springer-Verlag.

Gaymans, R. J., Tijssen, J., Harkema, S., and Bantjes, A. (1976). Elastic modulus in the crystalline region of poly(p-phenylene terephthalamide). *Polymer*, 17:517–518.

Glatter, O. and Kratky, O. (1982). *Small angle X-Ray Scattering*. Academic Press.

Graafsma, H. (2009). X-ray detectors. Lecture at the Nordforsk Summerschool, 2009.

Greenwood, J. H. and Rose, P. G. (1974). Compressive behaviour of kevlar 49 fibres and composites. *Journal of Materials Science*, 9(11):1809–1814.

Grubb, D. T., Prasad, K., and Adams, W. W. (1991). Small-angle x-ray diffraction of kevlar using synchrotron radiation. *Polymer*, 32(7):1167–1172.

Haraguchi, K., Kajiyama, T., and Takayanagi, M. (1979a). Effect of coagulation conditions on crystal modification of poly(para-phenylene terephthalamide). *Journal of Applied Polymer Science*, 23(3):915–926.

Haraguchi, K., Kajiyama, T., and Takayanagi, M. (1979b). Uniplanar orientation of poly(para-phenylene terephthalamide) crystal in thin-film and its effect on mechanical-properties. *Journal of Applied Polymer Science*, 23(3):903–914.

Helfer, E., Panine, P., Carlier, M.-F., and Davidson, P. (2005). The interplay between viscoelastic and thermodynamic properties determines the birefringence of f-actin gels. *Biophysical Journal*, 89(1):543–53.

Hermans, P. H., Heikens, D., and Weidinger, A. (1959). A quantitative investigation on the x-ray small angle scattering of cellulose fibers. Part II. The scattering power of various cellulose fibers. *Journal of Polymer Science*, 35:145–165.

Horio, M., Kaneda, T., Ishikawa, S., and Shimamura, K. (1984). Morphology of fibers made from polymer liquid crystals. *Sen'i Gakkaishi*, 40(8):285–290.

Jackson, C. and Chanzy, H. (1993). Morphology and structure of poly (p-phenylene terephthalamide) crystallized from dilute organic solution. *POLYMER-LONDON-*, 34:5011–5011.

Jackson, C. L., Schadt, R. J., Gardner, K. H., Chase, D. B., Allen, S. R., Gabara, V., and English, A. D. (1994). Dynamic structure and aqueous accessibility of poly(p-phenylene terephthalamide) crystallites. *Polymer*, 35(6):1123–1131.

Jain, A. and Vijayan, K. (2004). Forbidden reflections from the aramid ppta - a novel correlation with stacking faults. *Bulletin of Materials Science*, 27(1):47–50.

Jiang, H., Adams, W. W., and Eby, R. K. (1993). *High Performance Polymer Fibres: material science and technology (a comprehensive treatment)*, volume 12, chapter 13. VCH.

Jungnickel, B. J. (1977). Method for the quantitative characterization of the supermolecular structure of highly oriented polymers. *Journal of Polymer Science: Polymer Symposium*, 58:275—281.

Kenig, S. (1987). Orientability of liquid-crystal polymers in elongational flow. *Polymer Engineering and Science*, 27(12):887–892.

Klop, E. A. (2001). The investigation of the microstructure of aramid fibres using small-angle x-ray scattering. Teijin Aramid internal report.

Klop, E. A. (2009). unpublished. Private communication.

Koberstein, J. T., Morra, B., and Stein, R. S. (1980). The determination of diffuse boundary thicknesses of polymers by small-angle x-ray scattering. *Journal of Applied Crystallography*, 13:34–45.

Krause, S. J., Vezie, D. L., and Adams, W. W. (1989). Straightening of pleated sheet structure in fibers of poly(para-phenyleneterephthalamide) - kevlar 149. *Polymer Communications*, 30:10–13.

Li, L.-S., Allard, L. F., and Bigelow, W. C. (1983). On the morphology of aromatic polyamide fibres (kevlar, kevlar-49, and prd-49). *Journal of Macromolecular Science, Part B*, 22:269–290.

Liu, J., Cheng, S., and Geil, P. (1996). Morphology and crystal structure in single crystals of poly(p-phenylene terephthalamide) prepared by melt polymerization. *Polymer*, 37(8):1413–1430.

Livet, F. (2007). Diffraction with a coherent x-ray beam: dynamics and imaging. *Acta Crystallographica Section A: Foundations of Crystallography*, 63(Pt 2):87–107.

Loidl, D., Paris, O., Burghammer, M., Riekel, C., and Peterlik, H. (2005). Direct observation of nanocrystallite buckling in carbon fibers under bending load. *Physical review letters*, 95:225501–1–225501–4.

Mooney, D. A. and MacElroy, J. M. D. (2004). Differential water sorption studies on kevlar 49 and as-polymerised poly(p-phenylene terephthalamide): adsorption adn desorption isotherms. *Chemical Engineering Science*, 59:2159—2170.

Morgan, R., Pruneda, C., and Steele, W. (1983). The relationship between the physical structure and the microscopic deformation and failure processes of poly

(p-phenylene terephthalamide) fibers. *Journal of Polymer Science: Polymer Physics Edition*, 21(9).

Morse, J. (1993). *Neutron and synchrotron radiation for condensed matter studies*, volume 1, chapter Chapter IV- Detectors for synchrotron radiation, pages 95–112. EDP Sciences - Springer-Verlag.

Né, F., Gabriel, A., Kocsis, M., and Zemb, T. (1997). Smearing effects introduced by the response function of position-sensitive gas detectors in saxs experiments. *Journal of Applied Crystallography*, 30:306–311.

Northolt, M. G. (1974). X-ray-diffraction study of poly(p-phenylene terephthalamide) fibers. *European Polymer Journal*, 10(9):799–804.

Northolt, M. G. and Aartsen, J. J. v. (1973). On the crystal and molecular structure of poly-(p-phenylene terephthalamide). *Journal of Polymer Science: Polymer Letters Edition*, 11:333–337.

Northolt, M. G. and Sikkema, D. J. (1991). Lyotropic main chain liquid crystal polymers. *Advances in polymer science*, 98:119–172.

Northolt, M. G. and Stuut, H. A. (1978). Determination of crystal density of polymers by x-ray-diffraction. *Journal of Polymer Science: Polymer Physics*, 16(5):939–943.

Oster, G. and Riley, D. P. (1952). Scattering from cylindrically symmetric systems. *Acta Crystallographica*, 5:272–276.

Panar, M., Avakian, P., Blume, R. C., Gardner, K. H., Gierke, T. D., and Yang, H. H. (1983). Morphology of poly(para-phenylene terephthalamide) fibers. *Journal of Polymer Science: Polymer Physics Edition*, 21(10):1955–1969.

Panar, M. and Beste, L. F. (1977). Structure of poly(1,4-benzamide) solutions. *Macromolecules*, 10(6):1401–1406.

Pauw, B. R., Vigild, M. E., Mortensen, K., Andreasen, J. W., Klop, E. A., Breiby, D. W., and Bunk, O. (2009). Strain-induced internal fibrillation in looped aramid filaments. Submitted.

Pedersen, J. S. (1997). Analysis of small-angle scattering data from colloids and polymer solutions: modeling and least-squares fitting. *Advances in Colloid and Interface Science*, 70:171–210.

Pedersen, J. S. (2004). A flux- and background-optimized version of the NanoSTAR small-angle x-ray scattering camera for solution scattering. *Journal of Applied Crystallography*, 37:369–380.

Perret, R. and Ruland, W. (1969). Single and multiple x-ray small-angle scattering of carbon fibers. *Journal of Applied Crystallography*, 2:209–218.

Picken, S. J. (1990). Orientational order in aramid solutions determined by diamagnetic susceptibility and birefringence measurements. *Macromolecules*, 23(2):464–470.

Picken, S. J., Aerts, J., Doppert, H. L., Reuvers, A. J., and Northolt, M. G. (1991). Structure and rheology of aramid solutions - transient rheological and rheooptical measurements. *Macromolecules*, 24(6):1366–1375.

Picken, S. J., Aerts, J., Visser, R., and Northolt, M. G. (1990). Structure and rheology of aramid solutions - x-ray-scattering measurements. *Macromolecules*, 23(16):3849–3854.

Picken, S. J., Zwaag, S. v. d., and Northolt, M. G. (1992). Molecular and macroscopic orientational order in aramid solutions - a model to explain the influence of some spinning parameters on the modulus of aramid yarns. *Polymer*, 33(14):2998–3006.

Plazanet, M., Fontaine-Vive, F., Gardner, K. H., Forsyth, V. T., Ivanov, A., Ramirez-Cuesta, A. J., and Johnson, M. R. (2005). Neutron vibrational spectroscopy gives new insights into the structure of poly(p-phenylene terephthalamide). *Journal of the American Chemical Society*, 127:6672–6678.

Ran, s., Fang, D., Zong, X., Hsiao, B. S., Chu, B., and Cunniff, P. M. (2001). Structural changes during deformation of Kevlar fibers via on-line synchrotron SAXS/WAXSD techniques. *Polymer*, 42:1601–1612.

Rao, Y., Waddon, A. J., and Farris, R. J. (2001). Structure-property relation in poly(p-phenylene terephthalamide) (ppta) fibers. *Polymer*, 42:5937–5946.

Riekel, C., Dieing, T., Engström, P., Vincze, L., Martin, C., and Mahendrasingam, A. (1999). X-ray microdiffraction study of chain orientation in poly(p-phenylene terephthalamide). *Macromolecules*, 32:7859—7865.

Riekel, C. and Vollrath, F. (2001). Spider silk fibre extrusion: combined wide- and small-angle x-ray microdiffraction experiments. *International Journal of Biological Macromolecules*, 29:203–210.

Roche, E. J., Wolfe, M. S., Suna, A., and Avakian, P. (1985). Light-diffraction effects from kevlar aramid fibers. *Journal of Macromolecular Science and Physics*, B24(1-4):141–157.

Ruland, W. (1971). Small-angle scattering of two-phase systems: determination

and significance of systematic deviations from Porod's law. *Journal of Applied Crystallography*, 4:70–73.

Ruland, W. (1978). The evaluation of the small-angle scattering of anisotropic lamellar two-phase systems by means of interface distribution functions. *Colloid and Polymer Science*, 256:932–936.

Ruland, W. (1990). Carbon fibers. *Advanced Materials*, 2(11):528—-536.

S., C. (1993). Edge contributions to the kirste-porod formula: the spherical segment case. *Acta Crystallographica*, A49:750–755.

Saijo, K., Arimoto, O., Hashimoto, T., Fukuda, M., and Kawai, H. (1994). Moisture sorption mechanism of aromatic polyamide fibres: diffusion of moisture into regular kevlar as observed by small-angle x-ray scattering technique. *Polymer*, 35:496–503.

Sartirana, M. L., Marsano, E., Bianchi, E., and Ciferri, A. (1986). Order parameter in polymer liquid-crystals .1. poly(para-benzamide) in n,n-dimethylacetamide lithium-chloride. *Macromolecules*, 19(4):1176–1180.

Sawyer, L. C., Chen, R. T., Jamieson, M. G., Musselman, I. H., and Russell, P. E. (1993). The fibrillar hierarchy in liquid crystalline polymers. *Journal of Materials Science*, 28:225–238.

Schmidt-Rohr, K. (2007). Simulation of small-angle scattering curves by numerical fourier transformation. *Journal of Applied Crystallography*, 40:16–25.

Singletary, J., Davis, H., Song, Y., Ramasubramanian, M. K., and Knoff, W. (2000). The transverse compression of ppta fibers part ii fiber transverse structure. *Journal of Materials Science*, 35:583—592.

Smith, A. and Ade, H. (1996). Quantitative orientational analysis of a polymeric material (kevlar(r) fibers) with x-ray microspectroscopy. *Applied Physics Letters*, 69(25):3833–3835.

Stewart, D. (2009). A platform with six degrees of freedom (reprinted from vol 180, 1965). *Proceedings of the Institution of Mechanical Engineers Part C - Journal of Mechanical Engineering Science*, 223:266–273.

Stribeck, N. (2001). Extraction of domain structure information from small-angle scattering patterns of bulk materials. *Journal of Applied Crystallography*, 34:496–503.

Stribeck, N. (2007). *X-Ray Scattering of Soft Matter*. Springer-Verlag Berlin Heidelberg.

Stribeck, N., Buzdugan, E., Ghioca, P., Serban, S., and Gehrke, R. (2002). Nanostructure evolution of sis thermoplastic elastomers during straining as revealed by usaxs and two-dimensional chord distribution analysis. *Macromolecular Chemistry and Physics*, 203:636–644.

Tang, M.-Y., Rice, G., Fellers, J., and Lin, J. (1986). X-ray scattering studies of graphite fibers. *Journal of Applied Physics*, 60(2):803–810.

Tanner, D., Fitzgerald, J., and Phillips, B. (1989). The kevlar story - an advanced materials case-study. *Angewandte Chemie International Edition*, 28(5):649–654.

Veen, F. v. d. and Pfeiffer, F. (2004). Coherent x-ray scattering. *Journal of Physics- Condensed matter*, 16:5003–5030.

Vonk, C. G. (1973). Investigation of non-ideal two-phase polymer structures by small-angle x-ray scattering. *Journal of Applied Crystallography*, 6(2):81—-86.

Wang, W., Ruland, W., and Cohen, Y. (1993). Fibrillar and microfibrillar structures in poly(p-phenylene teraphtalamide) fibers. *Acta Polymer*, 44:273–278.

Weisstein, E. W. (2005). "log normal distribution" from mathworld–a wolfram web resource.

Weisstein, E. W. (2007). "line-line distance." from mathworld–a wolfram web resource.

Weisstein, E. W. (2008). "superellipse." from mathworld–a wolfram web resource.

Weisstein, E. W. (2009). "von mises distribution" from mathworld–a wolfram web resource.

Weyland, H. G. (1980). The effect of anisotropy in wet spinning poly(p-phenyleneterephthalamide). *Polymer Bulletin*, 3(6-7):331–337.

Yabuki, K., Ito, H., and Oota, T. (1976). Consideration on the relation between fine structure and mechanical property of poly(p-phenylene terephthalamide) fibres. *Sen-I Gakkaishi*, 32:T55—T61.

Yabuki, K., Ito, H., and Ota, T. (1975). Studies on the fine structure of poly(p-phenylene terephthalamide) fibres. *Sen-I Gakkaishi*, 31:T524—T530.

Zhang, F., Ilavsky, J., Long, G. G., Quintana, J. P. G., Allen, A. J., and Jemian, P. R. (2009). Glassy carbon as an absolute intensity calibration standard for small-angle scattering. *Metallurgical and Materials Transactions A*.

Zhang, H., Zhang, J., Chen, J., Hao, X., Wang, S., Feng, X., and Guo, Y. (2006).

Effects of solar uv irradiation on the tensile properties and structure of ppta fiber. *Polymer Degradation and Stability*, 91(11):2761–2767.

Appendix A

Interference in two special cases

(Addendum to derivation in paragraph 2.2.1)

To calculate the position of constructive and destructive interference for two point scatterers, it can be shown that this is dependent on the relative locations in 3D space of the two scattering centers, using two special, easy to calculate cases. The first case is where the scattering centres (a and b) are positioned just so, that half of the pathlength difference ΔL lies on either side of scatterer a (known as "diffraction condition", shown in Figure A.1). If we assume that we would like to know the scattering at an angle of 2Θ, we can show that the pathlength difference between the two diffracted rays ΔL is dependent on Θ and vector $\mathbf{r}$ (connecting a and b) through:

$$\Delta L = 2\frac{\sin\theta}{\mid \mathbf{r} \mid} \tag{A.1}$$

Interference maxima can then be found at Θ where $\Delta L = n\lambda$ where λ denotes the wavelength, and n is an integer. Minima are found for cases where $\Delta L = n\lambda - \frac{1}{2}\lambda = (n - \frac{1}{2})\lambda$. If we measure our diffraction pattern in (wavelength independent) q-space, where $q = \frac{4\pi}{\lambda}\sin\Theta$, we get maxima when $2\pi n = \mid \mathbf{r} \mid q$ and minima when $2\pi(n - \frac{1}{2}) = \mid \mathbf{r} \mid q$. We thus conclude, that for this case the interference is dependent on the distance between the scatterers alone.

The second hypothetical case is where the scatterers are related through vector r which is now perpendicular to the incoming radiation (cf. Figure A.2. For this system, we can derive relationships similar as above, resulting in:

$$\Delta L = \frac{\sin 2\theta}{\mid \mathbf{r} \mid} \tag{A.2}$$

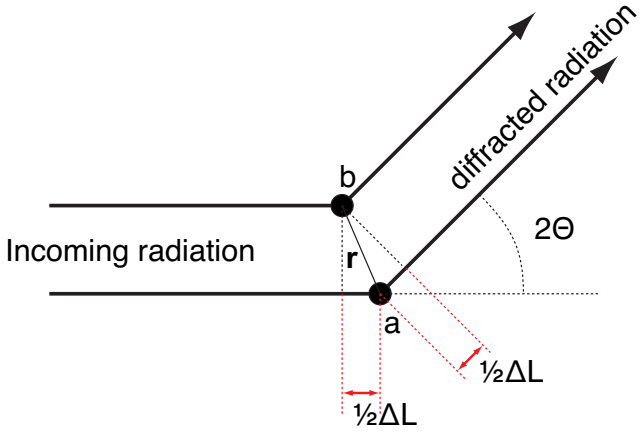

Figure A.1: *Two electrons in "diffraction condition", oscillating with an incoming EM wave and emitting interfering waves themselves.*

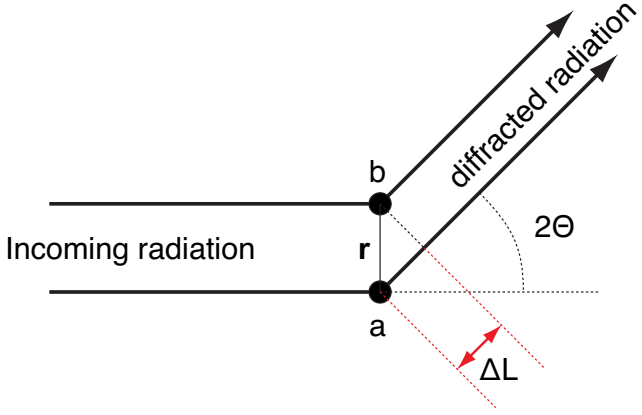

Figure A.2: *Two electrons positioned parallel to the wavefront of the incoming radiation, oscillating with an incoming EM wave and emitting interfering waves themselves.*

Which at first glance looks very similar to equation A.1, but is irreconcilable with it. This is proof that diffraction is dependent not only on the length of vector r, but also on its direction for arbitrary directions of r.

Appendix B

Software

For this project, a large amount of software was written in Matlab. Herewith a short description of some of the more useful programs. Many of the programs written never left development stage, or were immediately superseded by another function. Those "orphaned" programs will not be mentioned here as they were clearly of little use.

B.1 "educational" software

B.1.1 Software group description

This software group consists of programs that were written in order to obtain a better understanding of scattering of various systems. Most of this software has a rudimentary graphical user interface.

B.1.2 EDsel-programs

The programs starting with "EDsel" are programs for 1D superellipsoid simulation. They were written at the end of the project to get a better understanding of the origins of the scattering patterns obtained at the SLS. This package has the capability to simulate scatterers with an aligned superellipsoidal cross-section and included optional periodicity (through Fourier transforms), graded boundaries, detector point spread functions and beam width simulation. Version 5 of this command-line simulation program included the option of packed polydisperse

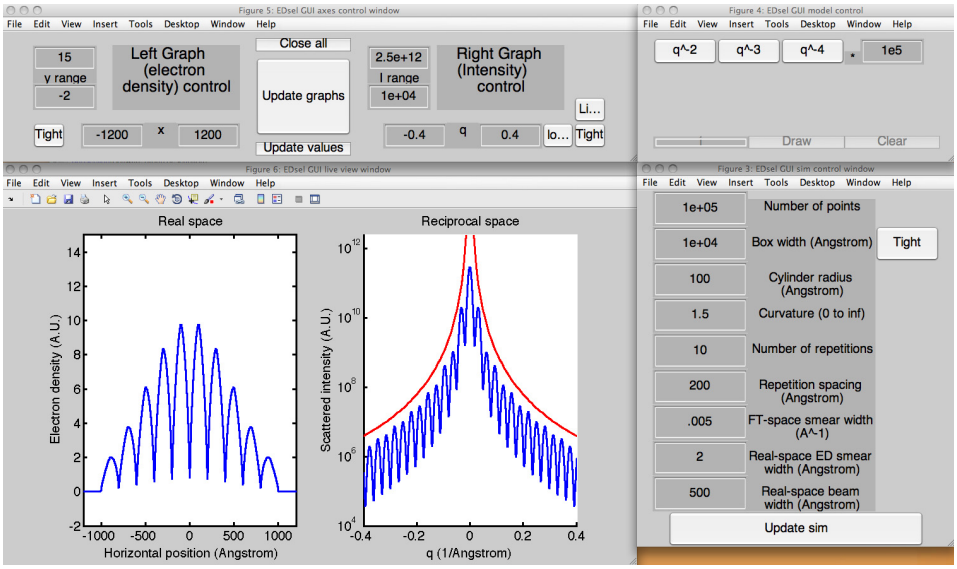

Figure B.1: *EDsel_gui_v2 interface.*

scattering profiles. There is a graphical user interface EDsel_gui_v2 (Figure B.1) which works with version 4 of the command-line program.

B.1.3 selscat-programs

The "selscat" programs can calculate the scattering patterns of projected 3D (aligned) superellipsoid-of-revolution shapes (lathe-like objects with a superellipsoidal cross-section). They were made during the project in an attempt to understand the scattering from the nanostructure in the fibres a little better. The intention was to use this simulation to test analytical approximations for a superellipsoid form factor function, which was never made. A numerical fitting function for fitting polydisperse superellipsoidal shapes to 2D scattering patterns of fibres was made, but remains untested. Its rudimentary GUI is shown in Figure B.2.

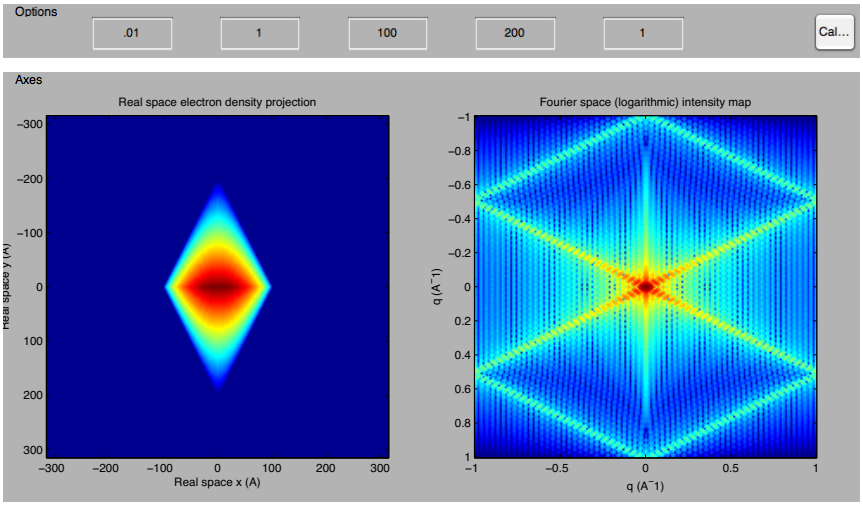

Figure B.2: *selscatgui interface.*

B.2 SAXSGUI data analysis

B.2.1 Software group description

The SAXSGUI is a software package that is intended for the analysis of (integrated or non-integrated) 2D scattering patterns and has been developed by dr. K. Joensen of JJ X-Ray Systems A/S in collaboration with Rigaku and several individual contributors. While there are still a few rough edges, it is being used more and more as a tool for quickly exploring 2D scattering patterns. Some aspects of its GUI are shown in Figure B.3.

B.2.2 2D fitting, with optional resolution function

Considerable work was done on the 2D fitting routine. While the graphical user interface was built by dr. K. Joensen, some under-the-hood improvements and additions were done by me, such as the implementation of binning and speeding up of the iteration procedure. A resolution function was added as well, so that instrumental smearing can be applied to the model. A final adaptation needs to be done to that before it is useful, however. This adaptation involves taking out the real-space smearing routine and replacing it for a (considerably faster) Fourier-

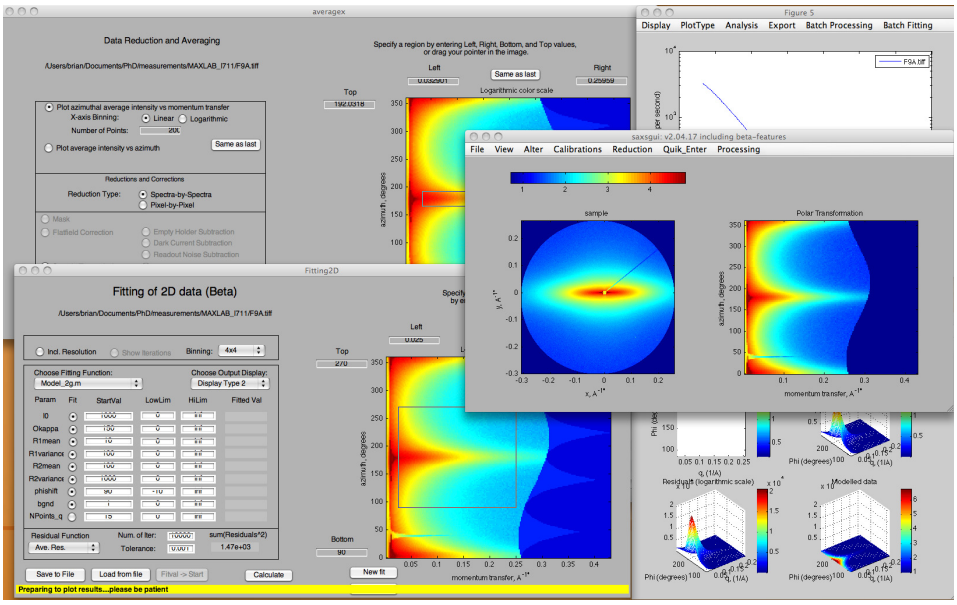

Figure B.3: *The SAXSGUI interface.*

space smearing routine. This may speed up the resolution function implementation enough to make it run at a bearable speed. An additional improvement would be the inclusion (or display) of the weighting of the fitting parameters as determined by the fitting algorithm (fminsearchbnd). All in all, this 2D fitting implementation has been used for most of the fits presented here, as it can do automated reporting and can be called automatically from the front-end database which is discussed next.

B.2.3 A front-end database

In order to automate the process of calibration and fitting, a front-end database was made to work with the SAXSGUI (Figure B.4). This database shows a thumbnail image of the scattering pattern, and stores this together with information on calibrations and corrections in a database. This database is saved every time a change is made, so that no manual saves are required. The information on calibrations and other relevant information is transferred to the SAXSGUI when the thumbnail is pressed, and the saxsgui is opened. It also has the capability of running automated data fitting using the 2D fitting routine, so that many samples can be fit sequentially.

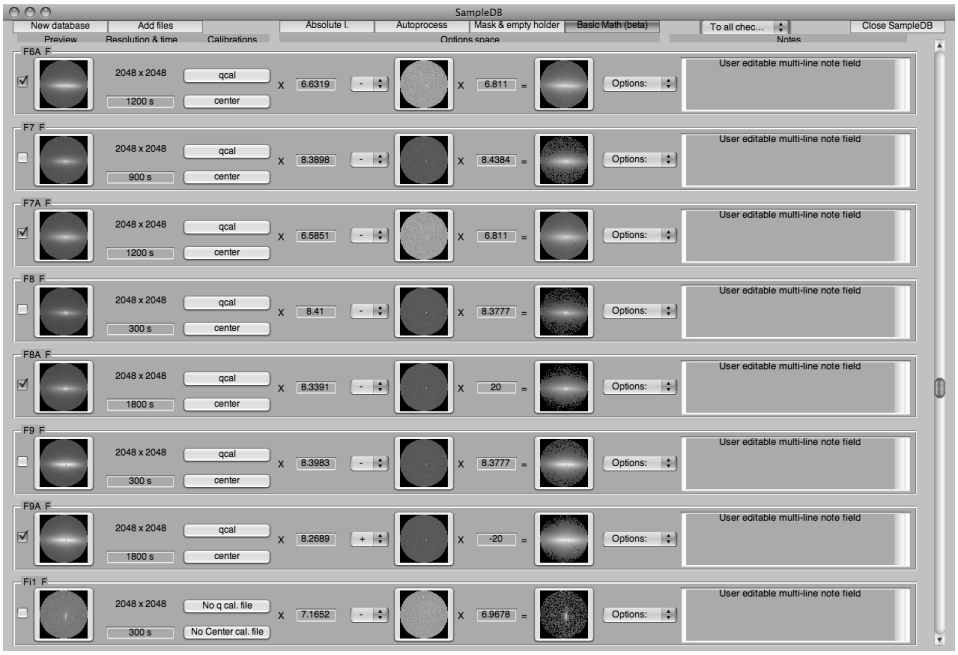

Figure B.4: *The sampledb interface.*

While the database (version 2.3) has proven itself to be a useful tool for this project, it should probably be rewritten from the bottom up. That is because the database can be made a lot simpler and faster if all the corrections and calibrations for these samples are done at collection time. A program has been written in the BW4-set (described on page 179) to generate corrected and calibrated files, containing all of the required information. This can then be read by the database, whose only purpose it is then to manage the corrected files. A proof-of-concept version (version 2.4) has been written which shows that it is indeed useful to have pre-corrected files. The database program can then be modified to give the user the option of applying the calibration, to change the calibration parameters if necessary, and to automatically perform fits on selected samples.

B.3 Other data processing software

B.3.1 Software group description

Some other data processing software was written which do not have a graphical user interface. These were written for (pre-)processing beamline-specific data and for applying classical fits to the data (the Maxlab-programs).

B.3.2 Maxlab-programs

The "maxlab_1D" program is the main program in this set, doing the majority of the computations. Its input consists of (at minimum) three structured arrays, describing the SAXS geometry, radiation and detection parameters (in the "config" structured array), the sample-specific information such as beam intensity and background correction information ("sampleconfig"), and the fitting set-up and parameters ("fitconfig"). This then is capable of running a Porod, (double-)Debye-Bueche, "Streak" and some other analyses on 1D data extracted from the 2D recording using 1-degree pie binning. Its output can be visualised in a report that can be generated by "maxlab_1D_PDcombine".

B.3.3 SLS-programs

The SLS programs are a set of programs designed to deal with the large quantity of data obtained from the SLS (over 700 GB of data was collected in 5 days!). "sls1Dmacro_v3" was made to do the orientation determination and the bresenham line extraction on a single measurement, writing the resulting I, q-data as an ASCII-file. The first row of this file lists also the information on the exact extraction angle in degrees, and the sum of intensity on this line. The program "sls1Dmacromacro_v2" was made to run the extraction on entire measurement sets (directories) at once. This function also outputs a matlab datafile containing the intensity and rotation maps of the samples.

The "slsfit"-programs could then fit the 1D data, and a game-like interface was built to handle the fitting of the many 1D curves (named "slsfit1Dmacro"). This interface could be used to check the fit and adjust the starting parameters where necessary using keypresses. Another important (but simple) program is "slsgetsetsize", which contains the information on real-space mesh scan size and number of points for each directory.

B.3.4 BW4-programs

The BW4-prorgams consist of a conbination of "BW4combine", which can be used to calibrate and correct the images obtained at BW4. It stores a center and (geometric) q-calibration in the file, and corrects for background, transmission and primary beam intensity. The produced file has the extension .arb, which stands for "arbitrary intensity". The alternative would be .abs for "absolute intensity"-calibrated files. These files can be read by "sampledb2_4", which uses a routine named "arb2saxs" to make the files suitable for reading with the SAXSGUI.

This program set allowed for on-site correction and fitting of the data at BW4, leaving only the interpretation of the results to be done after the beamtime was over. Thus, immediate feedback was obtained on the measurements, and a better decision on which remaining samples to measure could therefore be made on the spot.

The "BW4combine" program has a nice feature in that the input is given in parameter/value pairs. This means that any amount of information can be supplied in any order (the program will complain if not enough information is supplied to make the background correction or the q-calibration).

B.4 fitting functions

B.4.1 Software group description

These fitting functions were fitting models used in minimisation routines to try and find the best fit to a 2D scattering pattern. While many were written, only the more useful variants will be mentioned here.

B.4.2 1D fitting functions

1D fitting functions used are described in Table B.1.

Table B.1: *1D fitting functions*

Fitting function name	Description
	SAXSGUI fitting functions
Bessel_cyl	Single, isolated cylinder analytical scattering function
DoubleDebye	Two Debye-Bueche functions for obtaining correlation lengths from systems with bimodal distributions
TrueDoubleDebye	A Debye-Bueche function with a Guinier function for describing scattering from a distinctly separate set of scatterers
USF	The "Universal scattering function" as defined by Beaucage, combining a Guinier function with a Porod scattering function
	Maxlab_1D fitting functions
USF	The "Universal scattering function" as defined by Beaucage, combining a Guinier function with a Porod scattering function
Debye_1D	The Debye-Bueche scattering function
DoubleDebye	Two Debye-Bueche functions for obtaining correlation lengths from systems with bimodal distributions
Porod_1D	The Porod scattering function

B.4.3 2D fitting functions

The 2D fitting functions described in Chapter 4 Consist of two separate functions. One function handles the grid interpolation and implentation of the rotational smearing. These functions all start with "Model_2" and have a letter behind them to indicate their version. The version that has been used here is "Model_2g". It calls Model_1k_ell_noOD.m to compute the scattering pattern of perfectly aligned, polydisperse ellipsoidal scatterers over a limited number of q and ψ values.

Appendix C

Measuring in absolute units.

Absolute intensity measurements will provide the volume of the scatterers in the irradiated sample volume, allowing the estimation of the void fraction in the sample. The method involves a rescaling of the scattering plot to absolute units. Dreiss et al. [2006] have written a concise derivation of this method (a good review of the use of glassy carbon as a calibration standard is also available Zhang et al. [2009]). The intensity ($I_s(q)$) scattered from a sample in photons (N_s) per angular section ($\Delta\Omega$) per unit time (t_s) is defined as:

$$I_s(q) = \frac{N_s}{t_s} = I_0(\lambda) A \Delta\Omega \eta(\lambda) T_s(\lambda) d_s \left(\frac{\mathrm{d}\Sigma}{\mathrm{d}\Omega}\right)_s (q) + I_{B,s}(q) \tag{C.1}$$

where $I_0(\lambda)$ is the incident flux in photons $\mathrm{s}^{-}1\ \mathrm{cm}^{-2}$, A is the area illuminated by the beam, $\Delta\Omega$ is the solid angle element defined by the size of a detector pixel, η is the (wavelength dependent) detector efficiency, $T_s(\lambda)$ is the wavelength dependent sample transmission factor, d_s the thickness of the sample, $I_{B,s}(q)$ the background scattering instensity, and $\left(\frac{\mathrm{d}\Sigma}{\mathrm{d}\Omega}\right)_s (q)$ is the differential scattering cross section in cm^{-1}.

Dividing the intensity of a standard with a known differential scattering cross section, by the aforementioned intensity of the sample, we obtain the differential cross section of the sample:

$$\left(\frac{\mathrm{d}\Sigma}{\mathrm{d}\Omega}\right)_s (q) = \left(\frac{\mathrm{d}\Sigma}{\mathrm{d}\Omega}\right)_{st} (q) \frac{[I_s(q) - I_{B,s}]}{d_s T_s} \frac{d_{st} T_{st}}{[I_{st}(q) - I_{B,st}]} \tag{C.2}$$

Where the subscript $_{st}$ defines the measurements on the standard. The transmission factor in the case where capillaries are used, is the transmission of the sample *and* the capillary, and the standard *and* the capillary.

Thus, for each measurement on the standard, a machine- and time-dependent (but not sample-dependent) calibration factor (C) is derived:

$$C = \left(\frac{\mathrm{d}\Sigma}{\mathrm{d}\Omega}\right)_{st}(q)\frac{d_{st}T_{st}}{[I_{st}(q) - I_{B,st}]} \tag{C.3}$$

This can be used in the following manner to make the calibration of C.2 more convenient:

$$\left(\frac{\mathrm{d}\Sigma}{\mathrm{d}\Omega}\right)_{s}(q) = \frac{[I_s(q) - I_{B,s}]}{d_s T_s}C \tag{C.4}$$

Once the scattering plot has been scaled to $[cm^{-1}]$, the procedure of extracting the volume can be achieved in the following manner. The volume of a single scatterer (or the average volume of a polydisperse scatterer) can be determined from the scattering curve itself, for example in the case where we apply the ellipsoid-based model, we have information on the average radius and length of our cylinders, and therefore of the volume of the scatterer.

Then, the intensity needs to be extrapolated to $q = 0$. The method that is used for this extrapolation has a significant impact on the accuracy of the obtained result. Stribeck et al. [2002] uses the Guinier approximation for extrapolation to zero angle, for polydisperse as well as monodisperse samples. A closer look should show whether this is the right approximation to use. A better approach might lie in the application of the model described in this thesis to extrapolate to zero angle. Additionally, a check of the determination can be achieved using the simulated scattering patterns of which the volume fraction is known.

When this $I(0)$ value is obtained in the scale of $[cm^{-1}]$, the following equation applies:

$$I(0) = nV_{scat}^2(\Delta\rho)^2 \tag{C.5}$$

Where n is the number of scatterers, $Vscat$ is the volume of a single scatterer, and $\Delta\rho$ is the electron density contrast of the two main phases (and equal to the electron density of the polymer phase in a polymer-void system). The total volume of the scatterers inside the irradiated area can then be obtained by plugging the thus found n into $V_{scat,tot} = nV_{scat}$.

Appendix D

Nanostructures in various fibres

Table D.1: *The nanostructure in various fibres*

sample: Rusar (F2)		fitfunction: Model_2g.m		q range: 0.025 - 0.23		ψ range: 180 - 360		merit 11.1287			
I0	Okappa	R1mean	R1variance	R2mean	R2variance	phishift	bgnd	NPoints_q			
4.98E+04	623	95.1	1.04E+03	489	3.59E+05	89.2	13.8	15			
sample: Armos (F3)		fitfunction: Model_2g.m		q range: 0.025 - 0.23		ψ range: 180 - 360		merit 13.9604			
I0	Okappa	R1mean	R1variance	R2mean	R2variance	phishift	bgnd	NPoints_q			
6.04E+04	615	108	2.37E+03	814	2.62E+05	89.2	14.3	15			
sample: SVM (F4)		fitfunction: Model_2g.m		q range: 0.025 - 0.23		ψ range: 180 - 360		merit 8.2384			
I0	Okappa	R1mean	R1variance	R2mean	R2variance	phishift	bgnd	NPoints_q			
4.21E+04	309	18.8	974	409	7.47E+05	90.9	13.9	15			
sample: Techn. T200 (F5)		fitfunction: Model_2g.m		q range: 0.025 - 0.23		ψ range: 180 - 360		merit 7.3813			
I0	Okappa	R1mean	R1variance	R2mean	R2variance	phishift	bgnd	NPoints_q			
4.02E+04	9.74	604	6.72E+03	9.25	4.93E+04	1.22	14.6	15			
sample: Kevlar 49 (F6A)		fitfunction: Model_2g_special.m		q range: 0.025 - 0.23		ψ range: 180 - 360		merit 47.6761			
I0	I0b	R1mean	R1var	R1bmean	R1basp	R2mean	R2var	bgnd			
4.92E+05	1.87E+04	15.8	35.9	21.8	1.14E+04	81.7	7.27E+03	31.5			
sample: Kevlar 956 (F7A)		fitfunction: Model_2g_special.m		q range: 0.025 - 0.23		ψ range: 180 - 360		merit 22.439			
I0	I0b	R1mean	R1var	R1bmean	R1basp	R2mean	R2var	bgnd			
3.4E+05	2.44E+04	11.9	34	266	34.3	53.3	1.43E+03	25.5			
sample: AS Twaron (F8A)		fitfunction: Model_2g.m		q range: 0.025 - 0.23		ψ range: 180 - 360		merit 101.1937			
I0	Okappa	R1mean	R1variance	R2mean	R2variance	phishift	bgnd	NPoints_q			
4.99E+05	8.13	158	17.6	1.08E+04	4.68E+05	90	63.6	15			
sample: Twaron 1000 (F9A)		fitfunction: Model_2g.m		q range: 0.025 - 0.23		ψ range: 180 - 360		merit 653.9331			
I0	Okappa	R1mean	R1variance	R2mean	R2variance	phishift	bgnd	NPoints_q			
1.44E+06	52.9	16.6	2.34E+04	1.39E+04	8.39E+04	89.8	215	15			
sample: Twaron 2000 (F10)		fitfunction: Model_2g.m		q range: 0.025 - 0.23		ψ range: 180 - 360		merit 11.3913			
I0	Okappa	R1mean	R1variance	R2mean	R2variance	phishift	bgnd	NPoints_q			
2.28E+05	71.7	6.88	39.4	89	2.49E+04	92.4	14.3	15			
sample: Twaron 2100 (F11)		fitfunction: Model_2g.m		q range: 0.025 - 0.23		ψ range: 180 - 360		merit 12.3135			
I0	Okappa	R1mean	R1variance	R2mean	R2variance	phishift	bgnd	NPoints_q			
2.89E+05	49	6.4	42.1	79.7	1.2E+04	87.8	15	15			
sample: Twaron 2200 (F12)		fitfunction: Model_2g.m		q range: 0.025 - 0.23		ψ range: 180 - 360		merit 16.1806			
I0	Okappa	R1mean	R1variance	R2mean	R2variance	phishift	bgnd	NPoints_q			
3.15E+05	69.1	14.8	49.9	96.3	6.12E+04	90.1	15.5	15			
sample: Twaron 2300 (F13)		fitfunction: Model_2g.m		q range: 0.025 - 0.23		ψ range: 180 - 360		merit 9.9743			
I0	Okappa	R1mean	R1variance	R2mean	R2variance	phishift	bgnd	NPoints_q			
2.75E+05	69.1	15.8	22.5	94.4	1.76E+04	89.5	15.3	15			
sample: Zylon AS (F14)		fitfunction: Model_2g.m		q range: 0.025 - 0.23		ψ range: 180 - 360		merit 42.1527			
I0	Okappa	R1mean	R1variance	R2mean	R2variance	phishift	bgnd	NPoints_q			
9.41E+05	111	21.1	38.5	199	3.26E+04	88.9	25.5	15			
sample: Vectran (F15A)		fitfunction: Model_2g.m		q range: 0.025 - 0.23		ψ range: 180 - 360		merit 8.4722			
I0	Okappa	R1mean	R1variance	R2mean	R2variance	phishift	bgnd	NPoints_q			
2.66E+04	11.6	66.4	3.36E+03	2.09E+03	6.97E+03	90	19.2	15			

Appendix E

BW4 results (table)

Table E.1: *BW4 results for Twaron 1000*

sample: t1000_001_00001.tif		fitfunction: Model_2g.m		q range: 0.025 - 0.23		ψ range: 180 - 360		merit 5.6959
I0	Okappa	R1mean	R1variance	R2mean	R2variance	phishift	bgnd	NPoints_q
1.26E+05	91.7	16.3	37.9	100	2.3E+04	1.11	4.21	15
sample: t1000_002_00001.tif		fitfunction: Model_2g.m		q range: 0.025 - 0.23		ψ range: 180 - 360		merit 5.1185
I0	Okappa	R1mean	R1variance	R2mean	R2variance	phishift	bgnd	NPoints_q
1.03E+05	152	16	37.8	111	2.52E+04	1.01	4.06	15
sample: t1000_003_00001.tif		fitfunction: Model_2g.m		q range: 0.025 - 0.23		ψ range: 180 - 360		merit 5.2963
I0	Okappa	R1mean	R1variance	R2mean	R2variance	phishift	bgnd	NPoints_q
1.02E+05	137	15.9	38.3	111	2.64E+04	1	3.87	15
sample: t1000_004_00001.tif		fitfunction: Model_2g.m		q range: 0.025 - 0.23		ψ range: 180 - 360		merit 5.3659
I0	Okappa	R1mean	R1variance	R2mean	R2variance	phishift	bgnd	NPoints_q
1.01E+05	137	15.7	39	112	2.67E+04	0.998	3.98	15
sample: t1000_005_00001.tif		fitfunction: Model_2g.m		q range: 0.025 - 0.23		ψ range: 180 - 360		merit 5.3532
I0	Okappa	R1mean	R1variance	R2mean	R2variance	phishift	bgnd	NPoints_q
1E+05	137	15.9	38.8	112	2.67E+04	0.995	4.15	15
sample: t1000_006_00001.tif		fitfunction: Model_2g.m		q range: 0.025 - 0.23		ψ range: 180 - 360		merit 5.3799
I0	Okappa	R1mean	R1variance	R2mean	R2variance	phishift	bgnd	NPoints_q
9.99E+04	152	15.8	39.6	112	2.59E+04	0.994	4.18	15
sample: t1000_007_00001.tif		fitfunction: Model_2g.m		q range: 0.025 - 0.23		ψ range: 180 - 360		merit 5.5061
I0	Okappa	R1mean	R1variance	R2mean	R2variance	phishift	bgnd	NPoints_q
9.56E+04	137	15.4	40.8	112	2.85E+04	0.966	4.24	15
sample: t1000_008_00001.tif		fitfunction: Model_2g.m		q range: 0.025 - 0.23		ψ range: 180 - 360		merit 5.1693
I0	Okappa	R1mean	R1variance	R2mean	R2variance	phishift	bgnd	NPoints_q
8.92E+04	152	15.1	41.8	110	2.93E+04	0.948	4.24	15
sample: t1000_009_00001.tif		fitfunction: Model_2g.m		q range: 0.025 - 0.23		ψ range: 180 - 360		merit 3.3576
I0	Okappa	R1mean	R1variance	R2mean	R2variance	phishift	bgnd	NPoints_q
8.25E+04	92.4	16.7	35	103	2.29E+04	1.12	2.98	15
sample: t1000_010_00001.tif		fitfunction: Model_2g.m		q range: 0.025 - 0.23		ψ range: 180 - 360		merit 4.9677
I0	Okappa	R1mean	R1variance	R2mean	R2variance	phishift	bgnd	NPoints_q
1.05E+05	100	16.2	35.1	105	2.85E+04	0.904	3.23	15
sample: t1000_011_00001.tif		fitfunction: Model_2g.m		q range: 0.025 - 0.23		ψ range: 180 - 360		merit 4.5381
I0	Okappa	R1mean	R1variance	R2mean	R2variance	phishift	bgnd	NPoints_q
9.78E+04	124	16.8	34.4	113	2.24E+04	0.972	3.6	15
sample: t1000_012_00001.tif		fitfunction: Model_2g.m		q range: 0.025 - 0.23		ψ range: 180 - 360		merit 5.2158
I0	Okappa	R1mean	R1variance	R2mean	R2variance	phishift	bgnd	NPoints_q
8.1E+04	169	15.2	38.5	119	3.29E+04	0.971	3.54	15
sample: t1000_013_00001.tif		fitfunction: Model_2g.m		q range: 0.025 - 0.23		ψ range: 180 - 360		merit 5.1434
I0	Okappa	R1mean	R1variance	R2mean	R2variance	phishift	bgnd	NPoints_q
8.62E+04	113	16.2	42.8	111	2.31E+04	0.899	3.7	15
sample: t1000_014_00001.tif		fitfunction: Model_2g.m		q range: 0.025 - 0.23		ψ range: 180 - 360		merit 3.9954
I0	Okappa	R1mean	R1variance	R2mean	R2variance	phishift	bgnd	NPoints_q
1.02E+05	86.4	17.1	34.9	104	2.49E+04	1.46	3.49	15
sample: t1000_015_00001.tif		fitfunction: Model_2g.m		q range: 0.025 - 0.23		ψ range: 180 - 360		merit 2.5026
I0	Okappa	R1mean	R1variance	R2mean	R2variance	phishift	bgnd	NPoints_q
6.51E+04	69.1	17	34.2	98.6	2.06E+04	1.06	2.24	15
sample: t1000_016_00001.tif		fitfunction: Model_2g.m		q range: 0.025 - 0.23		ψ range: 180 - 360		merit 1.6582
I0	Okappa	R1mean	R1variance	R2mean	R2variance	phishift	bgnd	NPoints_q
4E+04	79.9	17.1	35.5	98.1	1.96E+04	0.966	2.22	15

Continued on next page

Table E.1 – continued from previous page

sample: t1000_017_00001.tif		fitfunction: Model_2g.m		q range: 0.025 - 0.23		ψ range: 180 - 360		merit 2.3584
I0	Okappa	R1mean	R1variance	R2mean	R2variance	phishift	bgnd	NPoints_q
5.65E+04	92.2	17.7	28.4	99.9	1.89E+04	0.353	2.62	15
sample: t1000_018_00001.tif		fitfunction: Model_2g.m		q range: 0.025 - 0.23		ψ range: 180 - 360		merit 1.9608
I0	Okappa	R1mean	R1variance	R2mean	R2variance	phishift	bgnd	NPoints_q
4.65E+04	80	17.2	32.1	99.3	1.97E+04	1.37	2.55	15
sample: t1000_019_00001.tif		fitfunction: Model_2g.m		q range: 0.025 - 0.23		ψ range: 180 - 360		merit 2.2028
I0	Okappa	R1mean	R1variance	R2mean	R2variance	phishift	bgnd	NPoints_q
4.35E+04	93.6	17.3	35.6	100	2.4E+04	0.836	2.58	15
sample: t1000_021_00001.tif		fitfunction: Model_2g.m		q range: 0.025 - 0.23		ψ range: 180 - 360		merit 3.445
I0	Okappa	R1mean	R1variance	R2mean	R2variance	phishift	bgnd	NPoints_q
1.07E+05	98.6	16.9	36.2	102	1.95E+04	0.8	4.34	15
sample: t1000_022_00001.tif		fitfunction: Model_2g.m		q range: 0.025 - 0.23		ψ range: 180 - 360		merit 3.2979
I0	Okappa	R1mean	R1variance	R2mean	R2variance	phishift	bgnd	NPoints_q
1.02E+05	100	17	35.1	100	1.9E+04	0.845	4.33	15
sample: t1000_023_00001.tif		fitfunction: Model_2g.m		q range: 0.025 - 0.23		ψ range: 180 - 360		merit 3.1875
I0	Okappa	R1mean	R1variance	R2mean	R2variance	phishift	bgnd	NPoints_q
9.7E+04	100	17.1	34.2	97.6	1.9E+04	0.954	4.37	15
sample: t1000_024_00001.tif		fitfunction: Model_2g.m		q range: 0.025 - 0.23		ψ range: 180 - 360		merit 2.9897
I0	Okappa	R1mean	R1variance	R2mean	R2variance	phishift	bgnd	NPoints_q
9.14E+04	100	17.4	33.7	97	1.93E+04	0.924	2.98	15
sample: t1000_025_00001.tif		fitfunction: Model_2g.m		q range: 0.025 - 0.23		ψ range: 180 - 360		merit 3.2339
I0	Okappa	R1mean	R1variance	R2mean	R2variance	phishift	bgnd	NPoints_q
1.04E+05	99.6	17.2	36	97.8	2.04E+04	0.956	3.23	15
sample: t1000_026_00001.tif		fitfunction: Model_2g.m		q range: 0.025 - 0.23		ψ range: 180 - 360		merit 4.5128
I0	Okappa	R1mean	R1variance	R2mean	R2variance	phishift	bgnd	NPoints_q
1.12E+05	86.4	16.8	37.8	97.4	2.63E+04	0.792	3.59	15
sample: t1000_027_00001.tif		fitfunction: Model_2g.m		q range: 0.025 - 0.23		ψ range: 180 - 360		merit 5.064
I0	Okappa	R1mean	R1variance	R2mean	R2variance	phishift	bgnd	NPoints_q
1.19E+05	100	16.7	35.9	102	3.26E+04	0.855	3.64	15
sample: t1000_028_00001.tif		fitfunction: Model_2g.m		q range: 0.025 - 0.23		ψ range: 180 - 360		merit 4.9735
I0	Okappa	R1mean	R1variance	R2mean	R2variance	phishift	bgnd	NPoints_q
1.02E+05	137	16.7	39.7	105	2.62E+04	0.916	3.84	15
sample: t1000_029_00001.tif		fitfunction: Model_2g.m		q range: 0.025 - 0.23		ψ range: 180 - 360		merit 4.7131
I0	Okappa	R1mean	R1variance	R2mean	R2variance	phishift	bgnd	NPoints_q
8.62E+04	124	15.5	43	97.7	3.27E+04	1	3.57	15
sample: t1000_030_00001.tif		fitfunction: Model_2g.m		q range: 0.025 - 0.23		ψ range: 180 - 360		merit 4.2099
I0	Okappa	R1mean	R1variance	R2mean	R2variance	phishift	bgnd	NPoints_q
1.01E+05	82.6	16.6	40.2	93.5	2.58E+04	1.17	3.77	15
sample: t1000_031_00001.tif		fitfunction: Model_2g.m		q range: 0.025 - 0.23		ψ range: 180 - 360		merit 4.2344
I0	Okappa	R1mean	R1variance	R2mean	R2variance	phishift	bgnd	NPoints_q
1.01E+05	80	16.6	41.1	93.4	2.64E+04	1.14	3.68	15
sample: t1000_032_00001.tif		fitfunction: Model_2g.m		q range: 0.025 - 0.23		ψ range: 180 - 360		merit 4.2562
I0	Okappa	R1mean	R1variance	R2mean	R2variance	phishift	bgnd	NPoints_q
1.01E+05	80	16.6	41.3	93	2.64E+04	1.12	3.82	15
sample: t1000_033_00001.tif		fitfunction: Model_2g.m		q range: 0.025 - 0.23		ψ range: 180 - 360		merit 4.2459
I0	Okappa	R1mean	R1variance	R2mean	R2variance	phishift	bgnd	NPoints_q
1.01E+05	80	16.5	41.9	92.7	2.64E+04	1.12	3.75	15
sample: t1000_034_00001.tif		fitfunction: Model_2g.m		q range: 0.025 - 0.23		ψ range: 180 - 360		merit 4.2698
I0	Okappa	R1mean	R1variance	R2mean	R2variance	phishift	bgnd	NPoints_q
1.01E+05	80	16.5	42.1	92.7	2.63E+04	1.11	3.94	15
sample: t1000_035_00001.tif		fitfunction: Model_2g.m		q range: 0.025 - 0.23		ψ range: 180 - 360		merit 4.3000
I0	Okappa	R1mean	R1variance	R2mean	R2variance	phishift	bgnd	NPoints_q
1.01E+05	80	16.6	41.9	92.5	2.64E+04	1.11	4.03	15
sample: t1000_036_00001.tif		fitfunction: Model_2g.m		q range: 0.025 - 0.23		ψ range: 180 - 360		merit 4.3121
I0	Okappa	R1mean	R1variance	R2mean	R2variance	phishift	bgnd	NPoints_q
1.01E+05	80	16.6	42.3	92.5	2.63E+04	1.1	4.05	15
sample: t1000_037_00001.tif		fitfunction: Model_2g.m		q range: 0.025 - 0.23		ψ range: 180 - 360		merit 4.706
I0	Okappa	R1mean	R1variance	R2mean	R2variance	phishift	bgnd	NPoints_q
1.03E+05	137	16	38.2	117	2.69E+04	0.846	4.89	15
sample: t1000_038_00001.tif		fitfunction: Model_2g.m		q range: 0.025 - 0.23		ψ range: 180 - 360		merit 4.5892
I0	Okappa	R1mean	R1variance	R2mean	R2variance	phishift	bgnd	NPoints_q
9.52E+04	137	15.5	41.5	115	2.9E+04	0.845	4.89	15
sample: t1000_039_00001.tif		fitfunction: Model_2g.m		q range: 0.025 - 0.23		ψ range: 180 - 360		merit 4.5373
I0	Okappa	R1mean	R1variance	R2mean	R2variance	phishift	bgnd	NPoints_q
8.93E+04	124	15.2	42.6	110	3.31E+04	0.832	3.38	15
sample: t1000_040_00001.tif		fitfunction: Model_2g.m		q range: 0.025 - 0.23		ψ range: 180 - 360		merit 4.4391
I0	Okappa	R1mean	R1variance	R2mean	R2variance	phishift	bgnd	NPoints_q
7.81E+04	124	14.8	45.7	104	3.54E+04	0.801	3.34	15
sample: t1000_041_00001.tif		fitfunction: Model_2g.m		q range: 0.025 - 0.23		ψ range: 180 - 360		merit 4.8788
I0	Okappa	R1mean	R1variance	R2mean	R2variance	phishift	bgnd	NPoints_q
7.79E+04	124	14.6	47.2	107	4.1E+04	0.849	3.54	15
sample: t1000_042_00001.tif		fitfunction: Model_2g.m		q range: 0.025 - 0.23		ψ range: 180 - 360		merit 5.1391
I0	Okappa	R1mean	R1variance	R2mean	R2variance	phishift	bgnd	NPoints_q
7.99E+04	113	15.1	48.4	108	3.4E+04	0.858	3.76	15
sample: t1000_043_00001.tif		fitfunction: Model_2g.m		q range: 0.025 - 0.23		ψ range: 180 - 360		merit 5.9988
I0	Okappa	R1mean	R1variance	R2mean	R2variance	phishift	bgnd	NPoints_q
1.12E+05	124	16.9	35.3	118	2.54E+04	0.892	3.96	15
sample: t1000_044_00001.tif		fitfunction: Model_2g.m		q range: 0.025 - 0.23		ψ range: 180 - 360		merit 5.8673
I0	Okappa	R1mean	R1variance	R2mean	R2variance	phishift	bgnd	NPoints_q

Continued on next page

Table E.1 – continued from previous page

1.07E+05	137	16.7	37.5	116	2.64E+04	0.897	4.13	15
sample: t1000_045_00001.tif		fitfunction: Model_2g.m		q range: 0.025 - 0.23		ψ range: 180 - 360		merit 5.8254
I0	Okappa	R1mean	R1variance	R2mean	R2variance	phishift	bgnd	NPoints_q
1E+05	137	16.6	39	115	2.93E+04	0.891	4.25	15
sample: t1000_046_00001.tif		fitfunction: Model_2g.m		q range: 0.025 - 0.23		ψ range: 180 - 360		merit 5.3287
I0	Okappa	R1mean	R1variance	R2mean	R2variance	phishift	bgnd	NPoints_q
9.05E+04	124	16.3	41.6	112	3.28E+04	0.879	4.14	15
sample: t1000_047_00001.tif		fitfunction: Model_2g.m		q range: 0.025 - 0.23		ψ range: 180 - 360		merit 5.9761
I0	Okappa	R1mean	R1variance	R2mean	R2variance	phishift	bgnd	NPoints_q
9.02E+04	137	16.1	43	113	3.34E+04	0.873	4.35	15
sample: t1000_048_00001.tif		fitfunction: Model_2g.m		q range: 0.025 - 0.23		ψ range: 180 - 360		merit 6.3766
I0	Okappa	R1mean	R1variance	R2mean	R2variance	phishift	bgnd	NPoints_q
1.22E+05	100	16.6	32.5	105	2.91E+04	0.911	4.31	15
sample: t1000_049_00001.tif		fitfunction: Model_2g.m		q range: 0.025 - 0.23		ψ range: 180 - 360		merit 6.6465
I0	Okappa	R1mean	R1variance	R2mean	R2variance	phishift	bgnd	NPoints_q
1.18E+05	113	17.1	35	110	2.14E+04	0.909	4.94	15
sample: t1000_050_00001.tif		fitfunction: Model_2g.m		q range: 0.025 - 0.23		ψ range: 180 - 360		merit 6.3585
I0	Okappa	R1mean	R1variance	R2mean	R2variance	phishift	bgnd	NPoints_q
1.14E+05	113	17.4	34.5	112	2.3E+04	0.915	5.14	15
sample: t1000_051_00001.tif		fitfunction: Model_2g.m		q range: 0.025 - 0.23		ψ range: 180 - 360		merit 5.8066
I0	Okappa	R1mean	R1variance	R2mean	R2variance	phishift	bgnd	NPoints_q
1.03E+05	113	17.1	38.4	109	2.43E+04	0.894	4.87	15
sample: t1000_052_00001.tif		fitfunction: Model_2g.m		q range: 0.025 - 0.23		ψ range: 180 - 360		merit 6.669
I0	Okappa	R1mean	R1variance	R2mean	R2variance	phishift	bgnd	NPoints_q
1.06E+05	104	16.6	40.4	109	2.64E+04	0.902	4.98	15
sample: t1000_053_00001.tif		fitfunction: Model_2g.m		q range: 0.025 - 0.23		ψ range: 180 - 360		merit 6.6674
I0	Okappa	R1mean	R1variance	R2mean	R2variance	phishift	bgnd	NPoints_q
9.68E+04	169	15.3	38.9	121	3.54E+04	0.932	3.62	15
sample: t1000_054_00001.tif		fitfunction: Model_2g.m		q range: 0.025 - 0.23		ψ range: 180 - 360		merit 5.2819
I0	Okappa	R1mean	R1variance	R2mean	R2variance	phishift	bgnd	NPoints_q
1.29E+05	92.6	16.8	33.8	101	2.47E+04	0.759	3.88	15
sample: t1000_055_00001.tif		fitfunction: Model_2g.m		q range: 0.025 - 0.23		ψ range: 180 - 360		merit 5.344
I0	Okappa	R1mean	R1variance	R2mean	R2variance	phishift	bgnd	NPoints_q
1.28E+05	90.1	16.9	35	100	2.65E+04	0.754	4.13	15
sample: t1000_056_00001.tif		fitfunction: Model_2g.m		q range: 0.025 - 0.23		ψ range: 180 - 360		merit 5.1538
I0	Okappa	R1mean	R1variance	R2mean	R2variance	phishift	bgnd	NPoints_q
1.24E+05	86.4	17	37.8	99.6	2.83E+04	0.752	4.2	15
sample: t1000_057_00001.tif		fitfunction: Model_2g.m		q range: 0.025 - 0.23		ψ range: 180 - 360		merit 5.5265
I0	Okappa	R1mean	R1variance	R2mean	R2variance	phishift	bgnd	NPoints_q
1.26E+05	84.8	16.8	38.3	99.4	2.95E+04	0.735	4.38	15

Table E.2: *BW4 results for AS Twaron*

sample: tas_020_00001.tif		fitfunction: Model_2g_special.m		q range: 0.025 - 0.23		ψ range: 180 - 360		merit 1.6247
I0	I0b	R1mean	R1var	R1bmean	R1basp	R2mean	R2var	bgnd
1.85E+04	2.09E+03	15.5	41.2	403	20.2	67.4	2.12E+03	2.72
sample: tas_058_00001.tif		fitfunction: Model_2g_special.m		q range: 0.025 - 0.23		ψ range: 180 - 360		merit 2.5894
I0	I0b	R1mean	R1var	R1bmean	R1basp	R2mean	R2var	bgnd
9.08E+03	2.92E+03	10.8	30.9	403	25.2	51.5	2.05E+03	2.71
sample: tas_059_00001.tif		fitfunction: Model_2g_special.m		q range: 0.025 - 0.23		ψ range: 180 - 360		merit 2.6848
I0	I0b	R1mean	R1var	R1bmean	R1basp	R2mean	R2var	bgnd
1.21E+04	2.83E+03	12	38.7	401	25.7	59.4	2.39E+03	2.78
sample: tas_060_00001.tif		fitfunction: Model_2g_special.m		q range: 0.025 - 0.23		ψ range: 180 - 360		merit 2.7009
I0	I0b	R1mean	R1var	R1bmean	R1basp	R2mean	R2var	bgnd
1.49E+04	2.85E+03	12.6	41.6	401	25.7	64.5	2.38E+03	2.93
sample: tas_061_00001.tif		fitfunction: Model_2g_special.m		q range: 0.025 - 0.23		ψ range: 180 - 360		merit 2.7174
I0	I0b	R1mean	R1var	R1bmean	R1basp	R2mean	R2var	bgnd
1.74E+04	2.9E+03	13	42.3	402	25.2	65.5	2.28E+03	2.99
sample: tas_062_00001.tif		fitfunction: Model_2g_special.m		q range: 0.025 - 0.23		ψ range: 180 - 360		merit 2.7438
I0	I0b	R1mean	R1var	R1bmean	R1basp	R2mean	R2var	bgnd
1.94E+04	2.94E+03	13.3	41.1	402	25.3	65.8	2.18E+03	3.07
sample: tas_063_00001.tif		fitfunction: Model_2g_special.m		q range: 0.025 - 0.23		ψ range: 180 - 360		merit 2.7438
I0	I0b	R1mean	R1var	R1bmean	R1basp	R2mean	R2var	bgnd
2.1E+04	2.93E+03	13.6	40	402	25.2	65.5	2.11E+03	3.13
sample: tas_064_00001.tif		fitfunction: Model_2g_special.m		q range: 0.025 - 0.23		ψ range: 180 - 360		merit 1.7309
I0	I0b	R1mean	R1var	R1bmean	R1basp	R2mean	R2var	bgnd
1.32E+04	2.53E+03	14.5	26.2	381	12.3	54.8	2E+03	2.99
sample: tas_065_00001.tif		fitfunction: Model_2g_special.m		q range: 0.025 - 0.23		ψ range: 180 - 360		merit 3.9659
I0	I0b	R1mean	R1var	R1bmean	R1basp	R2mean	R2var	bgnd
3.06E+04	6.33E+03	7.4	36.4	377	23.3	53.5	2.23E+03	4.12
sample: tas_066_00001.tif		fitfunction: Model_2g_special.m		q range: 0.025 - 0.23		ψ range: 180 - 360		merit 4.2529
I0	I0b	R1mean	R1var	R1bmean	R1basp	R2mean	R2var	bgnd
2.76E+04	6.43E+03	7.52	35.5	377	23.4	53.1	2.6E+03	4.14
sample: tas_067_00001.tif		fitfunction: Model_2g_special.m		q range: 0.025 - 0.23		ψ range: 180 - 360		merit 4.0037
I0	I0b	R1mean	R1var	R1bmean	R1basp	R2mean	R2var	bgnd
2.53E+04	6.05E+03	10.9	32.2	377	23.3	51.6	2.68E+03	4.08

Continued on next page

Table E.2 – continued from previous page

sample: tas_068_00001.tif		fitfunction: Model_2g_special.m		q range: 0.025 - 0.23		ψ range: 180 - 360		merit 2.4769
I0	I0b	R1mean	R1var	R1bmean	R1basp	R2mean	R2var	bgnd
2.08E+04	3.63E+03	13.1	32.7	373	27	53.4	1.95E+03	4.02
sample: tas_070_00001.tif		fitfunction: Model_2g_special.m		q range: 0.025 - 0.23		ψ range: 180 - 360		merit 3.1897
I0	I0b	R1mean	R1var	R1bmean	R1basp	R2mean	R2var	bgnd
1.87E+04	5.13E+03	11	35.2	376	23.5	51.6	1.7E+03	4.14
sample: tas_071_00001.tif		fitfunction: Model_2g_special.m		q range: 0.025 - 0.23		ψ range: 180 - 360		merit 3.4086
I0	I0b	R1mean	R1var	R1bmean	R1basp	R2mean	R2var	bgnd
1.91E+04	5.72E+03	11	34.4	376	23.5	49.7	1.61E+03	2.72
sample: tas_072_00001.tif		fitfunction: Model_2g_special.m		q range: 0.025 - 0.23		ψ range: 180 - 360		merit 0.94796
I0	I0b	R1mean	R1var	R1bmean	R1basp	R2mean	R2var	bgnd
717	135	2.92	94.9	647	7.55	28.1	826	1.82
sample: tas_073_00001.tif		fitfunction: Model_2g_special.m		q range: 0.025 - 0.23		ψ range: 180 - 360		merit 2.0207
I0	I0b	R1mean	R1var	R1bmean	R1basp	R2mean	R2var	bgnd
2.29E+04	3.17E+03	12.4	38	377	22.8	51.2	1.43E+03	2.81
sample: tas_074_00001.tif		fitfunction: Model_2g_special.m		q range: 0.025 - 0.23		ψ range: 180 - 360		merit 2.469
I0	I0b	R1mean	R1var	R1bmean	R1basp	R2mean	R2var	bgnd
2.19E+04	3.73E+03	12.6	38	375	23.3	46.3	1.35E+03	2.92
sample: tas_075_00001.tif		fitfunction: Model_2g_special.m		q range: 0.025 - 0.23		ψ range: 180 - 360		merit 26.2317
I0	I0b	R1mean	R1var	R1bmean	R1basp	R2mean	R2var	bgnd
1.75E+04	3.05E+03	15.1	26.8	377	23.1	49.3	941	2.61
sample: tas_069_00001.tif		fitfunction: Model_2g_special.m		q range: 0.025 - 0.23		ψ range: 180 - 360		merit 3.0775
I0	I0b	R1mean	R1var	R1bmean	R1basp	R2mean	R2var	bgnd
2.12E+04	4.96E+03	11.3	34.3	377	23.4	51.9	1.94E+03	4.01

Department of Chemical
and Biochemical Engineering

DTU Building 229
Søltofts Plads
DK-2800 Kgs. Lyngby
www.kt.dtu.dk